Studies on Traction Separation Relations in Fracture of Layered Composites; Experiments and Modeling

THÈSE N^{O} 7768 (2017)

PRÉSENTÉE LE 29 MAI 2017
À LA FACULTÉ DES SCIENCES ET TECHNIQUES DE L'INGÉNIEUR
LABORATOIRE DE MÉCANIQUE APPLIQUÉE ET D'ANALYSE DE FIABILITÉ
PROGRAMME DOCTORAL EN MÉCANIQUE

ÉCOLE POLYTECHNIQUE FÉDÉRALE DE LAUSANNE

POUR L'OBTENTION DU GRADE DE DOCTEUR ÈS SCIENCES

PAR

Georgios PAPPAS

acceptée sur proposition du jury:

Prof. F. Gallaire, président du jury
Prof. J. Botsis, directeur de thèse
Prof. G. Lubineau, rapporteur
Prof. C. González, rapporteur
Prof. V. Michaud, rapporteuse

ÉCOLE POLYTECHNIQUE
FÉDÉRALE DE LAUSANNE

Suisse
2017

Abstract

Layered fiber reinforced composite materials are prone to fracture in planes parallel to the direction of fibers leading to extensive delamination or intralaminar fracture. This phenomenon of crack propagation is frequently accompanied by significant increase in fracture resistance due to different damage mechanisms active on the wake of the crack. The developed zone comprises intact pulled-out fibers bridging the crack faces forming the so-called, large scale fiber bridging (LSB). Several studies have dealt with the evaluation of the traction-separation relations mainly related to the bridging phenomena in delamination, employing different techniques. However, only a few recent studies dealt with the effect of specimen size on LSB and the traction-separation relations, challenging the applicability of the existing relations in structural design.

This work initially focuses on the characterization of LSB phenomena in mode I intralaminar fracture of a unidirectional (UD) carbon fiber reinforced thermoplastic. Here an already developed semi-experimental technique based on quasi-continuous strain measurements by FBG sensors, adapted to the needs of the current study, is employed to identify the traction-separation relation. The outcome of the identification scheme compares very well with the results from a numerical micromechanical virtual test. The identified traction-separation relation is employed to calculate the energy release rate (ERR) and evaluate the resistance curves (R-curves) associated with LSB of this fracture response. An important toughening effect is demonstrated, which is about two times higher than the corresponding interlaminar values.

The aforementioned semi-experimental technique is implemented in intralaminar fracture of a UD carbon/epoxy composite and is devoted in evaluating the effect of specimen thickness on the developed closing tractions due to LSB. Here, double cantilever beam (DCB) specimens of three different thicknesses, loaded with end opening forces are employed to conduct the characterization. A significant effect of specimen's thickness is present on the three identified traction-separation relations.

The results of the present study indicate a scaling relationship expressed as a function of the bridging traction profile exponent and the stiffness of the specimen. Nevertheless, a common maximum closing traction at the crack tip is evaluated. Similar to the thermoplastic composite, the measured ERRs are considerably higher than the corresponding interlaminar values.

Furthermore, a testing apparatus able to apply pure moments on the bending arms of DCB specimens, by means of pairs of forces is designed, fabricated and used. This testing setup is employed in the fracture characterization of the mentioned carbon/epoxy system to investigate the effect of loading conditions. The acquired results show minor differences on the maximum ERRs, with some small variation on the shape of the R-curves.

Finally, the traction-separation relation in delamination of a woven glass fiber reinforced epoxy with tufting through the thickness reinforcement (TTR) is investigated. Accordingly, a generalization of the relation between the closing traction profile and flexural rigidity of the DCB arms is attested and a concise modeling approach for the load history prediction is proposed comprising the effects of LSB and TTR.

Keywords: Fiber reinforced polymers; Intralaminar fracture; Delamination; Fiber Bragg gratings; Fiber bridging; Traction-separation relation; Cohesive zone modeling; R-curves scaling; Micromechanics; Through the thickness reinforcement.

Résumé

Les matériaux composites laminés renforcés par des fibres sont enclins à rompre dans des plans parallèles à la direction des fibres, ce qui induit une délamination ou une rupture intralaminaire étendue. Ce phénomène de propagation de fissure est fréquemment accompagné d'une augmentation significative de la résistance à la rupture, à cause de divers mécanismes de dommage actifs dans le sillage de la fissure. Cette zone comprend des fibres arrachées intactes reliant les faces de la fissure, formant du pontage de fibres à grande échelle (LSB, large scale bridging). Plusieurs études ont évalué les relations de traction-séparation associées au phénomène de pontage principalement en délamination, utilisant diverses techniques. Cependant, seules quelques études récentes ont examiné l'effet de la taille de l'éprouvette sur le pontage et les relations de traction-séparation, questionnant l'applicabilité de telles relations dans la conception de structures.

Ce travail se concentre en premier lieu à la caractérisation du phénomène LSB en rupture intralaminaire en mode I, dans un laminé unidirectionnel (UD) fait d'un thermoplastique renforcé par des fibres de carbone. Une technique semi-expérimentale existante basée sur des mesures de déformation quasi-continues obtenues grâce à des capteurs à fibres optique à réseaux de Bragg, est adaptée aux besoins de cette étude, et appliquée afin d'identifier la relation de traction-séparation. Les résultats de cette procédure d'identification correspondent très bien avec les résultats obtenus par un test virtuel micromécanique. La relation de traction-séparation identifiée est utilisée pour calculer le taux de restitution d'énergie (ERR, energy release rate) et évaluer les courbes de résistance (R-curves) correspondant au LSB de cette rupture. Un effet notable d'augmentation de la ténacité est montré. Cet effet est environ deux fois plus grand qu'en rupture interlaminaire.

La technique semi-expérimentale mentionnée ci-avant est appliquée à la rupture intralaminaire d'un composite carbone/époxy UD et est dédiée à l'évaluation de l'effet de l'épaisseur de l'éprouvette sur le développement des contraintes de fermetures dues au LSB. Ici, des éprouvettes DCB (double porte-à-faux) ayant trois épaisseurs différentes, chargées en leur extrémité par des forces d'ouverture sont utilisées pour mener la caractérisation. Un effet significatif de l'épaisseur de l'éprouvette est trouvé sur les trois relations de traction-séparation obtenues. Les résultats de cette étude montrent un effet d'échelle exprimée en fonction de l'exposant du profil de contraintes et de la rigidité en flexion de l'éprouvette. Néanmoins, la contrainte de fermeture maximale, en pointe de fissure, est trouvée constante. Comme observé pour le composite thermoplastique, les ERRs sont considérablement plus hauts que les valeurs obtenues en rupture interlaminaire.

Par ailleurs, un dispositif de test capable d'appliquer un moment pur aux bras des éprouvettes DCB, au moyen de paires de forces, est conçu, fabriqué et utilisé. Ce dispositif est utilisé dans la caractérisation du composite carbone/époxy pour investiguer l'effet des conditions de chargement. Les résultats montrent de faibles différences sur les ERRs maximaux, avec quelques disparités sur la forme des courbes de résistance.

Enfin, la relation de traction-séparation en délamination d'un composite époxy/fibres de verre, tissées avec renforcement transversal par touffetage (tufting) est investiguée. Par suite, une généralisation de la relation entre le profil des contraintes de fermeture et la rigidité en flexion des bras de l'éprouvette DCB est validée et une approche de modélisation concise pour la prédiction de l'historique des forces est proposée, incluant les effets du LSB et de renforcement transversal.

Mots-clés: Polymères renforcés de fibres; Rupture intralaminaire; Délamination; Fibre optique à réseaux de Bragg; Pontage de fibres; Relation de traction-séparation; Model à zone cohésive; Effet d'échelle sur les courbes de résistances; Micromécanique; Renforcement transversal.

Acknowledgements

I would like to express my deep gratitude to Prof. John Botsis, primarily for giving me the opportunity to work at the Laboratory of Applied Mechanics and Reliability Analysis (LMAF). I feel grateful for all his great support and mentorship throughout the past four years and for his continuous availability and involvement in the research projects we conducted together. John has always kept his door open for my inquiries, as he does for every-one of his students.

I would also like to thank my officemate for the last two years and research partner Dr. Luis Canal, for his guidance in our projects, for transferring to me important knowledge and for our fruitful discussions that resulted into high quality research work. My sincerest thanks are also extended to Prof. S. Joncas (ÉTS, Montréal), for bringing the opportunity of a high quality research project, for transferring to me his experience in the field and for the overall excellent collaboration we had.

I would like to express my great appreciation to Dr. Joël Cugnoni for his valuable help in the modal-analysis material characterization, and for his constructive suggestions and availability during the last four years. I ought to thank also my first officemate in LMAF Dr. Roohollah Sarfaraz Khabbaz for his assistance in my first months at EPFL, and for sharing with me his expertise in the field. Many thanks should also be given to Dr. Marco Lai for volunteering to assist me in my first months in the lab.

I cannot forget expressing my thanks to Dr. Borotto, my friend Marco, for sharing with me his knowledge in the field, for being my companion in the long afternoons in the lab as well as in our sports activities and trips to Milan. I wish to thank Dr. Ebrahim Farmand Ashtiani, for introducing me to the experimental techniques of LMAF.

I further need to acknowledge the productive interaction we had with Guillaume Frossard and the warm working environment that all of my LMAF colleagues: Robin Amacher, Sébastien Kohler, Nassima Nasri and Prof. Thomas Gmür created during these years. Many thanks should be given to Mrs. Viviane Magnenat for her help in finding accommodation upon my arrival in Lausanne, and for all of her willingness and efficiency in our collaboration these years. I would also like to thank Prof. Véronique Michaud for the excellent collaboration in our common project.

Special thanks should be given to all the members of the ATME workshop for their contribution on machining all the necessary parts for the designed testing setups and specimens used in this project and in particular to Mr. Marc Jeanneret for his willingness to share his experience and offer his time so generously in perfecting my designs and improving the precision on the fabricated parts.

I would also like to extend my thanks to my father and my close family for their support, encouragement and trust in my choices.

Last, but not least, I feel the need to thank Naya, my partner in life, for all her love, for supporting and encouraging me from the very first moment of my application in the doctoral school and for continuing to standing by me through the good and the difficult times.

Contents

Abstract i

Résumé iii

Acknowledgements v

Contents vii

List of Figures xi

List of Tables xvii

List of Symbols xix

List of abbreviations xxiii

1. Introduction **1**

1.1 General foreword & motivation 1

1.2 Objective 5

1.3 Thesis outline 6

2. State of the art **9**

2.1 General definitions in fracture 9

2.2 Traction-separation relations and R-curves 11

2.3 Failure of fiber reinforced composites and LSB 13

2.3.1 Fiber bridging and characterization techniques 14

2.3.2 Comments on damage tolerance and other potentials 16

2.4 Micromechanics and Virtual testing techniques 18

2.5 Through the thickness reinforcement techniques 19

2.6 Fracture testing configurations 21

3. Methods **25**

3.1 Fracture testing and specimens 25

3.2 ERR calculation 27
  3.2.1 Linear elastic fracture mechanics 28
  3.2.2 General fracture mechanics' cases 31
  3.2.3 DCB under pure moment 32
3.3 Microscopy and fractography 34
3.4 Strain acquisition technique 35
3.5 FBG position tracking 38
3.6 Numerical Methods 39
  3.6.1 Identification of bridging tractions 41
  3.6.2 Cohesive zone modeling 46
  3.6.3 Embedded cell approach 48
  3.6.4 Fracture characterization methodology summary 49
4. Intralaminar fracture of UD carbon fiber/thermoplastic polymer-composite 51
4.1 Materials and specimens 51
4.2 Fracture testing 53
4.3 Results and discussion 53
  4.3.1 Fracture morphology 53
  4.3.2 Strain measurements 54
  4.3.3 Traction-separation relation and cohesive model 56
  4.3.4 Load-displacement and rotation curves 57
  4.3.5 Resistance curves 58
4.4 Summary of key points 61
5. Intralaminar fracture of UD carbon/epoxy composite; i) Convectional DCB 63
5.1 Materials and specimens 63
5.2 Fracture testing 65
5.3 Results 65
  5.3.1 Fracture morphology 65
  5.3.2 Load-displacement response 66
  5.3.3 Strain data 67

5.3.4 Identification of bridging tractions 68
5.3.5 Cohesive zone modelling 71
5.3.6 Resistance curves 72
5.4 Summary of key points 74
5.5 Discussion on LSB contribution and ERR evolution 75
6. Intralaminar fracture of UD carbon/epoxy composite; ii) Pure Moment Configuration 77
6.1 Design of the test-rig 77
6.1.1 Loading concept 77
6.1.2 Effects on loading points 78
6.1.3 Machine design and kinematics 80
6.2 Materials and specimens 81
6.3 Fracture testing 82
6.4 Evaluation of ERRs 84
6.5 Preliminary analysis and estimated results 87
6.6 Results of batch #2 88
6.7 Results of batch #3 and discussion 93
7. Traction-separation relations in delamination of a tufted GFRP composite 97
7.1 Materials and specimens 97
7.1.1 Material fabrication and elastic properties 97
7.1.2 DCB specimens 99
7.2 Fracture testing 101
7.3 Fracture morphology 101
7.4 Results of neat GFRP 103
7.4.1 Experimental R-curves 103
7.4.2 Strain data 104
7.4.3 Identification of traction-separation relations 105
7.4.4 Load-displacement response and cohesive zone modelling 108
7.5 Numerical approach and experimental results of the tufted GFRP 109

7.5.1 Experimental R-curves 109
7.5.2 Uniaxial tuft pulling tests 110
7.5.3 Load-history prediction modeling 111
7.6 Key points summary and discussion 114
8. Concluding remarks 117
8.1 General discussion & conclusions 117
8.2 Research perspectives and future work 120
Appendix I Numerical calculation of J-integral 123
Appendix II Material and specimen fabrication 127
Appendix III Fractography and micrographic observations 129
Appendix IV Design details of the Pure-Moment configuration 133
REFERENCES 137
Curriculum Vitæ 149

List of Figures

Fig. 1.1: Global carbon fiber consumption (tons) by application (2012) [1]. 1

Fig. 1.2: (a) Failure mechanisms' micrographs, in a cross-ply laminate (compact tension specimen at the compression side); modified from [5]. (b) Schema of possible energy absorption mechanisms during crack growth of a UD laminate [3]. 3

Fig. 1.3: Definition of intralaminar, interlaminar and translaminar crack. 4

Fig. 2.1: Definition of fracture modes... 9

Fig. 2.2: Superposition principle in LEFM 10

Fig. 2.3: Test specimen and real structure stress conditions. The detail shows the singularity dominated zone; courtesy of [20]. 11

Fig. 2.4: Stress distributions and cohesive models for FPZ; modified from [24]........... 12

Fig. 2.5: Crack stability: (a) Brittle fracture. (b) Typical rising R-curve behavior. 13

Fig. 2.6: Closing tractions profile, with bridging and FPZ. 14

Fig. 2.7: (a) DCB under end opening forces. (b) DCB under pure-moment. 21

Fig. 2.8: Pure moment loading configurations present in the literature: (a) Freiman et al., 1973 [82]. (b) Latest adaptation of Sørensen et al., 1996 [78] at Sørensen & Jacobsen, 2009 [27]. (c) Lindhagen & Berglund, 2000 [83]. (d) Berggreen & Anyfantis, 2014 & Saseendran et al., 2015 [79] & [80]. 23

Fig. 2.9: Examples of specimen configurations J-integral measurements 'independent of the details of the traction-separation relation' [27]: (a) DCB specimen under pure moments (Mode I). (b) DCB specimen under both axial forces and moments (Mixed Mode I &II). (c) DCB specimen under uneven moments (DCB-UBM) (Mixed Mode I &II). (d)DCB specimen loaded with pure, equal moments (pure Mode II). 24

Fig. 3.1: Schematic of a typical intralaminar DCB specimen with the glued optical fiber on the upper surface (not to scale). 27

Fig. 3.2: (a) Compliance vs. crack length for different calibration methods, $H = 10$ mm. (b) Resulting R-curves for different compliance calibration methods, $H = 10$ mm. These data are from the thermoset composite system..30

Fig. 3.3: (a) J-integral definitions for DCB under end opening forces. (b) J-integral definitions for DCB under a pair of forces, i.e. a pure-moment configuration.............31

Fig. 3.4: (a) Perspective cross-section of a typical single mode optical fiber (b) Typical FBG wavelength interrogator apparatus; schematic modified from [98].....................36

Fig. 3.5: Photo of a glued optical fiber on the upper surface of a specimen and microscopy of cross-section. 37

Fig. 3.6: Typical FBG wavelength interrogator apparatus; schematic modified from [98]...37

Fig. 3.7: Typical OLCR based apparatus measuring; schematic modified from [98]......38

Fig. 3.8: Typical FBG position tracking, based on OLCR reflected light intensity measurements..39

Fig. 3.9: Schematics of the numerical model used for the identification scheme: (a) Half DCB model, assuming symmetry. (b) Complete DCB model (arms may be symmetric or not)..41

Fig. 3.10: Schematic of the numerical model used for the identification scheme under presence of finite process-zone 45

Fig. 3.11: Definition of the traction-separation relation used in the cohesive zone modeling..47

Fig. 3.12: Map of the implemented experimental/numerical characterization methodology. 50

Fig. 4.1: Consolidation cycle applied (temperature and pressure) at the AS4/PPS composite..52

Fig. 4.2: (a) Fractured DCB SP1 and (b) transverse-section, optical microscopy in the fully developed bridging zone. 54

Fig. 4.3: Crack propagation and the development of bridging: photographs of a specimen and snapshots from the micromechanical numerical model at $a = 61$ mm (i), 70 mm (ii) & 85 mm (iii); as published in [67]..54

Fig. 4.4: (a) Strains versus time recorded by the FBGs. (b) Experimental strains and optimized numerical strain profiles at $a = 110$ mm; as published in [67]. 55

Fig. 4.5: (a) Traction-separation relation inside the bridging zone. (b) Overall traction-separation relation calculated from the inverse method and corresponding profile from the micromechanical model; as published in [67]. 57

Fig. 4.6: Experimental and numerically obtained load-displacement response. The SP 2 & 3 are unloaded at the end of the test; as published in [67]. 58

Fig. 4.7: (a) Experimental setup to acquire the rotation at the loading points. (b) Experimental and numerically obtained load-rotation response (see text for details); as published in [67]. 58

Fig. 4.8: (a) Experimental R-curves compared to numerically predicted R-curves (see text for details). (b) Experimental R-curves and numerical ones, using the SS-MCC method, $J^{(\theta)}_{total}$ and the calculated traction-separation relation; as published in [67] ... 59

Fig. 4.9: R-curves from experiment and the virtual testing using MCC, SS-MCC and $J^{(\theta)}_{total}$; as published in [67] 61

Fig. 5.1: Stress–strain response of the Gurit SP™ thermoset material, under transverse tensile test; as published in [55]. 65

Fig. 5.2: Typical side views of fractured specimens of all tested thicknesses; as published in [55]. 66

Fig. 5.3: Fracture surfaces and transverse-sections in the bridging zone at fully developed steady-state for (a) $H = 6$ mm (b) $H = 10$ mm; as published in [55]. 66

Fig. 5.4: Load-displacement curves for specimens $H =$ 6, 10 and 14 mm and typical unloading response at the end of the test 67

Fig. 5.5: (a) Strains versus time recorded by the FBGs for specimen $H = 6$ mm. (b) Strains versus distance from crack tip shifted to $a = 107$ mm for specimen $H = 6$ mm; as published in [55] 68

Fig. 5.6: Experimental strains and optimized numerical strain profiles; as published in [55]. 69

Fig. 5.7: Calculated bridging tractions profiles. 70

Fig. 5.8: Calculated traction-separation relations; as published in [55] 70

Fig. 5.9: Bridging zone length, exponential softening parameter and maximum angle at the end of bridging zone versus specimen thickness; as published in [55]. 71

Fig. 5.10: Experimental and corresponding numerically obtained load-displacement response; as published in [55]. 72

Fig. 5.11: Averaged R-curves, per specimen thickness. The first point indicates the fracture toughness of the composite; as published in [55]. 72

Fig. 5.12: Experimental R-curves compared to numerically predicted R-curves (see text for details). 73

Fig. 5.13: Experimental R-curves using the DCC method and R-curves based on calculated traction-separation relations (see text for details).....................................74

Fig. 6.1: (a) Pure moment test-rig configuration. (b) Schematic of the numerical model with the DCB geometry employed to evaluate the design parameters. (c) Photograph of an actual $H = 10$mm specimen at the end of the experiment. 79

Fig. 6.2: Numerical calculation of J_{tip} for different precrack lengths...........................80

Fig. 6.3: Typical specimen with speckle pattern, ready to test ($H = 10$mm)................82

Fig. 6.4: (a) Drawing of the pure moment test rig and detail of the goniometer. (b) Comparison of the actual measured angle with the one acquired from the kinematic model by the CAD...84

Fig. 6.5: (a) Specimen's force diagram. (b) Equivalent moment diagram.....................85

Fig. 6.6: (a) Snapshot of the FE model, with σ_z results and boundary conditions indicated. (b) R-curves based on the response of the cohesive element model, with the pure moment conditions and corresponding response from the EOF identification ($H = 10$mm) 88

Fig. 6.7: (a) Experimental R-curves batch #2, PM by CC and EOF by MCC, and identified $J_{total-SS}$ in EOF. (b) Photograph of specimen during fracture test ($H = 10$mm). 89

Fig. 6.8: (a) Measured angles from DIC vs. estimation using Beam Theory. (a) Typical photograph used in DIC to measure the curvature of the specimen. 89

Fig. 6.9: Experimental R-curves, by CC , $J_{total-PM}$ and $J^{(\theta_1,\theta_2)}_{total,PM}$ 91

Fig. 6.10: (a) Moment – angle ($\theta/2$) response, experiments, cohesive and micromechanical model; see text for details. (b) Experimental R-curves, SP2- PM-#2, by CC, compared with R-curves from micromechanical model...................................92

Fig. 6.11: Experimental R-curves, SP2- PM-#2, by CC, compared with R-curves from micromechanical model (modified); see text for details...93

Fig. 6.12: (a) Moment – angle ($\theta/2$) response, experiments from batch #3. (b) Experimental R-curves by CC, per specimen thickness; batch #3.................................94

Fig. 6.13: Fractured surfaces and recorded profile of specimens tested in PM ($H =$ 10mm); (a) DCB from batch #2. (b) DCB from batch #3. 95

Fig. 6.14: Cross-section views from specimens tested in PM ($H =$10mm); (a) DCB from batch #2. (b) DCB from batch #3. 96

Fig. 7.1: Schematic of a 5-SQ DCB specimen. 99

Fig. 7.2: Bottom: Typical neat GFRP with a schematic of an optical fiber bonded on the surface. Top: Typical neat GFRP specimen reinforced with PMMA beams. 100

Fig. 7.3: (a) Side and top view of DCB, neat GFRP specimen instrumented with an optical fiber. (b) Side and top view of DCB, tufted GFRP specimen. 102

Fig. 7.4: (a) Photograph of fractured neat GFRP with PMMA specimen and SEM detail. (b) Photograph of fractured tufted GFRP specimen and SEM detail. (c) Microscopy of an inserted tuft. 103

Fig. 7.5: (a) Experimental R-curves by MCC, of neat GFRP; with and without PMMA reinforcement. (b) Experimental R-curves by $J_{total}^{(\theta)}$, of neat GFRP; with and without PMMA reinforcement. 104

Fig. 7.6: (a) Strains versus time recorded by the FBGs. (b) Experimental strains and optimized numerical strain profiles at $\Delta a =$ 30 mm. 105

Fig. 7.7: Calculated tractions profiles. 107

Fig. 7.8: (a) Overall traction-separation relations. (b) Experimental R-curves and numerical ones, using the calculated traction-separation relations.......................... 108

Fig. 7.9: Experimental and numerically obtained load-displacement response. 108

Fig. 7.10: (a) Experimental R-curves by MCC, of 5-SQ GFRP; read text for details. (b) Experimental R-curves by $J_{total}^{(\theta)}$, of 5-SQ – 2 DCB specimen. 110

Fig. 7.11: (a) Uniaxial pulling testing setup and fractured surface: photographs and SEM. (b) Experimental load-displacement response, normalized pet tuft and mean approximation. 111

Fig. 7.12: (a) Snapshot of the FE model with key-regions and boundary conditions indicated. (b) Experimental and modeled load displacement response.................... 114

Fig. 8.1: Calculated traction-separation relations as a function of CODs and local angle, per specimen thickness; UD carbon/epoxy system. 119

Fig. 8.2: Calculated traction-separation relations as a function of CODs and local angle, per investigated stiffness; Woven GFRP system. 119

Fig. I.1: (a) Definition of the contour J-integral in presence of bridging tractions. (b) Domain integral definition. 123

Fig. I.2: Resulting values of J_{tip} for different contours, with and without bridging, $H =$ 10mm; as published in [55]. 125

Fig. II.1: (a) Fabrication mold in the autoclave. (b) Fabricated composite plate. (c) Specimen precracking. (d) Specimen and loading block, prepared for bonding. (e) Specimens ready to test. (f) Specimen mounted on the testing machine..................127

Fig. II.2: (a) Cross-section of the fabricated carbon/epoxy composite used for void calculation. (b) Microscopy of the pre-crack tip. 128

Fig. III.1: R-curves per thickness, and cross-sectional micrographs; Carbon/thermoset composite 130

Fig. III.2: Bundle and bulk fracture surface analysis, $H = 10$mm, carbon/thermoset system: (a) Microscopy of cross-section and approximated fracture profile. (b) Approximated fiber-bundle area and fracture profile. 131

Fig. III.3: Microscopy of cross-section for bundle and bulk fracture surfaces investigation, AS4/PPS. See also Fig. 4.2(b). 132

Fig. IV.1: Photograph of the complete experimental setup at the end of an experiment. 133

Fig. IV.2: Drawing of the assembled specimen gripping mechanism..........................134

Fig. IV.3: Assembled housing of the radial bearings and its connection with the carriages of the linear bearings. 135

List of Tables

Table 1: Material Properties-Engineering constants of woven cross-ply GFRP (Bold: experimental, Underline: modal analysis, rest literature [2]). 99

Table 2: Mean aproximated behavior per tuft and per connector element.............. 113

List of Symbols

a	Crack length
a_0	Pre-crack length
A_1, A_2	Fitting parameters of MCC
A_i^*	Domains for J-integral calculation
B	Specimen’s width
C	Specimen’s compliance
$D(\delta)$	Damage parameter, as linear stiffness degradation of the cohesive elements
f	Error function of the optimization scheme
f_{pz}	Error function of the optimization scheme with finite process-zone
f	Correction factor for end block effects.
$f_{ij}(\vartheta)$	Dimensionless functions of the angle, for SIF
F	Principal reaction force at PM
F_A	Compressive force applied to each arm of the specimen for PM
F_B	Opening force applied to each arm of the specimen for PM
$F_{c,X}$	Reaction force of the connector (tuft-row) at each key-point X
E_i	Young moduli on direction i
G	ERR for LEFM
G_{ij}	Shear moduli on plane ij
$G_{IC}, G_{IIC}, G_{IIIC}$	Critical energy release rates (ERRs) for each fracture mode
$G_{I,i}$	Initial fracture toughness, linear elastic, Mode I

$G_{I,b}$	Energetic contribution of bridging, linear elastic, Mode I
$G_{II,i}$	Initial fracture toughness, linear elastic, Mode II
G_{total}	Total energy release rate, linear elastic
G_{ss}	Energy release rate at steady state, linear elastic
h	Thickness (or height) of each DCB arm
H	DCB specimen's total thickness (or height)
I	Area moment of inertia
J	ERR by J-integral
$J_{I,b}$	Energetic contribution of bridging, general case, Mode I
J_{pz}	Energetic contribution of the process-zone
J_{tip}	ERR by means of numerical J-integral
J_{total}	Total ERR, general case
k	Bending stiffness, flexural rigidity
K_{IC}, K_{IIC}, K_{IIIC}	Critical stress intensity factor for each fracture mode
K_c	Initial stiffness of connector elements
K_0	Initial stiffness of cohesive elements
L	Lever's length of pair of forces on the rails
ℓ	Lever's length of pair of forces on the specimen
ℓ_c	Process-zone length
M	Reaction moment per DCB arm in PM
n	Refraction index
n_{eff}	Mean core refraction index
p_e	Experimental optomechanical grating gage factor
p_{ij}	Pockel's strain–optic constants
P	Reaction force
$\Re$	Fitting parameter in CC
T_i	Body tractions

r	Radial distance from crack tip
u_i	Local displacements in direction i
U	Strain energy
V_f	Fiber volume fraction
w	Strain energy density
W	Work of the external forces
x	Correction factor for orthotropy
z	Bridging zone coordinates/axis parallel to bending elastic line
$z_{\max}$	Bridging zone length
z_0	Length of the process-zone
α_f	Thermal expansion coefficient of optical fiber
γ	Traction profile exponent
Γ	Open contour
$\varDelta$	Applied displacement, cross-head displacement
δ	Crack opening displacement, COD
$\delta_{c,X}$	Relative displacement of the two connector’s nodes (tuft-rows) at point X
$\delta_{\max}$	COD at the end of the bridging zone
δ_1	COD at the end of the process-zone
ε_{ij}	Strains on directions ij
$\varepsilon_{\exp}$	Longitudinal experimental strain distribution
ε_{FEM}	Longitudinal numerical strain distribution
η	Fitting parameter in CC
θ	Relative rotation at the loading points of DCB
ϑ	Angle in polar coordinates
Λ_0	Period of the induced index modulation
$\lambda_{\mathrm{B0}},\lambda_{\mathrm{B}}$	initial Bragg wavelength, Bragg wavelength
μ	Rolling friction coefficient of liner bearings

ν_{ij}	Poisson’s ratio on directions ij
ν_f	Poisson’s ratio of optical fiber
ξ	Thermo-optic coefficient
Π	Potential energy
ρ	Crack tip radius
σ_c	Critical strength of the cohesive elements (transverse tensile strength of the composite)
$\sigma_{\max}$	Maximum bridging traction
$\sigma_{bf,\max}$	Fiber bundle strength
$\sigma_b\left(z\right)$	Bridging tractions over position
$\sigma_{pz}(z)$	Closing traction within the process-zone
$\hat{\sigma}(\delta)$	Traction-separation relation
$\hat{\sigma}_b(\delta)$	Traction-separation relation inside the bridging zone
$\hat{\sigma}_{pz}(\delta)$	Traction-separation relation inside the process zone
χ	Crack length’s variation parameter
Ψ_{tuft}	Damage energy per tuft

List of abbreviations

CC	Compliance calibration
CCD	Charge-coupled device
CFRP	Carbon fiber reinforced polymer
COA	Crack opening angle
COD	Crack opening displacements
DCB	Double cantilever beam
DCC	Double (or segmented) compliance calibration
DIC	Digital image correlation
ELS	End-loaded-split
EOF	End opening forces
ERR	Energy release rate
FBG	Fiber Bragg grating
FE	Finite element
FPZ	Finite process-zone
FRP	Fiber reinforced polymer
FWHM	Full width at half maximum
GFRP	Glass fiber reinforced polymer
LEFM	Linear elastic fracture mechanics
LSB	Large scale bridging
LVDT	Linear variable differential transformer
MCC	Modified compliance calibration

PM	Pure moment
PMMA	Polymethyl-methacrylate
PPS	Polyphenylene sulfide
R-curve	Resistance curve
SEM	Scanning electron microscope
SIF	Stress intensity factor
SLSR	Side lobe suspension reflection intensity
SMF	Single-mode optical fiber
SP	Specimen
TTR	Through the thickness reinforcement / reinforcing
UBM	Uneven bending moments
UD	Unidirectional
UV	Ultraviolet

Chapter 1

Introduction

1.1 General foreword & motivation

Current demands for higher energy efficiency and reduction of the ecological impact of modern transportation systems and structures, along with the ascending security standards, push the global engineering community towards lighter yet, safer than ever structures. In order to fulfill these stringent requirements, the solutions proposed are more and more based on advanced materials, with composite architecture. Amongst the composite materials, the fiber reinforced polymers (FRPs) are gaining greater share of the global market. The most accessible form of FRPs from an economical aspect, are the glass-fiber reinforced polymers (GFRPs), followed by the aramid FRPs and carbon fiber reinforced polymer (CFRP) composite materials. Nonetheless, CFRPs are gaining their share in structural components for aerospace, automotive, marine and infrastructure applications, due to their superior mechanical properties. Some statistics concerning the market share of CFRP composites are included in Fig. 1.1, where it is shown that the wind-turbine construction industry is the leader followed by the aerospace and defense sectors.

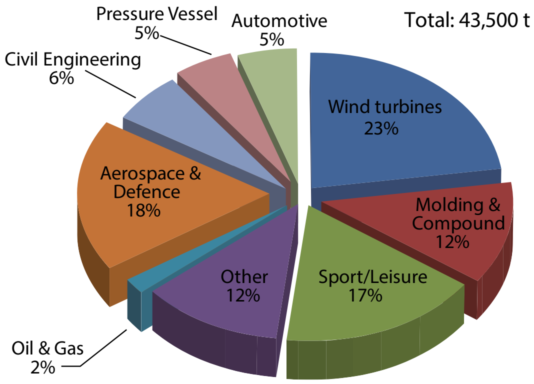

Fig. 1.1: Global carbon fiber consumption (tons) by application (2012) [1].

Composite materials are defined by their very high specific stiffness, and strength, with certain CFRP composites to exhibit for instance higher stiffness (over 210 GPa) and strength (over 2000 MPa) compared with metals, even in absolute numbers (i.e. regardless of their density). Due to these characteristics, the use of composite materials in wind-turbines, aircrafts, vehicles, marine vessels etc. provides superior energy efficiency with weight gain of 40-50% or higher, while composites enable space and biomechanical applications that were simply impossible before their invention. However, structural engineers have only recently taken full advantage of the composite architecture of these materials. Initially, the idea was simply to substitute metallic parts with others made of composite materials, like for instance aluminum with CFRP parts, creating the so called black aluminum, leading to severe overdesign. Moreover, FRPs are highly orthotropic materials; in other words they exhibit these extraordinary properties in particular directions and this fact has to be taken into account, in order to maximize the benefits that these materials can provide.

The anisotropic character of composites materials and FRPs in particular, is also reflected in their low initial fracture toughness, which is a critical feature of concern in structural design, compared to the metallic structures which are quite tolerant in cracking, due to plasticity prior failure. This low initial fracture toughness is associated to their composite nature (fiber-matrix interface, cohesive failure) and the low properties of their polymer matrix (adhesive failure). Fracture of these materials initiates and propagates predominantly within resin epoxy zones, since the matrix is by far the weakest component and failure mainly appears in matrix-fiber interfaces. As a result, these materials are prone to failure in planes parallel to the direction of the fibers. For this reason laminated composites can exhibit extended delamination while woven-fabric composites exhibit diffused damage (see [2,3] and references therein). At the microscale level, interfacial and matrix damage initiates under tensile and shear loads, leading to delamination and intralaminar cracking, before the ultimate tensile failure of the fibers [4], while compressive loads may lead to formation of kink bands with fibers to fail first [5] depending on the fiber orientation in the composite (Fig. 1.2(a)).

Nevertheless, crack propagation paths parallel to fibers' direction, after matrix and interface failure, lead in several cases to fiber bundles being pulled out of the composite, bridging the two cracking faces, and forming the so called, fiber bridging (Fig. 1.2(b)), which acts as a very important toughening mechanism. In particular, under mode I fracture, the resistance to crack growth is highly assisted by extensive large scale fiber bridging (LSB) (as reported in [6,7,8,9,10,11,12] etc.) due to the induced closing tractions opposed to the crack opening.

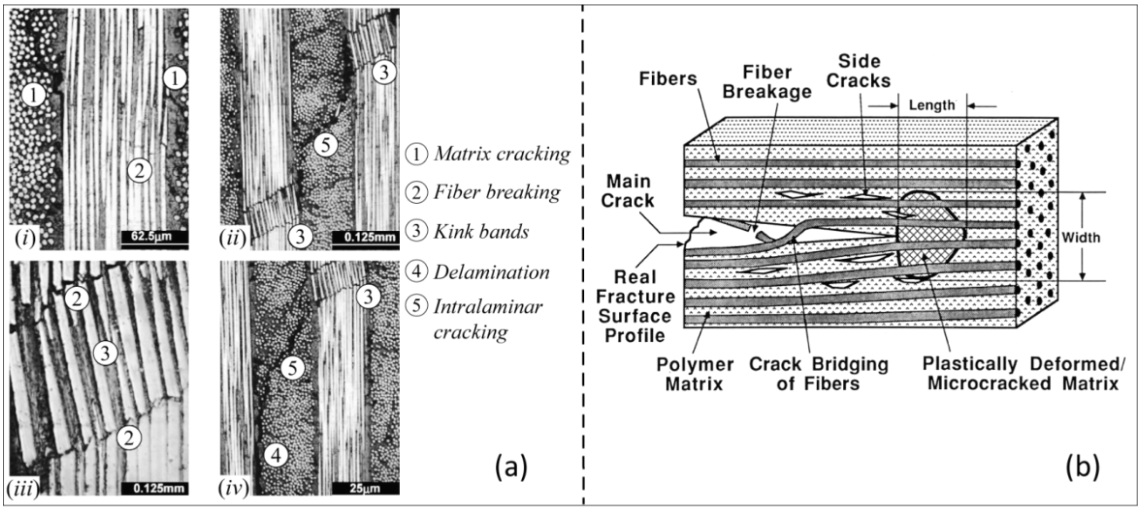
(i)
62.5μm
(ii)
0.125mm
(iii)
0.125mm
(iv)
25μm
① Matrix cracking
② Fiber breaking
③ Kink bands
④ Delamination
⑤ Intralaminar cracking
(a)
Fibers
Fiber Breakage
Side Cracks
Length
Main Crack
Width
Real Fracture Surface Profile
Polymer Matrix
Crack Bridging of Fibers
Plastically Deformed/ Microcracked Matrix
(b)

Fig. 1.2: (a) Failure mechanisms' micrographs, in a cross-ply laminate (compact tension specimen at the compression side); modified from [5]. (b) Schema of possible energy absorption mechanisms during crack growth of a UD laminate [3].

As a consequence, characterization of such toughening phenomena, like LSB, is of high importance in order to reduce over-design in composite structures and promote the damage tolerant design principles. Therefore, complete characterization of the bridging phenomena and calculation of the exact bridging traction's profile during crack propagation, provides important tools for the engineering design community. Significant fiber bridging phenomena may occur in both thermoset and thermoplastic matrices as well as with other type of matrices (metallic or ceramic). Yet, for the time being, the majority of structural designers define the end of components' life by the appearance of any sort of micro-crack (first-ply failure criteria), mainly due to lack of reliable characterization schemes.

Apart from the LSB which is formed due to the intrinsic architecture of the laminated composites, through the thickness reinforcing techniques, such as stitching, z-pinning or tufting may have similar, or more significant toughening effects, compared to LSB, due to the opposing closing tractions. Due to the similarity between these toughening phenomena, the experimental characterization techniques can be analogous.

For a laminated composite material, a crack starter may lie on a plane parallel to the laminas forming an interlaminar crack causing delamination fracture. On the other hand, two types of crack starters inside a unidirectional (UD) lamina may be distinguished: i) an intralaminar crack, being normal to the lamina plane and parallel to the fibers and ii) a translaminar crack being normal both to the lamina and the fibers. The last two may be found in the literature as lamina splitting, too, while translaminar and intralaminar in the international literature may also refer to through the thickness cracks in multidirectional laminated composites. A schematic representation of these reported definitions, used throughout this document, is depicted in Fig. 1.3.

Significant results have been reported on the delamination mechanisms of UD laminates [8,11,12,13,14] using different approaches. However, investigations into intralaminar fracture have not yet received the same level of attention owing to a lack of standards in introducing the precrack and the extent of LSB during fracture [9,10,15,16,17]. Nonetheless, intralaminar fracture propagation of a structural component remains a very probable scenario, since it may be initiated by defects introduced by machining processes like milling, sawing, drilling, etc., or stress concentrations in structural components, or part of extended delamination in multidirectional laminated composites. In addition, scale and geometrical effects related with the bridging phenomena have been reported since 1989 [6], without receiving significant attention, probably due to the underlying complexity of the matter, until recent studies came up with substantial experimental evidence and some scaling prediction guidelines propositions [14,18].

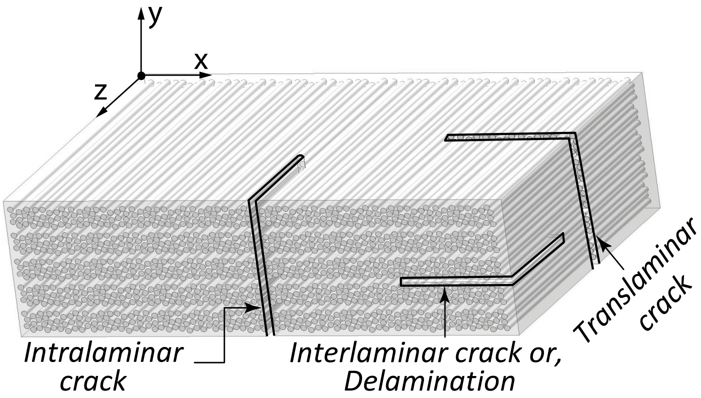

Fig. 1.3: Definition of intralaminar, interlaminar and translaminar crack.

1.2 Objective

Several studies have been conducted and new ones will continue to appear in the literature concerning the failure of composites materials, due to the large amount of effort needed for their characterization, originating from their anisotropy and their complex failure mechanisms.

The scope of this work is to propose and attest characterization techniques on fracture resistance of laminated composites, with focus on the effects of scale and loading conditions, on the traction-separation relations related to LSB phenomena under mode I intralaminar fracture of CFRPs. Moreover, this work aims to verify the applicability of the proposed methodology, on the characterization of mode I delamination fracture in a laminated, woven fabric GFRP composite, with tufting through the thickness reinforcement (TTR).

To fulfil this objective the following tasks are carried out:

Intralaminar fracture of a CFR-thermoplastic

- Identification of the traction-separation relation using a combined inverse experimental/numerical approach.
- Comparison of the inverse identification results with the corresponding ones from a micromechanical model based on the embedded cell approach.

Intralaminar fracture of a CFR-thermoset

- Characterization of traction-separation relations using a combined inverse experimental/numerical approach focusing on the identification of scale effects by varying specimens' thickness, to establish an approach based on the flexural rigidity of the specimen.
- Designing a novel test-rig capable of implementing mode I opening conditions with pure bending moments to be used on depicting the effect of loading conditions on the fracture resistance.

Delamination response of a 3D reinforced laminated woven GFRP

- Fracture resistance characterization by extending the proposed methodology and existing techniques.

1.3 Thesis outline

After this brief introduction (Chapter 1), this thesis is organized in the following chapters:

Chapter 2 introduces some general concepts and definitions in fracture, reviews the characterization techniques on R-curve phenomena and the identification of tractions-separation relations, focusing on the particular aspects of FRPs due to LSB and presents the concept of TTR. Moreover, in this chapter numerical micromechanical techniques are reviewed, followed by a discussion on the fracture testing configurations proposed in the literature.

Chapter 3 contains a thorough description of the experimental and numerical methodologies employed in this study. Also presented in this chapter are, the fracture testing and fractography procedures, the energy release rate (ERR) calculation methods, the strain acquisition techniques and all the numerical methods used in the traction-separation relations characterization and load history prediction.

Chapter 4 deals with the characterization of LSB phenomena in mode I intralaminar fracture of a UD carbon fiber reinforced thermoplastic. Here, an already developed semi-experimental technique based on strain measurements by FBG sensors, is adapted to the needs of the current study and is employed to identify the traction-separation relation. The identified traction-separation relation is used to calculate the ERR and evaluate the resistance curves (R-curves) associated with LSB of this fracture response. The outcome of the identification scheme is compared with the corresponding results from a numerical micromechanical model.

Chapter 5 presents the characterization of the intralaminar fracture of a UD carbon/epoxy composite and is devoted in the evaluation of the effect of specimen thickness on the developed closing tractions due to LSB. Here, conventional DCB specimens of three different thicknesses, loaded with end opening forces are employed to conduct the characterization. In this chapter, the effects of specimen's thickness on the three identified traction-separation relations are presented while a scaling relationship expressed as a function of the bridging traction profile exponent and the flexural rigidity of the specimen is shown. Moreover, a discussion on the impact of LSB on the maximum ERRs is included comparing the two investigated materials.

Chapter 6 comprises the design and the implementation of a testing apparatus able to apply pure moments on the bending arms of DCB (double cantilever beam) specimens, by means of pairs of forces. The results of the fracture characterization of the mentioned carbon/epoxy system with this testing setup are included in this chapter. Here, the results from the end opening forces and pure moment conditions are compared to investigate of the effect of loading condition. Moreover, some discussion on the influence of the fabrication procedures and microstructure, in the formation of LSB, is addressed.

Chapter 7 is devoted on the investigation of the traction-separation relations in delamination of a woven GFRP with and without tufting TTR. Accordingly, a generalization of the relation between the closing traction profile and the flexural rigidity of the DCB arms is attested and a concise modeling approach for the load history prediction is proposed comprising the effects of LSB and TTR.

Chapter 8 summarizes the concluding remarks of this study and presents the future perspectives of research in this domain.

Chapter 2

State of the art

2.1 General definitions in fracture

Structural components may inherit defects, during their production or their functional life, as structural discontinuities which upon loading may eventually form cracks. Fracture mechanics deals with the propagation and the stability of cracks.

According to traditional fracture mechanics, three fracture modes, depending on the loading direction, may be distinguished: (i) mode I: where the crack faces separate in an opening manner, (ii) mode II: where the crack faces are shearing in-plane, against each other, & (iii) mode III, where the crack faces are shearing out of plane (tearing). The fracture modes definition is depicted in Fig. 2.1. Moreover, complicated loading cases can be analyzed as mixed-mode cases with components of each mode. The characterization of the fracture is made by means of the energy needed to create new fractured surfaces, namely, the crack propagation strain energy release rate (ERR), while for cases that can be considered as linear elastic, the stress intensity factor (SIF) may also be used as a characterization tool.

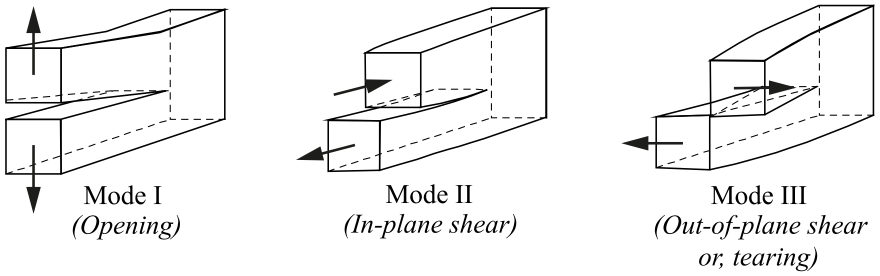

Fig. 2.1: Definition of fracture modes.

The stress field, $\sigma_{ij}\left(r,\vartheta\right)$, around a perfect crack, in polar coordinates (r is the radial distance from the crack tip) is proportional to the SIF, K, and is expressed as:

$\sigma_{ij}\left(r,\vartheta\right)=K\left(2\pi r\right)^{1/2} f_{ij}\left(\vartheta\right)$, with $f_{ij}\left(\vartheta\right)$ being dimensionless functions of the angle, ϑ, of the polar coordinates. K depends on the loading and boundary conditions, while a subscript note denotes the fracture mode, i.e. K_I, K_{II}, K_{III}. Thus, the stress field at the crack tip ($r \to 0$) is considered singular. The main consequence of the assumptions of the linear elastic fracture mechanics (LEFM) is the validity of the superposition principle. In other words a complex case can be treated as superimposed simple cases, with the total critical SIF to be equal to the sum of the others as depicted in Fig. 2.2.

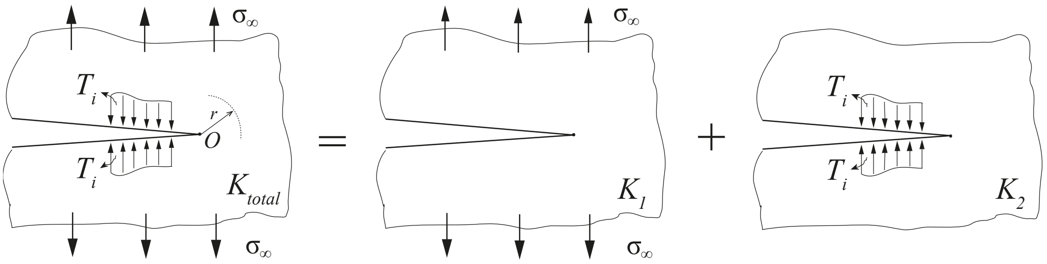

Fig. 2.2: Superposition principle in LEFM

The establishment of the SIF and the corresponding stress field enables the characterization of a structural component with a testing coupon as shown in Fig. 2.3. Nevertheless, the described stress field with the $1/\sqrt{r}$ singularity applies to linear elastic, brittle material and for the singularity dominated zone as depicted in the detail of Fig. 2.3, [19]. As a result the process or yielding zone at the tip has to be small (small scale yielding) compared to the crack length to consider LEFM. When this condition is not satisfied the stress field and its singularity varies.

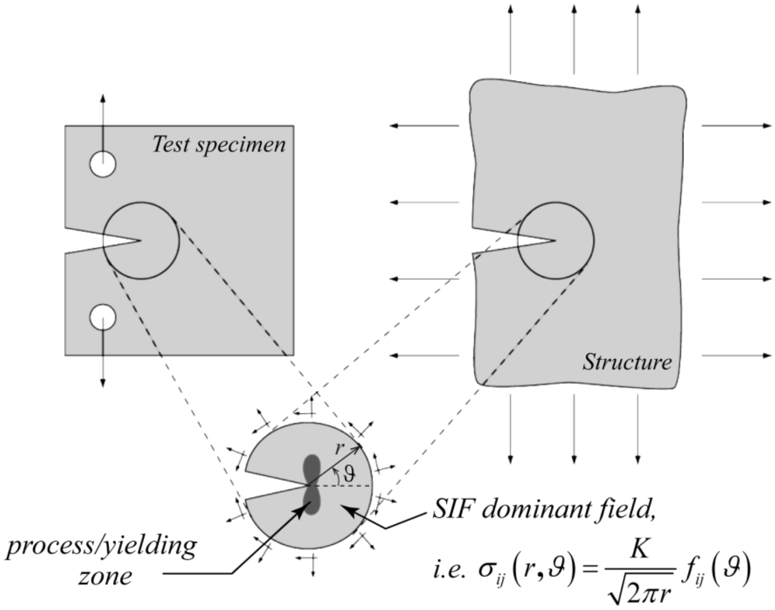

Fig. 2.3: Test specimen and real structure stress conditions. The detail shows the singularity dominated zone; courtesy of [20].

2.2 Traction-separation relations and R-curves

As it is already described, the basic fracture mechanics concept considers infinitesimal process-zone ahead of the crack tip, thus it is applicable for brittle fracture cases. Nevertheless, many structural materials demonstrate a finite, non-negligible process-zone (FPZ) due to yielding, or other micromechanisms ahead of the crack tip. For such materials, like metals, that extensive yielding zone may appear, Dugdale [21], proposed a yield strip model for mode I fracture, assuming a profile of closing (cohesive) tractions with a constant value, equal to the plastic limit of these materials, accounting for perfect plasticity. This model, accounts for a virtual crack tip shift, equal to the process-zone. Two years later Barenblatt [22] proposed a model based on the same concept, accounting though for any type of stress profile that reaches a maximum value at the crack tip, with a softening behavior until the end of the process-zone. This model, describing a ductile or, quasi-brittle fracture, with a finite process-zone with a profile of closing tractions, is generally referred in the literature as the Dugdale-Barenblatt model [23,19]. Moreover, in the literature another type of quasi-brittle crack model is found, refer to as “crack-band” model [24], accounting for a softening traction’s profile ahead of the crack tip, without virtual crack shifting, with applications in materials such as concrete and natural rocks. All described models are depicted in Fig. 2.4.

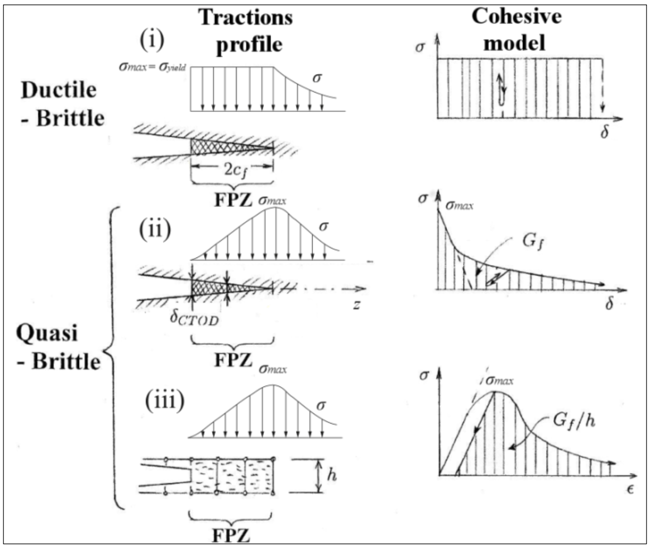

Fig. 2.4: Stress distributions and cohesive models for FPZ; modified from [24].

All these closing tractions' profiles, can be expressed as a function of the corresponding crack tip opening displacements (CTOD or, simply COD) forming the traction-separations relations, $\sigma(\delta)$, known also as cohesive laws, that are commonly considered material property. Using these traction-separation relations and by integrating the tractions over the CODs, the corresponding ERR (G or J) can be calculated. The existence of the FPZ and the evolution of the traction-separation relation is depicted on the measured ERR as an increase in the values, starting from a critical ERR followed by escalating numbers, leading to higher fracture resistance. Under stable crack propagation the resistance will increase up to a maximum, plateau state that the tractions evolve in a self-similar state as crack advances. The increase in fracture resistance or, in other words the evolution of the ERR from the initial critical value (G_C), as a function of the crack advance, is depicted in the so called, crack growth resistance curves (R-curves), for a corresponding fracture mechanism of a materials or, a structural component (see Fig. 2.5). The stability of the crack propagation is related to the stress state of a specimen or component. Thus, if the loading conditions result to ERRs lower than the critical value, the crack is stable. Now if the loading rate is lower or equal to the load defined by R-curve the crack propagates in a stable manner. On the other hand, if the loading rate is higher than the rate defined by the R-curve the crack propagates in an unstable mode (see Fig. 2.5).

Given that the traction-separation relation is not known a-priori since the closing tractions cannot be measured directly, the traditional methods to predict the traction-separation relations are based on the experimentally calculated R-curves. Nevertheless, even if the traction-separation relations are unidentified, the R-curves solely are important tools to describe the fracture response of a material, since the absolute values depicted and the shapes are often sufficient to classify materials and structures or, pinpoint improvements on an existing material.

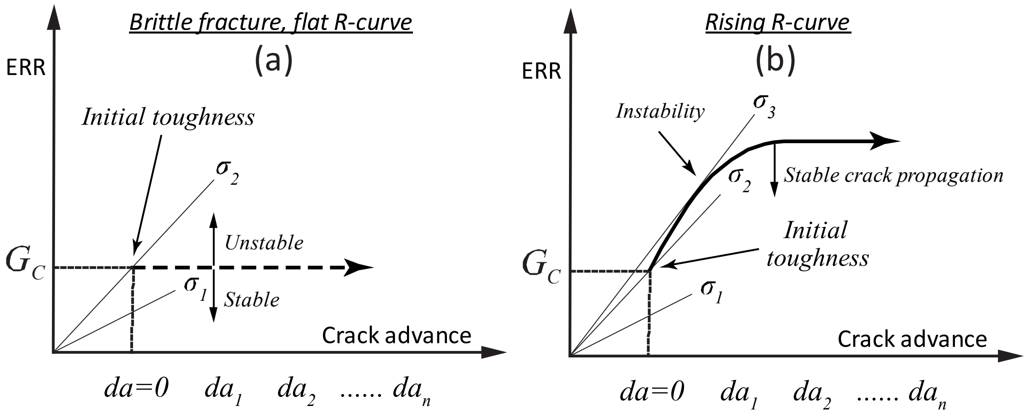

Fig. 2.5: Crack stability: (a) Brittle fracture. (b) Typical rising R-curve behavior.

2.3 Failure of fiber reinforced composites and LSB

Fiber reinforced composite materials of any matrix (ceramic, polymer or metallic) demonstrate complicated failure mechanisms with an initial brittle, quasi-brittle or ductile fracture followed by evolution of damage. Depending on the nature of the material, the process-zone may be infinitesimal or finite, while crack propagation leads to creation of a discernible damage zone. This damage zone is created mainly due to, either intact fibers that are bridging the crack faces, for cracks transverse to fiber’s direction (translaminar fracture), or from fibers that our pulled out of the composite for cracks planes parallel to fiber’s directions (interlaminar and intralaminar fracture, see Fig. 1.2 and Fig. 1.3). LSB may be dominant for mode I loading cases, while it is negligible in mode II loading conditions. Nevertheless, the vast majority of crack advancement in structural components occurs under mixed mode conditions where the effect of fiber-bridging is significant [25,26,27,28,29], yet reduced compared to simple mode I cases.

The fracture of a composite material, as already described, is characterized by significant toughening phenomena that can be reflected in R-curves. When LSB occurs, the R-curve is not sufficient to describe the fracture response, since it is affected by the loading conditions and specimen’s geometry. Therefore, efforts are devoted in establishing the physically based traction-separation relations, or so-called “bridging laws”, to model the effect of the bridging fibers with closing tractions along the bridging zone. These traction-separation relations of the bridging zone, $\hat{\sigma}_b(\delta)$, are essential in order to predict the fracture response and develop fracture tolerant design methods. An overall tractions profile under LSB contains the traction over an infinitesimal, or a FPZ followed, by the tractions corresponding to the LSB effect, while the stress decay ahead of the tip depends on the crack singularity and the far-field stress-state. A typical tractions’ profile, in mode I with LSB is schematically depicted in Fig. 2.6.

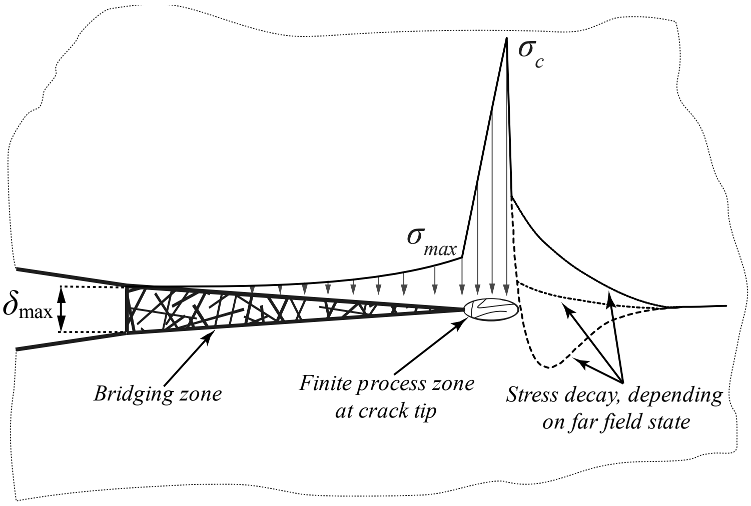
σ_c
σ_{max}
δ_{max}
Bridging zone
Finite process zone at crack tip
Stress decay, depending on far field state

Fig. 2.6: Closing tractions profile, with bridging and FPZ.

2.3.1 Fiber bridging and characterization techniques

To characterize the bridging tractions profile, two methods are mainly proposed in the literature:

a) The most commonly used method [8,9,10,15], is based on measurements of the CODs at the crack starter, during fracture and calculations of the ERR, relying on the direct application of Rice’s J-integral approach [30]. On this scheme, the derivative of the ERR with respect to experimentally acquired CODs, δ, is utilized to produce the traction-separation relation and may be referred as the direct method. One of the drawbacks of this method is that the resulting traction-separation relation can be significantly influenced by the accuracy of the COD measurements [31]. For this reason, apart from the older studies that employ extensometers for the COD measurements [9,10], electronic speckle pattern interferometry is investigated [32], while in more recent studies [33,34], digital image correlation (DIC) is considered, aiming at improving the accuracy.

Moreover, provided that the traction-separation relation usually consists of high stress gradient near the crack tip, and nearly asymptotic fields towards the tail, a fitting scheme is usually adopted for the ERR-COD data prior the derivation in order to increase the accuracy, making though the whole approach sensitive to the chosen fitted function [35,36].

b) Alternatively, an indirect method is lately proposed [11,12,18,35] based on internal quasi-distributed strain measurements by means of graded optical fibers, during delamination. According to this method the traction-separation relation is calculated using an inverse scheme where a variable bridging tractions profile is applied on a numerical model and the objective tractions' profile is identified by optimizing the difference between the experimentally measured and simulated strains. This scheme is applied for one point at the steady-state of propagation, to include the fully developed bridging profile. The result of this approach is a traction-separation relation unbiased from any experimental R-curve, while the ERR can be calculated using the integral of the bridging tractions over the CODs, as it is proposed in the current study.

The former method uses experimental COD measurements, which can become quite unreliable due to experimental scatter, as it reported in other studies [32]. Therefore, the latter method is acknowledged as more accurate, employing high precision experimental strain data along the delamination direction, rendering a reliable identification. The key feature of the latter method is the use of the multiplexed FBG sensors that provide quasi-continuous strain measurements during the fracture experiment. The optical fibers with inscribed FBGs used in this scheme have many other strain monitoring applications such as monitoring of curing processes (e.g. [37]), impact health monitoring (such in [38]) general structural health monitoring (e.g. [39]) and many others as reported in this review article [40]. The main advantage of the FBG sensors is their potential of embedding them inside the composite material during the fabrication procedures and the multiplexing of 10 or more sensors on the same host fiber.

In both mentioned identification methods, a shape for the tractions profile has to be considered. In the literature simple linear or bilinear softening bridging laws are considered for convenience [8,41,42,43], while others use polynomial softening profiles [9,44]. The inverse method on the other hand assumes an exponential softening tractions profile, as a function of the crack length, while the traction-separation relation follows a similar trend. This exponential softening has a very flexible fitting formulation covering a wide range of potential tractions' profiles. Following the shape of traction-separation relations produced by the indirect method, a recent work [45], proposes an identification scheme where the ERR based on a variable traction-separation relation is optimized with the one obtained from conventional experimental R-curves. This approach is attempting to simplify the procedure and avoid some of the elaborate experimental identification steps.

The size of the specimen has been considered as a parameter from the very early studies of mode I fracture in DCB specimens [6,7], both as a function of thickness solely, or thickness and width, especially in multidirectional laminates [46], however, the experimental scatter did not allow for definition of a trend. The first work that reports some significant trend was published in 1993 [47], but these findings remained unconsidered probably for convenience, reducing the amount of experimental work to be conducted. Nevertheless, the majority of researchers consider a thickness effect on the initial slope of the R-curves, and all results agree on the fact that the higher the bending stiffness, the longer the crack extension needed to attain steady-state crack growth [8,9,10,15]. However, the bridging law is conventionally considered a unique relation, independent of specimen thickness, which implies a unique, steady-state ERR [8,9,13]. Recent studies [14,18] though, report a strong correlation between specimen thickness and maximum ERR, which leads to a different bridging law for each geometry, challenging the hypothesis of the traction-profile as a material property, when LSB is present. Yet, there is still room for improvement regarding the identification of the parameters that define the relation of the bridging laws with rigidity, or geometrical parameters. These effects are also highly connected with fibers' orientation, as reported in [48], correlating the effect of width in cross-ply laminates.

2.3.2 Comments on damage tolerance and other potentials

The current design strategies, avoid entering in a damage tolerant domain when it comes to FRPs due to lack of well-established characterization techniques, therefore leading to overdesign of structures. As a result, only the initial critical ERR may be considered at the designing stage, following for instance, the mode I characterization ASTM standard [49], where LSB is considered as an artifact of the experiment. Nevertheless, for highly demanding applications such as the ones in the aerospace domain, a less conservative approach is adopted. There (see [50]), a mean ERR of the first 100 mm of crack advancement is considered as a design parameter, incorporating practically all effects of LSB or other toughening phenomena, yet with an inclusive approach, avoiding to enter into the details of the complex fracture events. The corresponding ISO standard [51] is also on a similar track, i.e. reckons toughening phenomena at a mean ERR of 50mm crack advance and moreover, defines a very specific specimen geometry, serving in material classification, and not in damage tolerant design purposes.

The toughening LSB phenomena are reported in all kinds of laminated composites [52,53,54]. Significant studies have been reported, on the delamination mechanisms and intralaminar fracture of fiber-epoxy unidirectional laminates, using DCB specimens [8,9,35,12,55]. However, very few works have addressed the bridging phenomena on fiber reinforced composites with thermoplastic matrices [6,7,35]. According to these works the extent of LSB is comparable to the epoxy based composite systems with the triggering mechanisms being similar, since the matrix and the fiber-matrix interfaces both fail in a brittle manner. Moreover, in these materials the effects of LSB are highly beneficial, since the fiber-matrix interfacial bonding may be low, leading to very initial fracture toughness.

The damage tolerant design framework is highly assisted with the use of cohesive zone modeling in numerical methods and in particular with the introduction of cohesive FE elements [42] or cohesive surface numerical bonding and the XFEM tools [56], in commercial FE codes [57]. As a result, an engineer can model a cracked component, and introduce a cohesive element zone ahead of the crack and predict the residual life of the structure, provided that the traction-separation relations are already characterized for this case taking into account effects of geometry etc. Thus, identification techniques of toughening mechanisms such as LSB, can extent and enrich the damage tolerant design methodologies.

While there are numerus parameters, from a loading configuration aspect, affecting the fracture response, collective experimental results [52], demonstrate that the loading rates can be of secondary importance when the matrix demonstrates a quasi-brittle response, and the loading speed rates are out of the viscoelastic range or creep response. In other words, a quasi-static monotonic characterization can be applicable in some dynamic loading cases, albeit with loading rates far from the acoustic level, or the resonance of the structure. For example, in a very recent work investigating both interlaminar and intralaminar fracture under low-velocity impact [58], a quasi-static monotonically identified traction-separation relation is implemented, to predict successfully the experimental results of all fracture modes. Their applicability can even be extended in crash analysis, according to a published, combined academic-industrial work in applied crashworthiness design [59]. Hence, further understanding of the effects of stiffness, geometry and loading conditions under presence of LSB will have many applications in structural design.

2.4 Micromechanics and Virtual testing techniques

The described traction-separation relations, identified with either method (direct or indirect), are practically a homogenized representation of the creation and failure of the bridging ligaments, during the LSB phenomena. From the very first investigations of the LSB, some researchers considered the analysis of the bridging phenomena at a micromechanical level by modeling the bridging bundles as beams. The first approach by Spearing & Evans [7], models a representative bridging bundle, as a cantilever beam attached to the intact arms of DCB specimen, under mode I loading conditions. In this model the energetic contribution of bending is superimposed, to decohesion of the bundle, and for the adopted simplifications, it provides a single bundle bridging-law in a closed form solution that can be used as a simplistic estimate. Furthermore, another model exists in the literature, tailored for fiber-reinforced composites, with ceramic matrices, proposed by Kaute et al., 1993 [60]. This model is also applicable to mode I fracture conditions, incorporating for the fibers' pull-out and peeling-off, which play a significant role especially in these types of composites. More recently, Sørensen et al., 2008 [61] extended the existing models for FRPs [7,9], to incorporate the effect of mode-mixity in LSB fiber ligament decohesion and failure. All these models provide some closed form solutions, after some simplifications, yet they fail to predict complicated phenomena, like the effect of specimen stiffness in the maximum ERR.

New advances in the numerical virtual testing techniques [62,63,64,65], using multiscale modeling methods, are proven very robust in simulating the failure mechanisms of composite materials. All the afore-cited works include FE modeling of fracture phenomena, using the embedded cell approach which comprises detailed modeling of fibers and interfaces involved in failure, while for the far field, homogenized properties are used, to reduce the processing cost in the solver. Recently, a multiscale model based on the embedded cell technique [66], predicts the experimental load-displacement response as well as the ERR and captures the thickness effect on crack advancement in the presence of LSB. The experimental part of this approach [66] is part of this thesis and is reported in §5 and [55]. In this method fiber-bundles are modeled based on microscopic evidence from the fractured specimens. This technique is also implemented on an experimented carbon/thermoplastic composite [67], being part of this thesis and this time is also used to extract directly the traction-separation relations. Further details for the numerical micromechanical model can be found in the methodology section (§3.6.3) and the corresponding results (§4.3).

2.5 Through the thickness reinforcement techniques

Laminated fiber reinforced composites can be created using three different techniques:

(i) By laminating, on the desired direction, UD pre-impregnated laminas, usually with a polymer matrix.

(ii) By infusing, wetting etc. with resin, (a) pre-laminated UD laminas in the desired directions, held together with polymer stitches, forming the so-called, non-crimp fabrics, (b) pre-laminated woven fabric plies.

The last techniques and in general any type of dry fiber preform, allows the introduction of through the thickness reinforcements (TTR) by means of stitches with high strength fibers, or fibrous tufts. On the other hand, the first technique allows reinforcement with fibrous or metallic pins (z-pins). These TTR techniques increase the resistance in delamination of these composites, 1 to 2 orders of magnitude, compared with their initial fracture toughness. This is accomplished by the closing traction imposed by TTR components that are bridging the delaminating plies. This toughening effect of the TTR is very essential in preventing and stopping delamination that can initiate from existing defects, fatigue or impact [68]. Nevertheless, TTR introduces one more complicated stage at the already elaborate and expensive manufacturing procedure of composite structures. As a result, full characterization of the effects of the TTR technique is of high interest in order to fully exploit their advantages.

Fibrous stitching is a relatively simple TTR technique, employed using tools from the textile industry and it is proven to increase delamination resistance [69]. Nevertheless, stitching is inducing some preloading to the laminas, which is difficult to control and for this reason is not vastly used, for the moment.

The most popular and very well characterized TTR technique is z-pinning, mainly due to the good repeatability of the procedure. The z-pins increase the fracture resistance in delamination of the host material, by the initial locking of the z-pins and after the first failure, by the friction opposed to the pulling-out of the pins. Characterization of the force-separation relation of z-pins' pulling-out mechanism, demonstrates that the accumulated damage is a function of the quality of the cohesive interface between the matrix and the pin. As a result, the diameter of the pins may be more important than their material, since pins of metallic or carbon fiber origin, may have the same response [70,71].

Some analytical approaches exist to model the response of the z-pins based on the shear lag theory [70], while combinations of numerical micromechanical and analytical methods have also been proposed [72,73]. The cohesive response of the z-pins is usually obtained experimentally by tensile tests where a single pin is pulled out of the composite substrate. Modeling of the complete delamination phenomena requires knowledge of the interlaminar failure response of the adjacent layers and the z-pinned interface. Typically, DCB specimen configuration is used to experimentally characterize the fracture response and the existing modeling techniques [74,73] comprise a cohesive element zone for the non-pinned interface while the pins are modeled as embedded cells with the characterized shear model.

Recent developments in the implementation of tufting in fabric preforms, have promoted the industrial application of this TTR technique. The toughening effect of tufting can be similar or superior to the one of z-pinning or, stitching [75,76], due to the mechanical locking of the tufts and their high strength, fibrous nature. All TTR toughening mechanisms can be modeled with the methods described for the z-pinning case, while the traction-separation relations of the tufts are quite different from the z-pins, since mechanical locking exists and the tuft may be partially pulled out before total rupture. An example of experimental characterization and modeling of a tufted composite is presented in [76]. However, the effect of tuft pattern and geometry is still not well characterized. In addition the single tuft pull-out experiment may not provide representative force-separation relations, due to the complexity of the experiment and the potential interaction of the tufts. Moreover, in the modeling part of the cited works, it is considered that the non-TTR interfaces fail in a perfect brittle way without any contribution of LSB phenomena that usually appear, especially in mode I fracture.

Part of this thesis, is the characterization of a tufted woven GFRP composite in mode I delamination, using the DCB configuration, employing the traction-separation relation of the un-tufted equivalent and the force-separation relations of tufts from uniaxial tuft pulling tests. The final objective is to propose a numerical, modeling method able to simulate the delamination response of the tufted GFRP.

2.6 Fracture testing configurations

The very common testing tool for mode I characterization of many materials is the DCB specimen configuration. A DCB specimen can be loaded under either end opening forces (EOF) (Fig. 2.7(a)), or pure moments (PM) (Fig. 2.7(b)). Moreover, mode II characterization can be conducted using a DCB based configuration known as the end-loaded-split (ELS) test [77], as well as mixed mode experiments, using DCBs under uneven bending moments (UBM) [27,78,79,80].

Regarding the mode I experiments, the simple DCB configuration (Fig. 2.7(a)) leads to relative simple experiments with reliable results for the fracture characterization of a material, without the necessity of complex specimens and test-rigs, and for this reason it is standardized [49,51]. Nevertheless, when it comes to characterization of fracture with LSB phenomena, or other types of large process-zone cohesive behaviors, the simple DCB configuration under EOF, is supposed to provide questionable results according to Suo & Bao, 1992 [8]. This argument is based on the variant stress distribution on the DCB arms for the EOF case, as the maximum stress, being proportional to the applied moment, increases linearly along the arms (Fig. 2.7(a)). As a result the crack propagation may not be self-similar, since the region that the tractions appear has a variant stress-field, leading to lack of steady-state in the development of traction-separation relation. Contrary to that, the pure moment configuration provides an invariant stress field all along the crack length, allowing for self-similar propagation and steady-state achievement. Nonetheless, the argument of Suo & Bao [8], is proven weak among the numerus studies that involve DCB under EOF and are reaching a self-similar crack propagation, steady-state and fully developed LSB [6,7,10,11,18,47] etc.

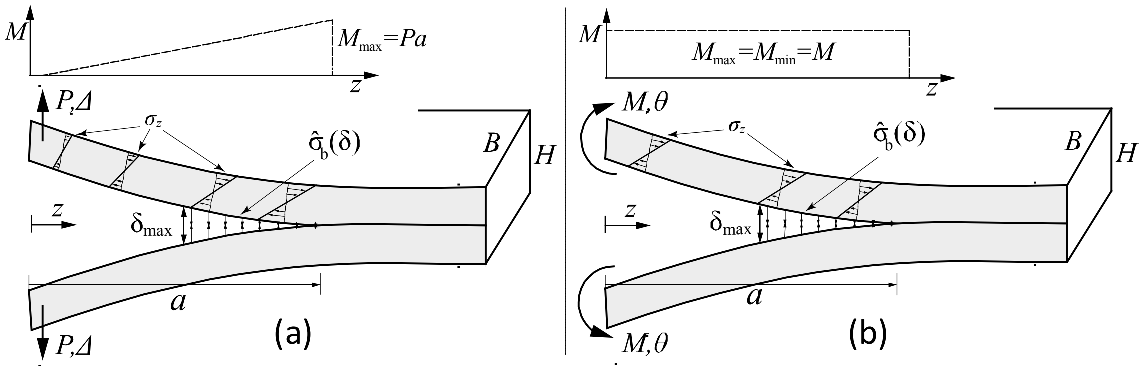

Fig. 2.7: (a) DCB under end opening forces.
(b) DCB under pure-moment.

This mentioned argument described in [8], should be reformulated, as a question on whether the traction-separation relation acquired from the EOF, is applicable to other mode I loading conditions, and if the identified cohesive law, is the same with the PM configuration, where the details of the bridging law are supposed to be 'independent of the ERR measurements' [9,27,81]. According to the already cited works [8,9], the PM configuration, and only this, should result to a traction-separation relation valid for all loading cases of the same fracture mode, while [81] considers that each loading case should demonstrate a different cohesive profile. Part of this thesis's scope is to answer this question.

The PM configuration, although it stands as a very convenient ERR and traction-separation characterization tool in terms of calculations, in practice, requires very elaborate test-rigs and specimens fixtures that are challenging the efficiency and the applicability of such a testing protocol. Moreover, pure moment cannot be applied directly in reality, but it can only be introduced by a pair of forces, or some distributed tractions resulting to an effective moment. The first reported experimental setup able to apply a pair of pure moments on a DCB specimen, was implemented on studying the mode I fracture response of a ceramic material, by Freiman et al., 1973 [82] as depicted in Fig. 2.8(a). This experimental setup is relatively simple to construct and test, while the specimen fixture induces stress concentrators that can lead to local failure, which may affect the pure moment stress distribution and the calculations of energy dissipation. However, for the tested ceramic material, it stands as a very robust test-rig for its simplicity.

The idea of this configuration is extended in a more recent study conducted by Sørensen et al., 1996 [78], once more initially tested in a ceramic material, with the load being applied by wires and pulleys (Fig. 2.8(b)). The latter configuration is also implemented in CFRP composites to investigate the LSB phenomena [9,15] and the toughness of adhesive joints [31]. The main advantage of this testing setup is the presence of the wires and pulleys, that allow for an easy adaptation to uneven bending moment (UBM)-DCB configuration as implemented in [27]. Nevertheless, the problems of the stress concentrators at the specimen gripping positions as described for the former test-rig are more problematic for a polymer based composite, while the compliance and the slipping of the wires may lead to erroneous measurements.

A more promising design to apply symmetric PMs in DCB is reported in [83] and is depicted in Fig. 2.8(c). This test-rig can be mounted in any conventional axial testing machine, while moment is transferred to the specimen by a pair of forces, being an improvement compared to the two aforementioned setups. Nonetheless, specimens' gripping is facilitated by its size and nature (woven GFRP) which allows for this simplistic fixture. Moreover, the whole implementation, as depicted in photos included in [83], reveals the poor design and manufacturing of this test-rig from a machine element design aspect. The calculated ERR and the applied load, are so high for the tested specimens that allow for many simplifications on the loading concept and make the induced friction negligible.

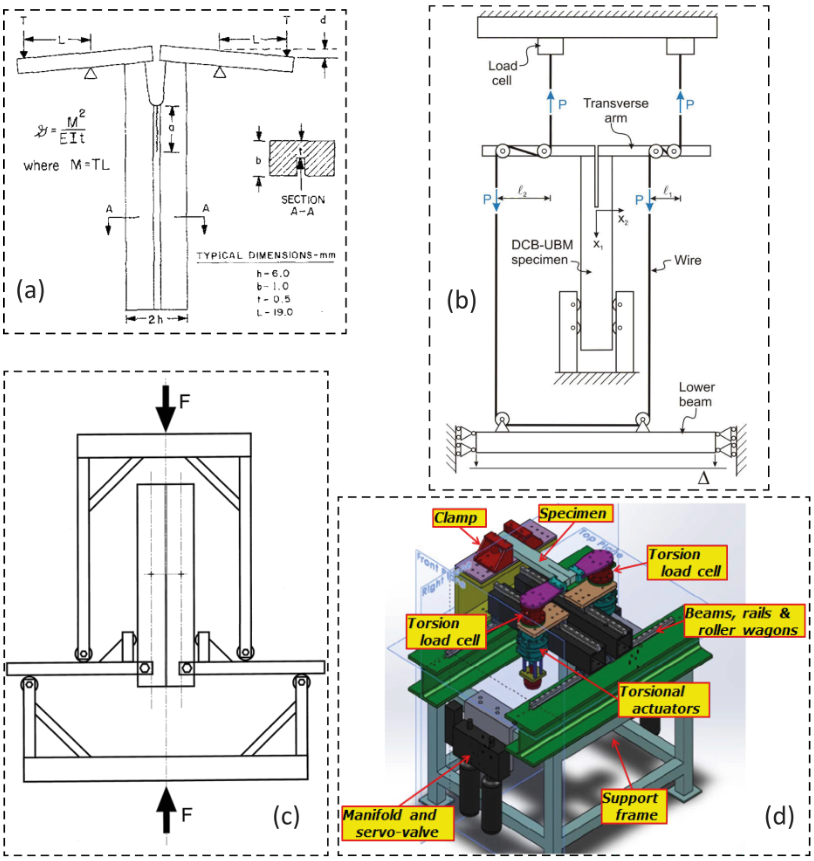
T
L
T
d
L
$\mathcal{G} = \frac{M^2}{EIt}$
where M = TL
a
b
t
SECTION A–A
A
A
TYPICAL DIMENSIONS-mm
h - 6.0
b - 1.0
t - 0.5
L - 19.0
2h
(a)
Load cell
P
Transverse arm
P
P
ℓ_2
P
ℓ_1
x_2
x_1
DCB-UBM specimen
Wire
(b)
Lower beam
Δ
F
F
(c)
Clamp
Specimen
Torsion load cell
Torsion load cell
Beams, rails & roller wagons
Torsional actuators
Manifold and servo-valve
Support frame
(d)

Fig. 2.8: Pure moment loading configurations present in the literature:

(a) Freiman et al., 1973 [82].

(b) Latest adaptation of Sørensen et al., 1996 [78] at Sørensen & Jacobsen, 2009 [27].

(c) Lindhagen & Berglund, 2000 [83].

(d) Berggreen & Anyfantis, 2014 & Saseendran et al., 2015 [79] & [80].

As it is already mentioned, the pure moment cannot be implemented directly; in practice a pair of forces or, equivalent tractions have to be applied with a resulting moment. However, the measurement of these tractions with precision might be problematic. To overcome this issues, recently, a new PM configuration is proposed in [79] and [80], where the moments are transferred as torsion by hydraulic actuators, and the applied torsion is measured with torsion load-cells Fig. 2.8(d). This setup is tested on interface characterization of composite sandwich beams. The presence of two independent actuators and moment measuring points, are the main improvements of this test-rig. On the other hand, apart from being extremely elaborate to build, there is a potential of mechanical locking and induction of high friction, with the slightest misalignment of the four linear bearings of the setup. The authors of [80] report the need of extra reinforcement on the composite sandwich beams to keep the opening displacements and rotations in low levels.

Fracture cases with long traction zones on the wake of the crack tip may be present in all fracture modes. As a result the same arguments, and issues that have been already analyzed for the mode I fracture, can be projected in pure mode II and mix-mode fracture, with the question on traction-separation relations' universality, regardless the details of the loading conditions, still to remain. In any case, the pure moment configurations which are assumed to provide J-integral measurements 'independent of the details of the traction-separation relations' [8,9,27] are shown in Fig. 2.9. Nevertheless this assumption has never been proven experimentally with independent comparative measurements. All the pure moment configurations assumed to have this characteristic, of all fracture modes, are shown in Fig. 2.9.

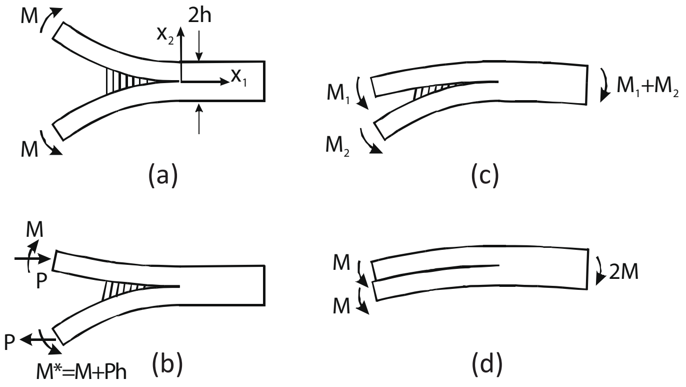

Fig. 2.9: Examples of specimen configurations J-integral measurements 'independent of the details of the traction-separation relation' [27]:
(a) DCB specimen under pure moments (Mode I).
(b) DCB specimen under both axial forces and moments (Mixed Mode I &II).
(c) DCB specimen under uneven moments (DCB-UBM) (Mixed Mode I &II).
(d)DCB specimen loaded with pure, equal moments (pure Mode II).

Chapter 3

Methods

3.1 Fracture testing and specimens

For the greatest part of this work the experimental procedure used follows the ASTM standards [49] for interlaminar fracture characterization of a simple DCB Mode I test rig. The experiments are performed at room temperature with a constant displacement rate with the displacement being monitored by the machines' integrated LVDT, while the loads are recorded using the standard load-cells of the testing machines. For the remaining part of the study, a novel test-rig is built capable to apply pure bending moment conditions on DCB specimens. For this part of the study an additional load-cell, and an in-house calibrated rotary encoder, are employed to monitor the loads and the rotations during the experiments. Further details are included in §6.3.

Several DCB specimens are fabricated and, in most of the cases, loading of the specimens is achieved with two steel loading blocks, glued symmetrically on the pre-cracked edge.

On selected specimens, optical fibers with 10 multiplexed FBG sensors are glued on the upper surface of the specimen, to monitor the strains during specimens' fracture. A schematic of a typical UD DCB created specimen with an intralaminar precrack is illustrated in Fig. 3.1. Positioning of the fiber on the surface of the specimen, instead of embedding it at the curing process, is chosen to avoid excessive handling of the specimen during preparation and the pre-cracking procedure. Moreover, this positioning provides uniform strain measurement, avoiding interaction with the LSB plane, which is described by the noticeably big bundle size of the intralaminar fracture.

It is well known that the geometry of the crack starter is important in the experimental evaluation of the initial fracture toughness. Regarding the specimens for intralaminar fracture (§4, §5 and §6), on which is very difficult to insert a release film during fabrication, a 60 mm intralaminar precrack, a_0 (see Fig. 3.1), is introduced in each beam by the use of diamond wire saw, with a diameter of 130 μm, to create symmetric DCB specimens. Such a long precrack, with a tip radius, $\rho = 65$ μm and $\rho / a_0 \ll 1$, can be considered as a natural crack according Tada et al., 2000 [84]. Similar techniques have been used in the literature using either the diamond wire or diamond coated disks [9,85] forming a pre-crack with at least the double crack tip diameter. In some cases, an initial fatigue precracking can be used, risking though initiating fiber bridging.

The suitability of the diamond wire precrack as an equivalent of a natural crack, can be also assessed using the process-zone length calculation formula, proposed by Hillerborg et al., 1976 [86], given as $\ell_c = E_x G_{I,i} / \sigma_c^2$, which is providing a critical length of ~1.4mm for a 40MPa of tensile strength in the transverse direction and for a typical initial fracture toughness $G_{I,i} \simeq$ 300J/m^2. As a result the expected process-zone at initiation is 10 times longer than the diameter of the precrack. In any case, for both the tested carbon/epoxy and carbon/thermoplastic composites, the interlaminar initiation fracture toughness (using an insert film) compares very well with the acquired intralaminar value from specimens with the crack starter introduced using the diamond wire. At this point it is worth mentioning that the intralaminar fracture initiated using the diamond wire, is free from the pop-in effect, caused by the resin pocket created ahead of the film inserts at the delamination experiments which is the main reason why in [49] is instructed to use very small thicknesses on the film inserts, as reported in [87].

Regarding the investigation on delamination resistance of the studied woven GFRP composite, an ETFE film, 13μm thick is introduced during the fabrication procedure to form a symmetric precrack, as instructed by the ASTM standards [49]. The introduced precrack has a length of 65±2 mm.

One side of each specimen, normal to the plane defined by the precrack, is painted with high quality, brittle, white spray paint and a fine printed paper ruler with 1 mm step, is glued on the lower half. This preparation is necessary, to provide a clear image of the crack tip position during the experiment in order to construct the R-curves and create representative numerical models with the correct crack length. Representative photos of the fractured specimens are illustrated in §4.3.1, §5.3.1 and §7.3 of this thesis. The crack propagation is monitored by means of a high resolution (1392 × 1024), monochrome CCD camera that constantly records the crack tip position at 1 Hz and the visual crack length recognition accuracy is at least 0.25 mm as instructed by [49].

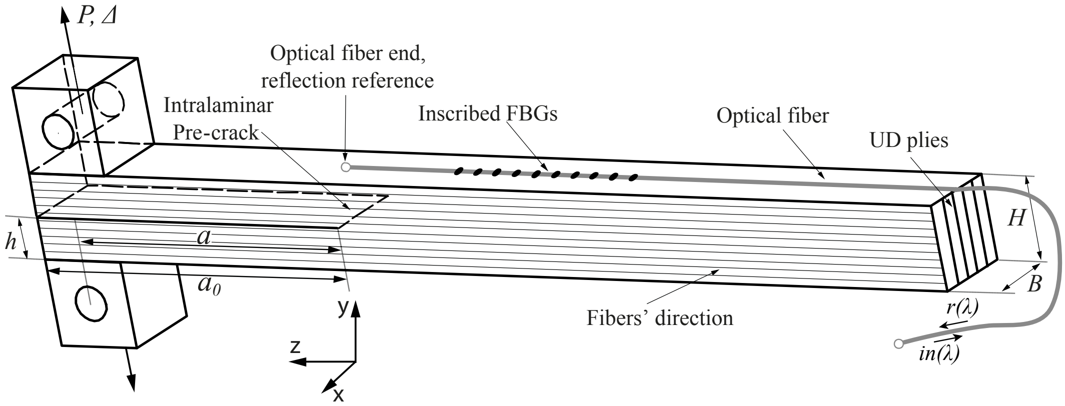

Fig. 3.1: Schematic of a typical intralaminar DCB specimen with the glued optical fiber on the upper surface (not to scale).

3.2 ERR calculation

The initial failure and the accompanied damage of a structural material are described by crack initiation and crack propagation. The characterization of these phenomena is made by means of the ERR measured in J/m^2. In the literature the symbol G is conventionally used when referring to LEFM conditions, where ERR has a linear relationship with the square of the critical SIF for each mode case i.e. $K_{IC}^2, K_{IIC}^2, K_{IIIC}^2 \propto G_{IC}, G_{IIC}, G_{IIIC}$ [19,88]. On the other hand, for the general case (with any non-linearities, i.e. large displacements, plasticity etc.) the symbol J is used, being introduced by the definition of the J-integral by Rice in 1968 [30]. These symbol-conventions will be respected throughout this document. The experiments carried out in this study demonstrate that LSB accompanies intralaminar fracture. Thus, non-linear geometrical effects may be important, while the material behavior is assumed linearly elastic as explained later. For this reason the ERR calculations are considered and compared to evaluate the extent on non-linearities.

The ERR has been defined by Irwin since 1956 [89], as the negative partial derivative of the potential energy of the system, Π, over the crack length increment, thus:

$$G \, or \, J = -\frac{1}{B}\frac{\partial \Pi}{\partial a} \qquad (3.1)$$

where $\Pi = U - W$ and U being the strain energy and W the work done by the external forces. Since G or J is obtained from the derivative of the potential is also called crack extension force, or most commonly crack driving force [19]. As a result, if the potential energy change over crack area, of a system, reaches the critical ERR for a given material, the crack advances. The aforementioned definition is based on a 2D analysis with plain strain state on the tip, and for this reason the derivative of the potential is simply divided by the width B. Nevertheless, the generalization of this definition (3.1) can be valid for simple 3D cases as well.

3.2.1 Linear elastic fracture mechanics

Following the aforementioned definitions, and considering the generic linear elastic case ($\Pi = -U = -\frac{1}{2}P\Delta$), the simplest way to calculate experimentally ERR is by the derivative of the potential energy, using finite differences. This method is also called the area method [19], and in order to obtain some accuracy, the crack increments have to be particularly smooth.

Alternatively, in order to increase the accuracy, methods based on the compliance of the system are implemented. Namely, the total mode I ERR, G_{total}, for a composite material with bridging tractions, can be calculated by the following expression [19]:

$$G_{total} = G_{I,i} + G_{i,b} = \frac{P^2}{2B}\frac{\partial C}{\partial a}, \; C = \Delta / P \qquad (3.2)$$

where P, is the recorded reaction load, Δ is the applied opening displacement, B is the specimen's width, C is the compliance and a is the crack length measuring from the loading point (see Fig. 3.1). Parameters $G_{I,i}$, $G_{i,b}$ refer to the ERR values at initiation and the contribution of bridging to fracture resistance.

The critical ERR at initiation $G_{I,i}$ (linear case) for the mode I intralaminar DCB specimen can be accurately calculated using the formulation proposed by Hashemi et al. [90] applied in delamination problems, produced by calculating the compliance of a DCB loaded with EOF, using the orthotropic nature of a composite material included in correction factor x and a correction factor f for end block effects. The analytical expression, for the plain strain case, is as follows:

$$G_{I,i} = \frac{12 f\, P^2 (a+xh)^2}{B^2 h^3 E_z \big/ (1-v_{xz}v_{zx})} \tag{3.3}$$

where E_z stands for the modulus in the direction of the fibers and h is the thickness of each DCB arm (see Fig. 3.1). The calculated compliance of the pre-cracked intact specimens using this approach is in perfect agreement with the experimental data. At this point it should be noted that, $\varepsilon_{zz} = \frac{1-v_{zx}v_{xz}}{E_z}\sigma_{zz}$ for the plain orthotropic case and due to the transverse isotropy of the unidirectional materials under investigation $v_{zx} = v_{zy}$. Moreover, for highly orthotropic materials, such as the tested UD specimens, the difference between the plain stress and plain strain model is ~1 %, since $(1-v_{xz}v_{zx}) = 0.99$.

When progressive resistance to crack growth is present (i.e. R-curve behavior), use of Eq. (3.2), requires experimental values of C and a to obtain the compliance vs. crack length function. Conventionally [49], two empirical approaches are implemented to express the compliance vs. crack length. The first is referred to as the Compliance Calibration (CC) method, [49] where the compliance is fitted in a power law as $C = \Re a^{\eta}$, where $\Re$ and η are the fitting parameters, also commonly known as Berry's law [91]. The second method is referred to as the Modified Compliance Calibration (MCC) [49], with the compliance being fitted by $C = (a/H\mathbf{A}_1 + \mathbf{A}_2)^3$, where $\mathbf{A}_1, \mathbf{A}_2$ are fitting parameters and H is the total specimen's thickness. This second method proposed in [92], based on the work of Williams' group ([90] and references therein, as described in Eq. (3.3)), is recommended by the ASTM standards [49] to increase the accuracy of the ERR calculations [87].

Typical experimental data and the fitting curves from the CC and MCC methods from conventional DCB tests, of the thermoset composite system are shown in Fig. 3.2. The data in Fig. 3.2(a) demonstrate that the CC method may provide a satisfactory fitting for the calculation of fracture toughness at initiation $G_{I,i}$. However, it fails to describe the rapid decrease of specimen compliance due to LSB in intralaminar fracture. Although, the MCC method describes better the gradient of compliance due to LSB (Fig. 3.2(a)), is not very precise in the transition zone and the steady state propagation. The option of higher degree polynomial fitting has also been investigated, but the fitting becomes specimen-sensitive and the accuracy on the initiation value is lost, therefore this approach is not beneficial.

To obtain a better fit of the ERR at steady propagation ($G_{total-SS}$) and compare it with the value obtained from the identified tractions, a segmented CC method (Double Compliance Calibration or DCC) can be used to evaluate the ERR on the two important regions on an R-Curve (i.e. initiation and steady state). The first segment consists of compliance and crack length data, from initiation to the start of the steady state propagation, and the second is formed by data only from the steady state propagation region. This calibration approach is also shown in Fig. 3.2(a). For comparison, the error between the fitted compliance and experimental values is evaluated by its residual norm as $erf({}_{x}CC)=\left\|\left(C_{fitted}-C_{\exp}\right)/C_{\exp}\right\|$. These calculations show that the DCC approach has an ~65% improvement on the error function and provides more accurate results for $G_{I,i}$ and $G_{I,b}$. However, the resulting R-curves become likewise segmented, as seen in Fig. 3.2(b). In this work, the MCC method is used to construct benchmark experimental R-curves. The DCC is also used to compare the ERR values obtained from the identified traction-separation relation and the experimental values at initiation and steady state (§5.3.5). In general, the characterization of fracture response is done in the steady state of crack propagation, and as a result, fitting the data from the steady state only, can significantly improve the accuracy of the calculated ERR. Therefore, for completeness, R-curves of the mode I intralaminar DCB experiment, using the MCC for both the full range of the experiments and only for the steady state (SS-MCC), are also considered in the analysis of the experimental data (§4.3.1).

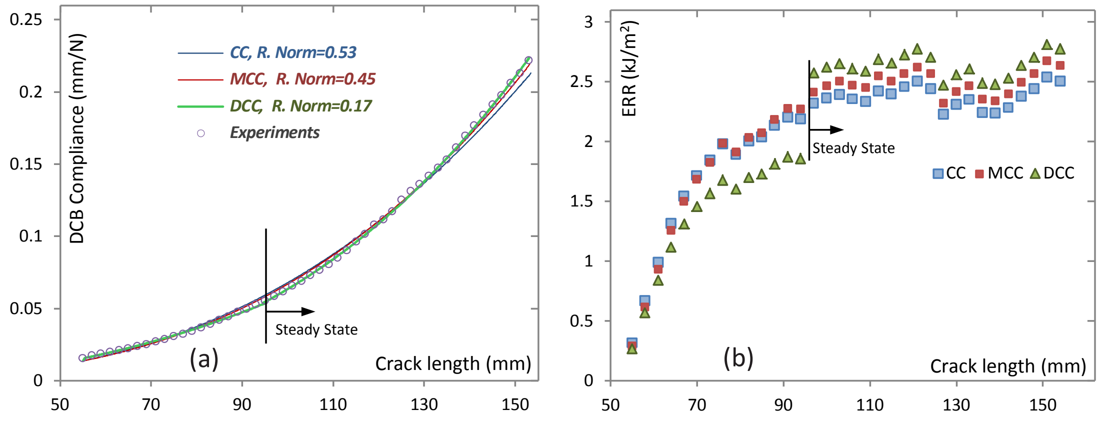

Fig. 3.2: (a) Compliance vs. crack length for different calibration methods, $H = 10$ mm. (b) Resulting R-curves for different compliance calibration methods, $H = 10$ mm. These data are from the thermoset composite system.

3.2.2 General fracture mechanics' cases

Rice [30] defined the J-integral, using the generic formulation for the strain energy and the external body tractions to calculate the derivative of the potential energy over the crack length increment (i.e. ERR). The result of that work is the following path independent contour integral:

$$J\big|_{\Gamma} = \frac{1}{B}\oint_{\Gamma}\left(w dx_2 - T_i \frac{\partial u_i}{\partial x_1} ds \right) \qquad (3.4)$$

Where, w is the strain energy density, T_i are the body tractions and Γ is an open contour around the crack (see Fig. 3.3 and Appendix I).

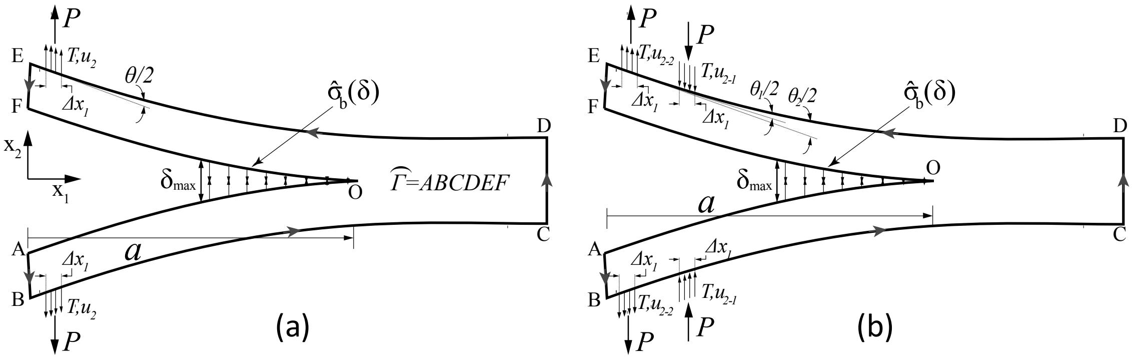
P
E
T, u_2
$\theta/2$
F
Δx_1
$\hat{\sigma}_b(\delta)$
D
x_2
x_1
δ_{max}
O
$\widehat{\Gamma}=ABCDEF$
A
Δx_1
a
C
B
T, u_2
P
(a)
P
P
E
$T, u_{2\text{-}2}$
$T, u_{2\text{-}1}$
$\theta_1/2$
$\theta_2/2$
$\hat{\sigma}_b(\delta)$
F
Δx_1
Δx_1
D
O
δ_{max}
a
C
A
Δx_1
Δx_1
B
$T, u_{2\text{-}1}$
$T, u_{2\text{-}2}$
P
P
(b)

Fig. 3.3: (a) J-integral definitions for DCB under end opening forces.
(b) J-integral definitions for DCB under a pair of forces, i.e. a pure-moment configuration.

For a DCB specimen, subjected to EOF (Fig. 3.3(a)), the ERR, J_{total}, at any crack length, can be calculated using outmost contour, where the strain energy vanishes and only the body tractions contribute as:

$$J_{total} = \frac{1}{B}\left(-\int_{0}^{\Delta x_1} T \frac{\partial u_2}{\partial x_1} dx + \int_{\Delta x_1}^{0} T \frac{\partial u_2}{\partial x_1} dx \right) \qquad (3.5)$$

For the given tractions $T = {P}/{dx}$ and identifying the total relative rotation, θ, measured at the two loading points as: ${\theta}/{2} = {du_2}/{dx}$, the ERR can be calculated as follows [93,84]:

$$J_{total}^{(\theta)} = \frac{P\theta}{B} \tag{3.6}$$

This formula is the result of the J-integral evaluation along the outmost contributing contour thus, is independent of the damage zone and accounts for any geometrical and/or material non-linearities. Therefore, Eq. (3.6) provides a realistic measure of ERR and is used to construct the R-curve of the DCB experiment which is compared with G_{total} from Eq. (3.2) and the compliance calibration methods. This is also one way to quantify the extent of non-linearities of the DCB experiment.

3.2.3 DCB under pure moment

As it has already been mentioned, apart from the conventional end opening forces loaded DCB configuration, DCB loaded with pure bending moments is considered (see Fig. 2.7(b)). For this case, the ERR can be calculated with simple analytical solutions in both the linear elastic and the general case (G & J), and is independent of the crack length. For the linear elastic case, a closed form analytical solution can be expressed as follows for any isotropic material:

$$\left.\begin{aligned} & W = M\theta \ \& \ U = \frac{M\theta}{2} \underset{for\,each\,beam}{\overset{beam\ theory}{\Rightarrow}} \frac{\theta}{2} = \frac{Ma}{EI} \\ & \Rightarrow C_{tot} = \frac{\theta}{M} = \frac{2a}{EI} \Rightarrow \frac{\partial C}{\partial \mathrm{a}} = \frac{2}{EI} \end{aligned}\right\} \Rightarrow G = \frac{1}{B}\frac{\partial U}{\partial a}\bigg|_M = \frac{M}{2B}\frac{\partial \theta}{\partial a}\bigg|_M = \frac{M^2}{2B}\frac{\partial C}{\partial a} \Rightarrow \boxed{G = \frac{M^2}{BEI}}$$

This formulation can be adapted for a plain strain case of an orthotropic material (z, parallel to the neutral axis) as:

$$G_{PM} = 12(1-\nu_{zx}\nu_{xz})\frac{M^2}{B^2h^3E_z} \tag{3.7a}$$

Remarkably, for the DCB configuration under pure moments the LEFM solution gives the same result with the general case, with certain simplifications as described subsequently. This can be proven with the following analysis [30,88]: Considering the J-integral at the most exterior contour of a DCB like the one illustrated in Fig. 2.7 (b) (respecting the definitions of Fig. 3.3) and assuming that due to pure bending the tractions are simply equal to the maximum bending stresses $T_1 = \sigma_{11}$, and for $\varepsilon_{11} = \partial u_1 / \partial x_1$ then Eq. (3.4) results to:

$$J\big|_{\Gamma_{ext}} = \oint_{\Gamma_{ext}} \left(w dx_2 - T_1 \frac{\partial u_1}{\partial x_1} ds \right) = \int_{-H/2}^{H/2} \sigma_{11}\varepsilon_{11} dx_2 = 2\int_{0}^{H/2} \sigma_{11}\varepsilon_{11} dx_2,\ for\, w = \sigma_{11}\varepsilon_{11}/2 .$$

If the horizontal axis is shifted to the neutral axis of the upper arm-beam so that $x_2' = x_2 - H/4$, then $J = 2\int_{-H/4}^{H/4} \sigma_{11}\varepsilon_{11} dx_2'$. Assuming now pure bending conditions along the surface contour, and relatively small deformations (therefore $(\partial u_1/\partial x_1)^2 \ll 1$), then $\sigma_{11} = Mx_2'/I'$ and $w = \left(Mx_2'\right)^2/2EI'^2$ are obtained, providing $J = \dfrac{M^2}{EI}$. Note that for the aforementioned steps and only, J, σ_{11} and I are defined for unit thickness.

As a result for the pure moment DCB configuration, the ERR calculation (LEFM and general case) is given by the same formula (also orthotropic material, plain strain i.e. ε_{11} or, $\varepsilon_{zz} = \dfrac{1-v_{zx}v_{xz}}{E_z}\sigma_{zz}$):

$$J_{PM} = 12(1 - v_{zx}v_{xz})\frac{M^2}{B^2h^3E_z} = G_{PM} \qquad (3.7b)$$

At this point it is important to be noted that in the literature [8,9,83] for simplicity the product $v_{zx}v_{xz}$ is considered equal to $v_{zx}{}^2$. This assumption of isotropy, can lead to errors even greater than 10%, provided that the tested material is highly orthotropic like a UD FRP. For the latter case, the plane stress and plain strain solution provides practically the same result, as it noted on the comments after Eq.(3.3). This assertion, is also verified by the created FE models.

The previous formulation for the general case has the advantage of being simple, allowing for ERR calculations and establishment of R-curves, by measuring the applied moment. Nevertheless, still some first order approximations are made mainly on the relation between stresses and strains, provided that highly orthotropic materials might be investigated and surface tractions like cohesive forces or, LSB tractions may be present. Alternatively, and after comprehending that pure moment cannot be applied, but the load is always transferred by some surface tractions, a more precise way of calculating the J-integral may be proposed. In detail, for a pure moment applied by a pair of forces (Fig. 3.3(b)), the J-integral can be calculated in a similar way with the Eq. (3.5) & (3.6). As a result, the total ERR, J_{total} is calculated as:

$$\begin{gathered}J_{total}=\frac{1}{B}\left(-\int_{0}^{\Delta x_1}T\frac{\partial u_{2-2}}{\partial x_1}dx+\int_{0}^{\Delta x_1}T\frac{\partial u_{2-1}}{\partial x_1}dx-\int_{\Delta x_1}^{0}T\frac{\partial u_{2-1}}{\partial x_1}dx+\int_{\Delta x_1}^{0}T\frac{\partial u_{2-2}}{\partial x_1}dx\right)\Rightarrow\\ \Rightarrow\boxed{J_{total}^{(\theta_1,\theta_2)}=\frac{P(\theta_2-\theta_1)}{B}}\end{gathered}\tag{3.8}$$

Here the relative rotations at the loading points are defined as $\theta_1/2 = du_{2-1}/dx$ and $\theta_2/2 = du_{2-2}/dx$, while equal forces P, are assumed. This formulation provides very accurate estimation of the ERR at any point of crack advance and can be considered precise for all cases no matter the extent of process-zone and non-linearities during the experiment. All this due to the consideration of the outmost possible contour, where only external tractions are applied and the potential energy is simply equal to the energy provided to specimen like in the formulations of Eq. (3.6).

This concept has been applied successfully on the calculation of ERR for pure mode II in an older studies by Stigh [94] and more recent studies for mixed mode loading conditions by Sarrado et al. [33,34]. Apart from all advantages of using these methods (Eq. (3.6) & (3.8)) for evaluating the ERR, the main point of uncertainty is the measurement of the angles. In the literature devises such as rotary encoders [95] and inclinometers [34] are proposed, while in the current study rotary encoder and DIC techniques directly on the specimen, or on an assistive arm are used. Further details, are found in the corresponding sections (§4.2 & §6.3).

3.3 Microscopy and fractography

Prior to testing, transverse sections of the fabricated specimens, are examined under an optical microscope to evaluate the quality of the cured material and measure the void volume content of the composite using image-pixel processing by means of a Matlab® script. After testing, the specimens carbon-coated fracture surfaces, as well as transverse sections, are examined with a scanning electron microscope (SEM). For all the transverse sections standard metallographic preparation techniques are implemented before the microscopy sessions. For simplicity some transverse sections are studied using optical microscope, without significant loss in the image quality. The fractographic images are employed to assess the type of failure (cohesive or adhesive) at a microscopic level while the cross-sectional microscopy provides information for the fiber-bundle morphology. This information may also be used to create micromechanical models to simulate the LSB behavior in a multiscale simulation scheme. Finally, a digital-optical microscope (Keyence VHX-5000) is used to evaluate the roughness of the fractured surfaces.

3.4 Strain acquisition technique

The key for the characterization of the bridging tractions are the axial strain measurements during the fracture experiments. These measurements are carried out using 10 wavelength multiplexed FBG sensors, inscribed on a single-mode (smf-28), simple telecom optical fiber Fig. 3.4 (a). The diameter of fiber's cladding is 125 μm while the one of the core is 8.2 μm. The protective polyamide coating is removed around the region of the sensors, by applying sulfuric acid for a couple of minutes. This procedure is essential since the polyamide has poor adhesion properties & low modulus and as a consequence the measurements may be compromised due to its presence. The grating length of the sensors is 1mm, and the reflected Bragg wavelengths are equally spaced in a range between 1520 and 1565 nm. The maximum bandwidth per inscribed FBG (FWHM) is 1.5nm while they are characterized by a minimum 50% reflectivity and side lobe suspension reflection intensity (SLSR) of minimum 15dB.

The strain acquisition technique [96,97] is based on the FBG property to reflect only a characteristic Bragg wavelength, λ_{B0}, of the broadband source light, $in(\lambda)$, which is introduced in the optical fiber (details in Fig. 3.4(b)). The reflected (Bragg) wavelength, λ_B, depends on the systematic inscription of a varying periodic refraction index, n, into the core of a germanium-doped silica fiber. The inscription is done using a high intensity ultraviolet (UV) source (e.g. UV laser). For a uniform grating, the characteristic grating period, Λ_0, corresponds to the grating spacing. The relationship between the reflected wavelength, the grating period and the mean core index of refraction, n_{eff}, is: $\lambda_B = 2n_{eff}\Lambda_0$.

When an optical fiber is submitted to mechanical loading (Fig. 3.4(b)), the effective index and the grating period varies due to strain changes, and as a result the Bragg wavelength shifts to different wavelengths. For example, when each of the sensors is exposed to a uniform axial strain, the corresponding characteristic Bragg wavelength change, $\Delta\lambda_{B,i}$, for each sensor, i, is given: $\Delta\lambda_{B,i} = \lambda_{B,i} - \lambda_{B0,i}$ (Fig. 3.4(b)). If the strains are homogeneous and the axial strain is dominant ($\varepsilon_{x,i} = \varepsilon_{y,i} = -\nu_f \varepsilon_{z,i}$), the reflected signal peaks are sharp and narrow and are simply translated in space. In such case, the wavelength shifts ($\Delta\lambda_{B,i}$) can be correlated with the axial strains per sensor, $\varepsilon_{z,i}$, as [98]:

$$\frac{\Delta\lambda_{B,i}}{\lambda_{B0,i}} = (1-p_e)\varepsilon_{z,i} + (\alpha_f + \xi)\Delta T \text{, with } p_e = \frac{n_{eff}^2}{2}\left[p_{12} - v_f\left(p_{11} + p_{12}\right)\right] \qquad \text{(3.9a)}$$

In this equation α_f & v_f, are the thermal expansion coefficient and the Poisson's ration of the fiber, while ξ is a thermo-optic coefficient, while p_{ij}, are the Pockel's strain–optic constants. The coefficient p_e, is effective fiber strain-optic constant that can be obtained experimentally [97], as $p_e = 0.2148$.

If the strain field is non-homogeneous, wavelength peak spit may occur. For such cases, a method has been proposed in the literature [99] implemented for strains acquired along a long FBG sensor.

For the series of conducted experiments, where the dominant strains are axial (bending strains $\varepsilon_{z,i}$, see Fig. 3.4(b) & Fig. 3.5), it is observed that all FBG spectra are simply translated in space, while the temperature field is steady. For such case Eq.(3.9a) renders to:

$$\frac{\Delta\lambda_{B,i}}{\lambda_{B0,i}} = (1-p_e)\varepsilon_{z,i} \qquad \text{(3.9b)}$$

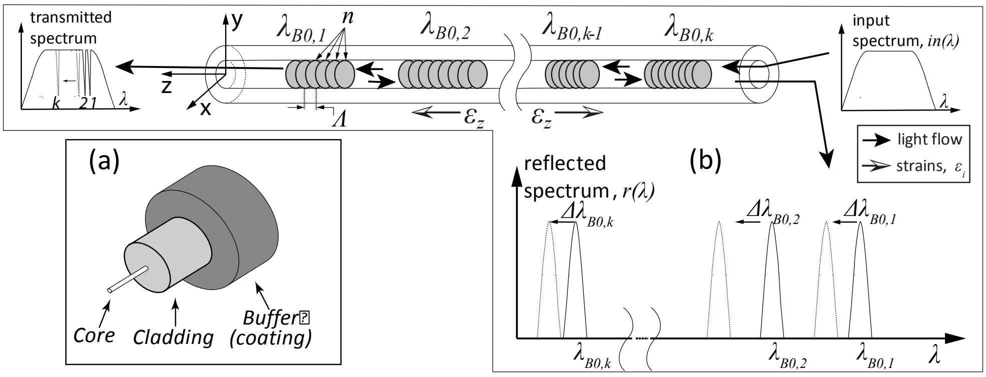
transmitted spectrum
k
2
1
λ
y
z
x
λB0,1
n
Λ
λB0,2
λB0,k-1
λB0,k
εz
εz
input spectrum, in(λ)
λ
light flow
strains, εi
(a)
Core
Cladding
Buffer (coating)
reflected spectrum, r(λ)
(b)
ΔλB0,k
ΔλB0,2
ΔλB0,1
λB0,k
λB0,2
λB0,1
λ

Fig. 3.4: (a) Perspective cross-section of a typical single mode optical fiber
(b) Typical FBG wavelength interrogator apparatus; schematic modified from [98].

The surface of the DCB specimens on which an optical fiber is bonded (see Fig. 3.5), is slightly roughened with a P1000 grinding paper and thoroughly cleaned with pure acetone. The prepared optical fiber is positioned on the center of the specimen's exterior upper surface and bonding is achieved by means of a liquid cyanoacrylate instant adhesive (Loctite® 401). A typical cracked specimen with the optical fiber is shown in Fig. 3.5 with a cross-section in detail. At this cross-section micrograph is visible that the interface between the optical fiber and the composite specimen is just a couple of microns thick due to the liquid nature of the adhesive. Hence, the measurements can be considered direct and accurate and the strain data acquired are assumed to correspond to the center of the optical fiber.

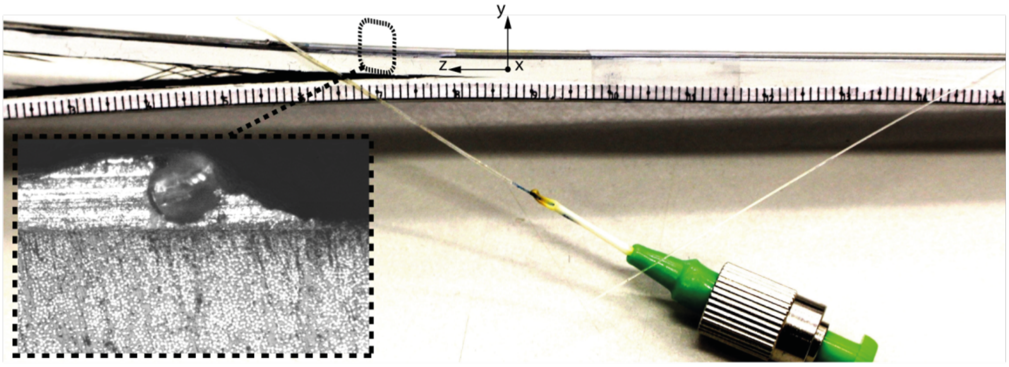

Fig. 3.5: Photo of a glued optical fiber on the upper surface of a specimen and microscopy of cross-section.

One of the main advantages of FBG sensors is multiplexing, which is accomplished, by inscribing many gratings with different Bragg wavelength on the same optical fiber [98,100]. Via sensor multiplexing, simultaneous measurements can be obtained from different positions of the same structure, with only one host optical fiber. For the current study, the wavelength changes are recorded by the use of a Micron Optics sm130 sensing interrogator, the working principle of which is presented in Fig. 3.6. The data acquisition frequency is 1000Hz, while the recording frequency is set to 50 Hz, providing sufficient resolution for the conducted quasi-static, monotonic experiments.

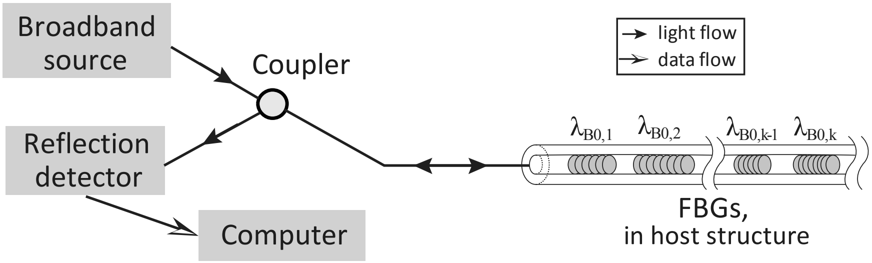

Fig. 3.6: Typical FBG wavelength interrogator apparatus; schematic modified from [98].

3.5 FBG position tracking

The exact position of the Bragg grating on the specimen, after the gluing procedure, is identified by the use of the Optical Low Coherence Reflectometry (OLCR) technique, the measuring principle of which is briefly presented in this thesis, while further details can be found in [98] & [101]. The details of a typical OLCR apparatus are depicted in Fig. 3.7. This technique is based on Michelson's scanning interferometer including a broadband light source and a light detector and can be used both for FBG signal acquisition [99] and FBG position tracking. For the current study OLCR is used only to track the position of the sensors.

For the FBG position tracking procedure, initially, the transmitted broadband light is split between the reference and the test arm. The two beams are reflected by, the moveable mirror and the FBGs, while, half of the reflected light is directed to the detector through the coupler. The two detected signals are delayed proportionally to the distance z and z'. When the signals are in phase, the reflected light intensity recorded by the detector is maximized. Thus, while the mirror translates, this event (the reflected light intensity maximization) will happen as many times as the number of the inscribed FGB sensors, plus once more, if the optical fiber is sharply sliced, to create a the free-end (point (C), in Fig. 3.7). The recorded relative spatial position, $z'(z)$, has to be corrected using the fiber's refractive group index $n_g \simeq 1.468$ to provide the actual position $z'_{real} = z' / n_g$. This is due to the fact that this special measurement is based on the speed of light; therefore, a correction for the phase velocity in the medium (optical fiber) has to be made. As a result, with the peaks recorded as a function of their relative distance, the actual position of the FBG sensors in the fiber can be tracked knowing the position of the optical fiber's free-end on the specimen.

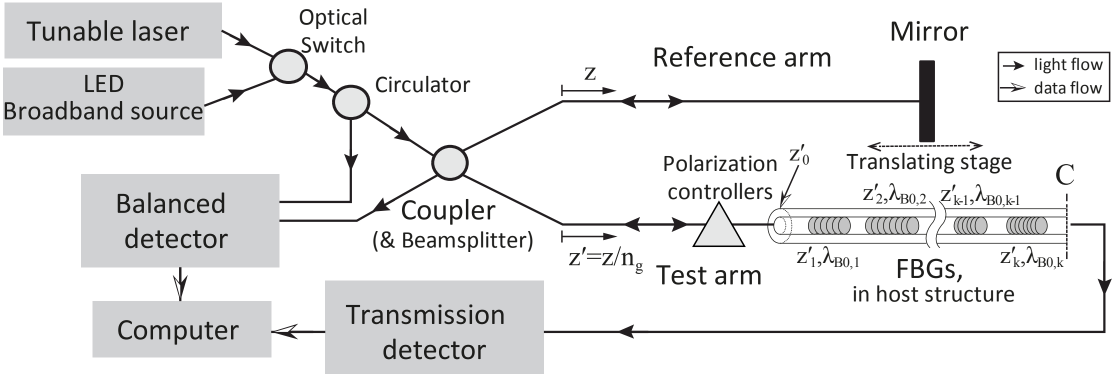
Tunable laser
LED Broadband source
Optical Switch
Circulator
Balanced detector
Coupler (& Beamsplitter)
Computer
Transmission detector
z
Reference arm
Mirror
light flow
data flow
Translating stage
Polarization controllers
z'_0
C
$z'_2, \lambda_{B0,2}$
$z'_{k-1}, \lambda_{B0,k-1}$
$z'=z/n_g$
Test arm
$z'_1, \lambda_{B0,1}$
FBGs, in host structure
$z'_k, \lambda_{B0,k}$

Fig. 3.7: Typical OLCR based apparatus measuring; schematic modified from [98].

A typical example of the recorded reflected light intensity over the corrected spacing is illustrated in Fig. 3.8. The scanning spatial accuracy of this measurement is 25 µm, while the actual measurements are done with recording resolution of 50 µm. Nevertheless, the overall precision of the procedure relies also on the accuracy on tracking the sliced free-end of the fiber, for which a high intensity laser source is used.

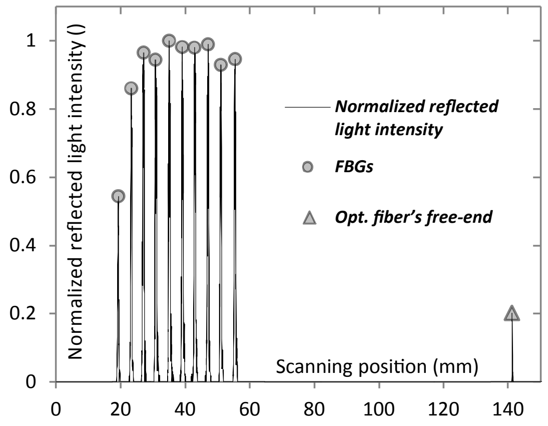

Fig. 3.8: Typical FBG position tracking, based on OLCR reflected light intensity measurements.

For these series of experiments the center to center distance of the integrated FBG sensors varies from 2.9 - 4.4 mm, resulting in a strain measurement region of ~36 mm, as it is attested using the aforementioned OLCR tracking method.

3.6 Numerical Methods

In this work, Finite Element (FE) plane-strain models (for the identification of bridging tractions and cohesive zone modeling) are built in Abaqus Standard v6.12 software using the actual specimen geometry. The boundary conditions follow the experimental conditions in all models (Fig. 3.9: (a), for half model or (b) for full). Due to minor asymmetry of the fractured specimens, in some cases, both arms of the specimen are modelled in the identification of the tractions (as explained later). For the cohesive zone analysis both arms need to be modeled while there, symmetric ones are sufficient.

The experimental observations of this study are also utilized to establish a three-dimensional micromechanical model based on the embedded cell approach. This is part of a parallel project carried out with Dr. Luis Canal. For a thorough description of the micromechanical model, the reader can consult the corresponding journal publications by Canal et al., 2016 [66] and Pappas et al., 2016 [67].

In all models the orthotropic material properties implemented for the composite arms, are reported in corresponding sections. While, stainless and mild steel isotropic material properties are implemented for the loading blocks, with elastic moduli, $E =$ 200 GPa and 210 GPa respectively, a Poisson's ratio $\nu =$0.3, and for the rollers (PM), simple aluminum with $E =$ 70 GPa & $\nu =$0.33, being all typical values for these metals.

Experimental observations reveal that LSB accompanies intralaminar fracture and requires relatively long crack lengths to reach a steady state. Thus, non-linear geometrical effects and/or material response may be present and should be investigated. Regarding of the tested material, the maximum measured experimental strain is about 4200 με (§4.3.2, §5.3.3 and §7.4.2). This value is well below the elastic limit of a typical carbon fiber/PPS composite at room temperature [102], below the 90° tensile elastic limit of the thermoset composite (Fig. 5.1), and the experimental tensile elastic limit for the woven GFRP composite, as measured with the in-plane tensile tests (§7.1.1). Moreover, for an epoxy based composite the failure is expected to be quasi-brittle, as seen in the SEM fractography (§5.3.1). On the other hand, for the thermoplastic matrix composite, the major failure mechanism is considered as be fiber-matrix interface debonding, being characteristic of this system as depicted in the low initial fracture toughness values contrary to other, thermoplastic matrices like PEEK [6]. Additionally, the plastic deformation of the matrix is considered negligible having a minor contribution on the failure behavior of the composite and this is supported by the absence of noticeable permanent deformation, of the fractured specimens. As a result, in all cases the failure is considered quasi-brittle and the material response is assumed linearly elastic.

To evaluate the extent of geometrical non-linearities, the unloading load-displacement curves are compared with a perfect linear response and a small extent of non-linearity is observed at relatively long crack lengths, corresponding to the steady phase of propagation. The difference in the area under the actual and linear responses does not exceed 3-4.5%. Furthermore, to fully investigate the effect of geometrical non-linearities in this DCB experiment, the optimization procedure is performed with both linear and non-linear (considering large displacements, Abaqus 'NLGEOM' [57]) numerical models. The obtained results (presented in §4.3.3) show that their difference does not exceed 4%, but for higher accuracy, the latter approach is used in all simulations for the characterization process.

3.6.1 Identification of bridging tractions

3.6.1.1 Ordinary approach

For the identification the of bridging tractions, an inverse technique is built, based on the strain profile produced by a 2D, finite element (FE), plain strain model of the DCB experiment, with the objective bridging tractions' profile, $\sigma_b(z)$, as the parametric input applied over the bridging zone as shown in Fig. 3.9 . The parametric bridging tractions' profile is represented by an exponential softening equation, as described in previous works [11,35,12], and given as:

$$\sigma_b(z) = e^{-\gamma z}\left(\sigma_{\max} - \frac{\sigma_{\max}}{z_{\max}} z\right),\ 0 \leq z < z_{\max} \qquad (3.10)$$

Here $\sigma_{\max}$ is the maximum stress in the bridging zone, $z_{\max}$ is the length of the bridging zone at steady state and γ is a softening coefficient. These three parameters are identified by iteratively optimizing the numerically calculated strain profile vs. the experimental one. To obtain these parameters ($\sigma_{\max}, z_{\max}, \gamma$), the error function is iteratively optimized with random initial values chosen in the following ranges: $0 < \sigma_{\max} \leq \sigma_{\mathrm{c}}$, where σ_{c} is a critical stress, taken equal to the transverse tensile strength of the UD composite and $0 < z_{\max} \leq \Delta a_{\max}$, where $\Delta a_{\max}$ is maximum crack advance of the experiment. With respect to parameter γ no constraint is required, however, older studies [11,35,12,14] result in $0 \leq \gamma \leq 1$. These iterations converge to the same results, independent of the initial choice of parameters, which is considered as the solution of the optimization scheme.

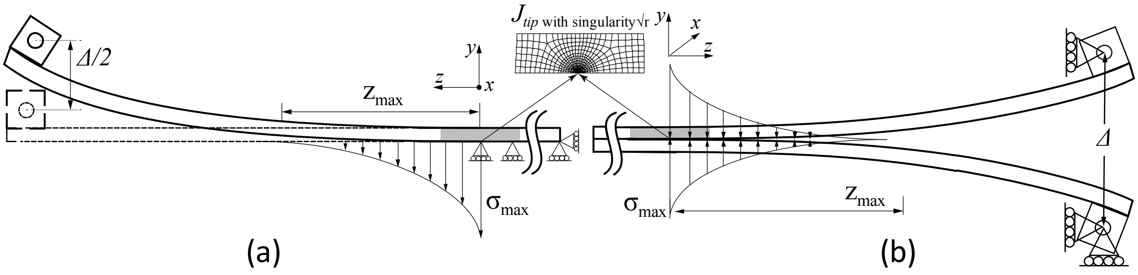

Fig. 3.9: Schematics of the numerical model used for the identification scheme:
(a) Half DCB model, assuming symmetry.
(b) Complete DCB model (arms may be symmetric or not).

Since the optical fiber is placed on the exterior surface of the specimen (Fig. 3.1), the crack tip is not discernible on the recorded strain data, as is the case when the optical fiber is embedded one layer above the delamination plane [12]. Moreover, the conversion of the strain data, from a function of time to a function of crack length, may add some error, depending on the discretization of the crack recognition data and the stability of the experiment. To account for all these uncertainties in the crack tip position, the crack length, on the strain data, is allowed to vary by a parameter χ =±2 mm. This parameter can also absorb the difference between the actual 3D crack propagation and the 2D model originating from a bowing crack front.

To enhance the robustness of the analysis, the fracture toughness at initiation, $G_{I,i}$, is employed. Hence, the optimization algorithm minimizes the norm of the residual error of the experimental strains vs. the numerical ones, plus the error of the numerically calculated J-integral [30] at the crack tip, J_{tip}, and the experimentally evaluated $G_{I,i}$. The J_{tip} is calculated using the Abaqus v6.12 contour integral tool [57], which uses a definition of the domain integral formulation in the absence of body forces, thermal strains and crack face tractions [19]. Details for the calculations of the J_{tip} are given in APPENDIX I. In all models, the quadrilateral, quadratic elements in the vicinity of the crack are transformed into triangular and the middle nodes are shifted to ¼ of the side [19] to model the singularity of $1/\sqrt{\mathrm{r}}$ (r indicates the distance from the crack tip). The residual error minimization scheme utilizes the 'lsqnonlin' optimization routine of Matlab® 8.0 based on a non-linear least-squares fitting. A trust-region reflective Newton's algorithm is employed to solve the constrained non-linear least-square optimization problem with an error function, $\mathrm{f}(\sigma_{\max}, z_{\max}, \gamma, \chi)$, described as follows:

$$\mathrm{f}(\sigma_{\max}, z_{\max}, \gamma, \chi) = \left[\frac{\varepsilon_{FEM} - \varepsilon_{\exp}}{\varepsilon_{\exp}}, \left[\frac{J_{tip} - G_{I,i}}{G_{I,i}} \right]_{rank(\varepsilon_{\exp})} \right] \tag{3.11}$$

To construct the traction-separation relation, $\hat{\sigma}_b(\delta)$, the CODs acquired from the numerical model, $\delta(z)$, are correlated with the identified $\sigma_b(z)$ (Eq. (3.10)) to obtain $\hat{\sigma}_b(\delta)$. The traction-separation relation may also be obtained with the use of $\sigma_b(z)$ and appropriate weight function [103]. Since in the latter case, a numerical integration is necessary, $\delta(z)$ from the optimized solution is used for simplicity. Selected experimentally measured values of CODs, acquired from the crack monitoring images, are compared with computed values and practically no differences are identified.

With the traction-separation relation known, the total ERR at the steady propagation state, $J_{total-SS}$, due to crack growth in the presence of bridging is calculated using the following relation [30]:

$$J_{total-SS} = J_{tip} + J_{I,b} = G_{I,i} + \int_{0}^{\delta_{\max}} \hat{\sigma}_b(\delta) d\delta \qquad (3.12)$$

Here J_{tip}, taken as the fracture toughness at initiation, is considered equal to the experimental $G_{I,i}$, and $J_{I,b}$ is the contribution of bridging to $J_{total-SS}$, calculated by the integral of the tractions $\hat{\sigma}_b(\delta)$, on the crack plane with $\delta_{\max}$ representing the COD at the end of the bridging zone $z = z_{\max}$. The integral in Eq. (3.12) is the ERR due to bridging tractions in the general case of a linear or non-linear model/experiment.

The numerical model adopted for the optimization procedure of the AS4/PPS thermoplastic composite, is schematically shown in Fig. 3.9(b). In this model the full DCB specimen is simulated due to variations of ~0.15 mm in the thickness of the two resulting irregular beams after fracture. This crack morphology is typical for intralaminar cracks as illustrated in Fig. 4.2 and Fig. 5.3. Therefore, the DCB specimen is modeled, with appropriate adaptations on the beams' thicknesses, using discrete thickness measurements from the acquired images in order to follow the actual fracture plane. The model comprises 4,476 quadrilateral, quadratic, reduced integration plain strain elements (Abaqus CPE8R).

For the identification of the thermoset composite specimen with $H = 6$ mm, a symmetric numerical model is adopted as is schematically shown in Fig. 3.9(a) since crack growth is fairly symmetric. This model consists of 2,866 quadrilateral, quadratic, reduced integration plain strain elements (Abaqus CPE8R). However, for the $H = 10$ mm specimen, a symmetric model is insufficient, due to higher variations of the fracture surface during propagation that are taken into account in a similar manner as already described for the AS4/PPS system. Therefore, the entire DCB specimen is modeled (Fig. 3.9(b)). This model is discretized with 7,334 elements of the same type as for $H = 6$ mm. The specimen with $H = 14$ mm is not instrumented with FBGs, thus, no optimization scheme is carried out. However, a numerical model is created to extract the COD profile, necessary for the evaluation of the traction-separation relation as described in Eq. (3.9), and the energetic contribution of bridging. For this purpose, a model with 7,523 quadrilateral CPE8R elements is used to discretize one arm of the specimen, assuming perfect symmetry. The specifics of the extrapolation of the tractions profile to the thickest specimen using the two identified ones are developed in §5.3.4.

In all numerical models the initial thickness loss due to the diamond wire precrack is taken into account in order to reduce the error between the numerical and the experimental specimens' compliance. This error for the thin specimens is substantial, while for the thicker ones it is proven insignificant.

3.6.1.2 Approach with finite process-zone

For the woven E-glass-epoxy system, a quasi-brittle delamination is also observed, however some extended process-zone at the tip is present, attributed to the wavy architecture of the fabric-plies as shown in the corresponding sections (§7.3 and §7.4). For this case a linear softening model is adopted to describe the failure at the crack tip. Thus, in this optimization scheme the closing tractions profile comprises two parts: one for linear softening of the process-zone ahead of the crack tip, followed by the aforementioned exponential softening to depict the bridging phenomena in wake of the crack tip. Therefore, the tractions profile inside the process-zone is defined by the following equation:

$$\sigma_{pz}(z)=\sigma_c-\frac{\sigma_c-\sigma_{\max}}{z_0}z,\ 0\le z<z_0 \tag{3.13}$$

For the bridging part the form of Eq. (3.10) is kept, shifting though the origin of coordinates by the length of the process-zone, z_0, as:

$$\sigma_b(\hat{z})=e^{-\gamma\hat{z}}\left(\sigma_{\max}-\frac{\sigma_{\max}}{z_{\max}-z_0}\hat{z}\right) for\ \hat{z}=z-z_0,\ z_0\le z<z_{\max} \tag{3.14}$$

In this approach, the critical stress, σ_c, is considered constant and equal to the tensile strength of the epoxy, whereas the optimization scheme has one more parameter, the length of the process-zone, z_0.

A schematic of the adopted numerical model is illustrated in Fig. 3.10. In this model J_{tip} is also calculated numerically as already described, however in this case the resulted value is expected to be equal to zero, since the ERR contribution of the crack tip is already included in the process-zone and corresponding tractions, as J_{pz}. Consequently, the optimized error function, with finite process-zone before bridging, $\mathrm{f}_{pz}(\sigma_{\max}, z_{\max}, z_0, \gamma, \chi)$, can be summarized as:

$$\mathrm{f}_{pz}(\sigma_{\max}, z_{\max}, z_0, \gamma, \chi) = \left[\frac{\varepsilon_{FEM} - \varepsilon_{\exp}}{\varepsilon_{\exp}}, \left[\frac{J_{tip} - 0}{G_{I,i}} \right]_{rank(\varepsilon_{\exp})} \right] \tag{3.15}$$

Here the part of the relative error of J_{tip} with respect to zero cannot be defined, and for this reason the error is normalized over the experimentally obtained $G_{I,i}$, defining a logical order of magnitude for the calculated error.

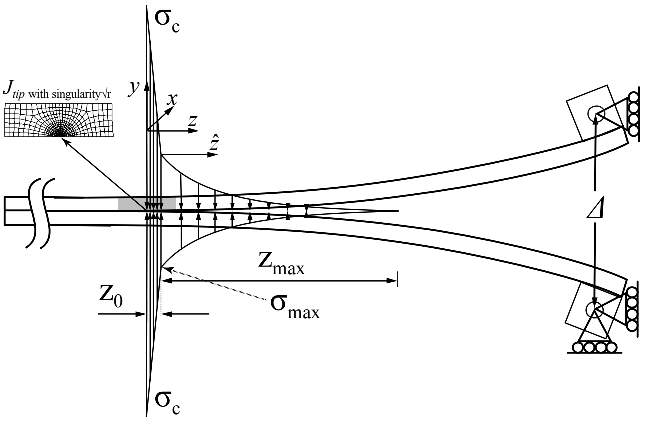

Fig. 3.10: Schematic of the numerical model used for the identification scheme under presence of finite process-zone

To obtain the overall traction-separation relation, $\sigma(\delta)$, the CODs acquired from the numerical model, $\delta(z)$, are correlated with the identified $\sigma_{pz}(z)$ and $\sigma_b(\hat{z})$ (Eq. (3.14) and (3.15)) to form the two partitions of $\hat{\sigma}(\delta)$: $\hat{\sigma}_{pz}(\delta)$ and $\hat{\sigma}_b(\delta)$. The COD at the end of the defined process-zone $\delta(z_0)$ is denoted as δ_1. Moreover, the total ERR at the steady propagation state, $J_{total-SS}$, similar to Eq. (3.12), is calculated as:

$$J_{total-SS} = J_{pz} + J_{I,b} = \int_0^{\delta_1} \hat{\sigma}_{pz}(\delta) d\delta + \int_{\delta_1}^{\delta_1+\delta_{\max}} \hat{\sigma}_b(\delta) d\delta \tag{3.16}$$

The described methodology is adopted to characterize the traction-separation relation in DCB specimens with different geometry and stiffness. Further details, for the scaling effect on the traction-separation relations, and the data treatment, to calculate γ and $z_{\max}$, are given in the corresponding section (§7.4.3), as well as information regarding the size of the numerical models.

3.6.2 Cohesive zone modeling

To verify the validity of the identified bridging tractions and predict the load-displacement response, a numerical model using Abaqus® v6.12 standard cohesive elements [57] with the identified traction-separations relations, $\hat{\sigma}_b(\delta)$, is built. The key parameter of the cohesive elements is the damage factor, $D(\delta)$, causing a degradation of the cohesive elements' stiffness. The overall cohesive response, commonly referred to as 'cohesive law', is schematically represented in Fig. 3.11 and is summarized in the following equation:

$$\sigma = (1 - D(\delta))K_0\delta \;\; with\, D(\delta) = \begin{cases} 0 \; for \;\; 0 < \delta \le \delta_c \\ \dfrac{\delta_1(\delta - \delta_c)}{\delta(\delta_1 - \delta_c)}, \; for\, \delta_c < \delta \le \delta_1, \; \delta_1 = \delta_c + \left(1 - \dfrac{\hat{\sigma}_{b,\max}}{\sigma_c}\right)\left(\delta^d - \delta_c\right) \\ 1 - \dfrac{\hat{\sigma}_b(\delta)}{K_0\delta}, for\, \delta_1 < \delta \le (\delta_{\max} + \delta_1) \end{cases} \qquad (3.17)$$

The cohesive law is built in a stress criterion (Abaqus Maxs) and comprises three distinct regions as depicted in Eq. (3.17): (i) The first one describes the linear response of the intact cohesive elements, with an elastic stiffness K_0, until reaching the critical stress σ_c. (ii) The second segment follows a linear degradation of σ over δ, using the damage factor described in [42], adapted to define the correct maximum opening for this region, δ_1, that corresponds to opening at the maximum identified bridging traction $\sigma_{\max} = \hat{\sigma}_{b,\max}$. The area of the defined truncated triangle (grey region in Fig. 3.11) is equal to $G_{I,i}$. (iii) The third region is defined by the calculated traction-separation relation, $\hat{\sigma}_b(\delta)$. For this part the calculated, by the optimized numerical model, values of δ, are shifted by δ_1 (Fig. 3.11), since the maximum bridging traction, $\sigma_{\max}$, for the identification scheme is taken at the crack tip (Fig. 3.9). Thus, the energetic contribution of the bridging tractions is given by $J_{I,b} = \int_{\delta_1}^{\delta_{\max}+\delta_1} \hat{\sigma}_b(\delta)d\delta$. This shift has no effect on the value of $J_{I,b}$, and for an infinitesimal process-zone at the crack tip, δ_1 is very small compared to $\delta_{\max}$, as shown later from the calculated values. In the case of the woven GFRP the overall $\sigma(\delta)$ is identified so no shift is required.

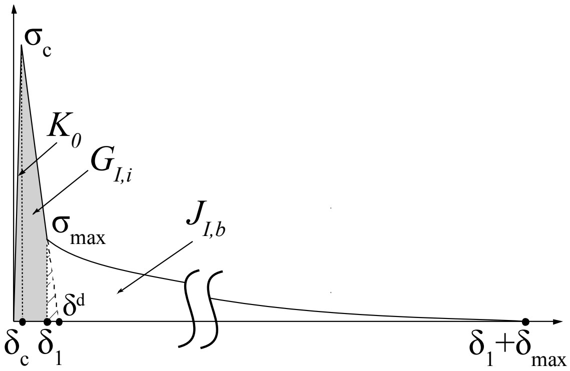

Fig. 3.11: Definition of the traction-separation relation used in the cohesive zone modeling.

In the numerical implementation of the cohesive model, the damage initiation point, σ_c, is considered equal to the 90° tensile strength of the material, taken as $\sigma_c =$ 40 MPa, for the AS4/PPS, being representative for this material [104] and 42MPa for the thermoset system, as given by Gurit SP™ [105]. In addition, the ratio δ_c / δ^d (where δ^d is an auxiliary opening, see Fig. 3.11) is chosen equal to 1%, for better convergence of the numerical solution, reducing the elastic recovery after the element's failure. With these values selected and $G_{I,i} \simeq$150J/m^2 (refer to §4.3.5) for the AS4/PPS comprise an initial stiffness $K_0 \simeq$ 530 GPa/mm and $\delta_1 \simeq$0.007 mm. The corresponding initial stiffness value for the thermoset composite is $K_0 \simeq$325 GPa/mm for $G_{I,i} \simeq$265J/m^2 (refer to §5.3.6). The COD at $\sigma_{\max}$, for the woven GFRP is identified from the optimization scheme as $\delta_1 \simeq$0.015 mm and the initial stiffness is chosen as $K_0 \simeq$305 GPa/mm.

The resultant initial stiffness values are about 30-40 times greater than the $E_x/(1mm)$ of each material and in this way, the compliance of the cohesive layer has a negligible effect on the overall response of the model. The damage variable, $D(\delta)$, is implemented in the cohesive elements in a tabular form of ~600 entries, to provide adequate data for the numerical solver to interpolate the desired damage function and is calculated with a Matlab® script using the identified traction-separation relation $\hat{\sigma}_b(\delta)$ (§3.6.1) and Eq.(3.15).

For the simulations of the DCB experiment, two symmetric beams are modelled representing the actual composite beams with the two steel loading blocks, perfectly bonded to the composite beams. These regions are discretized using quadrilateral, quadratic plain strain elements with reduced integration (Abaqus CPE8R). The actual case is three dimensional however, 2D elements are used for simplicity, while plain stress models are lunched as well, with an unnoticeable difference at the load displacement response, as explained in the comments after Eq. (3.2). The two parts are mutually connected with quadrilateral, linear, cohesive elements (Abaqus COH2D4) modified for zero thickness. An Abaqus 'Tie' constraint is applied to tether the cohesive element zone with the elements of the intact material. This technique allows a very fine mesh for the cohesive zone, while the element size of the rest of the specimen remains within reasonable range. A typical element in the specimen arms along the bridging zone has length of 0.25 mm and its ratio with the cohesive elements is 1/25. This ratio is larger than the minimum recommended [106] for such model cases, so that the static FE solver converges for very small crack increments. The boundary conditions for these models are the equivalent with the ones depicted in Fig. 3.9(b).

The size of the models built to simulate the intralaminar fracture of the AS4/PPS and the thermoset composite system ranges from 22,718 up to 54,730 elements, for the three different thicknesses. This increase in size, apart from the thickness, is also necessary due to longer bridging zone lengths for higher thicknesses. In all cases, enough elements ahead of the crack tip are implemented to allow for precise decay of the strains. This region can reach 20–60 mm of DCB length depending on the specimen thickness (Fig. 4.4 and Fig. 5.6).

In addition, the identified cohesive law for the thermoset composite system is implemented on a cohesive element model of the DCB with boundary conditions that correspond to the designed pure moment configuration. A schematic of this model is illustrated at the insert of Fig. 6.6. The results of this model are compared with the experimental moment-angle response, and the calculated R-curve behavior is used to quantify the difference on cohesive laws for different loading conditions.

Details concerning the cohesive models and the additional numerical tools employed on the investigation of the woven GFRP, are provided in §7.

3.6.3 Embedded cell approach

As it is already mentioned, a micromechanical virtual test - numerical model is created based on the experimental observations of this work [66,67]. In this section, only a brief description is included. The created 3D numerical model is established using the embedded cell approach. In this model the DCB arms and the loading blocks are model using the homogenized properties while the bridging bundles are the embedded cells. The bundles are modeled using 2-node linear beam elements with circular cross-section (Abaqus B31), with the corresponding orthotropic material properties, following cross-sectional profile distributions based on the microscopic observations (§4.3.1 and §5.3.1). The interaction of the beam elements with the homogenized solid parts is simulated using node connector elements (Abaqus CONN3D2). These connectors represent the local transverse failure (strength and fracture energy) of a bundle and the bulk composite. The mechanical properties of the connector elements follow a triangular failure response similar to the first segment of the cohesive law, used for the macromechanical/homogenized damage model (Fig. 3.11), formed though in a force-displacement relation. To model, the random generation of LSB, a random sequence of weak and strong connector, are induced, with the strong connector being 50%, tougher and stronger than the weak, which has a critical strength equal to the considered σ_c and a toughness equal to $G_{I,i}$. Moreover, the failure of the bridging bundles-linear beam elements is introduced in a material level. The boundary conditions imposed are the same with the ones illustrated in Fig. 3.9(b).

The obtained load-displacement and rotation curves from both the micromechanical and the cohesive model are compared with the experimental data. In addition, the reactions and displacements of the connector elements are compared with the identified cohesive law. Moreover, the experimental R-curves are compared with the ERR calculated using the embedded cell approach and the energy calculations from the inverse identification technique. In this thesis results of the virtual-testing only of the CFRP thermoplastic composite are included, while the corresponding results of the thermoset matrix composite are published in [66].

3.6.4 Fracture characterization methodology summary

In summary, the adopted methodology for EOF experimental series, shown in Fig. 3.12, comprises the following steps: In the experimental part the load-displacement curves, crack position, longitudinal strain profile and the cross-section morphology of the fractured specimens are extracted. From these data, experimental R-curves are constructed using the reported equations in §3.2. The numerical modeling involves identification of bridging tractions, predictions of the load-displacement curves using a cohesive model, and micromechanics of bridging. Namely, with the measured strain data and the iterative optimization method, the traction-separation relation, $\hat{\sigma}_b\left(\delta\right)$, is calculated and implemented in a cohesive zone model to predict the load history and obtain the corresponding, numerically estimated, R-curves. In parallel, a numerical model implementing the embedded cell approach is used as a virtual experiment, to provide predictions of the load-displacement response and the R-curve behavior of this composite system. As a final step, the experimental and models' results are compared to draw the necessary conclusions.

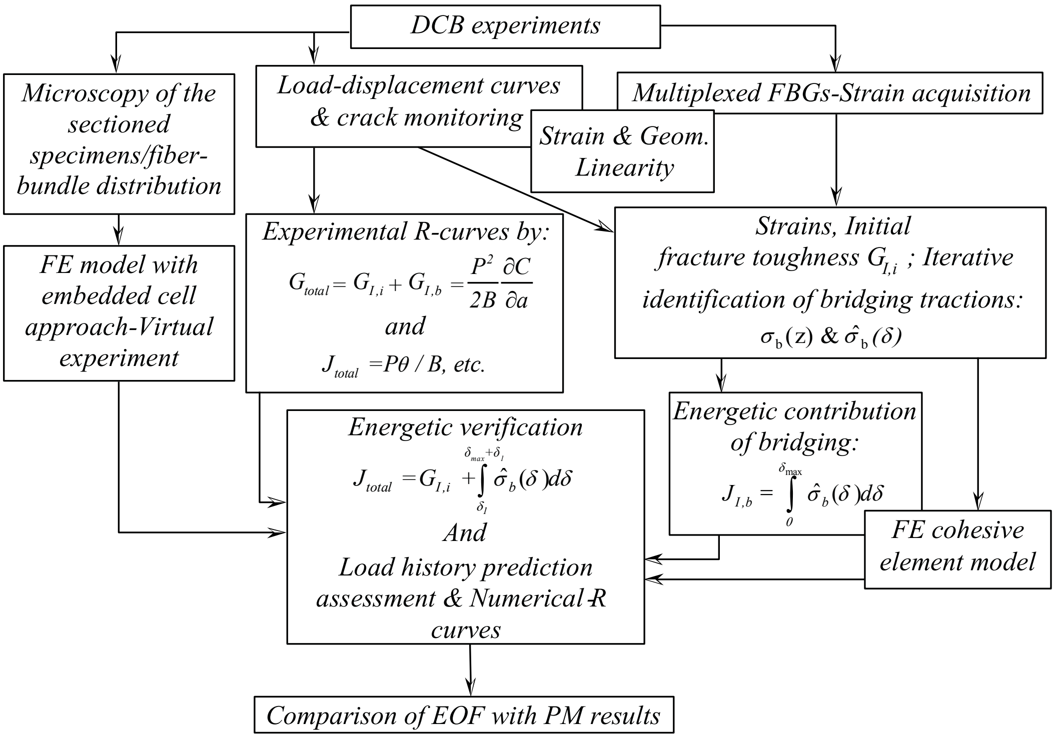
DCB experiments
Microscopy of the sectioned specimens/fiber-bundle distribution
Load-displacement curves & crack monitoring
Multiplexed FBGs-Strain acquisition
Strain & Geom. Linearity
FE model with embedded cell approach-Virtual experiment
Experimental R-curves by:
$G_{total} = G_{I,i} + G_{I,b} = \frac{P^2}{2B}\frac{\partial C}{\partial a}$
and
$J_{total} = P\theta / B$, etc.
Strains, Initial fracture toughness $G_{I,i}$; Iterative identification of bridging tractions:
$\sigma_b(z)$ & $\hat{\sigma}_b(\delta)$
Energetic verification
$J_{total} = G_{I,i} + \int_{\delta_I}^{\delta_{max}+\delta_I} \hat{\sigma}_b(\delta) d\delta$
And
Load history prediction assessment & Numerical-R curves
Energetic contribution of bridging:
$J_{I,b} = \int_0^{\delta_{max}} \hat{\sigma}_b(\delta) d\delta$
FE cohesive element model
Comparison of EOF with PM results

Fig. 3.12: Map of the implemented experimental/numerical characterization methodology.

As a final step, the identified traction-separation relation and the acquired R-curves from the EOF loading conditions are compared with the corresponding behavior from the PM testing configuration, to assess the difference on the fracture response and the corresponding LSB phenomena.

Chapter 4

Intralaminar fracture of UD carbon fiber/thermoplastic polymer-composite

4.1 Materials and specimens

Although carbon/thermoset systems are the most common systems, some carbon/thermoplastic materials are found in specific applications. In particular the AS4/PPS (Polyphenylene sulfide), despite being characterized by moderate transverse tensile and bending strength, along with low fracture toughness, is popular in industrial applications because PPS has low water absorption, very good properties in elevated temperatures and excellent chemical resistance.

On the framework of this study, DCB specimens are cut from a composite plate, which is fabricated by stacking 50 UD layers (~0.135 mm thick) of the carbon/ thermoplastic system AS4/PPS from Cytec, and consolidated in a hot-press. A steel mold is fabricated to accommodate a composite plate with a surface of 300×150 mm^2 for the pressing procedure.

PPS is a semi-crystalline thermoplastic with a melting temperature of ~280°C and a degradation temperature of ~370°C thus, the curing cycle has to be adapted on these characteristics. The applied consolidation profile consists of a ramp to 305°C at 9.5°C/min, which is then kept constant for 1 hour, followed by cooling down to room temperature. The material is consolidated with a pressure of 8 bar applied to the stacked prepreg plies on the constant part of the pressing cycle, as instructed for such types of material [104]. The details of the consolidation cycle are depicted in Fig. 4.1.

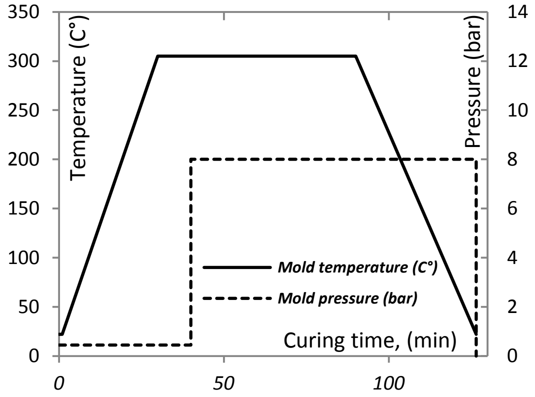

Fig. 4.1: Consolidation cycle applied (temperature and pressure) at the AS4/PPS composite.

The aforementioned fabrication cycle provides a material with very low porosity and a fiber volume fraction of approximately 60%. The elastic properties of the material are determined using an inverse method based on modal analysis. For this purpose a plate with dimensions 100×97×4 mm^3 is fabricated, and consequently tested according to the procedure described in [107]. The obtained elastic properties are: Young moduli $E_z = 128$ GPa, $E_y = E_x = 10.1$ GPa; shear moduli $G_{zx} = 4.9$ GPa, $G_{zy} =$ 5.7 and $G_{xy} = 2.1$ GPa; Poisson's ratios ν_{zy}, $\nu_{zx} = 0.37$ and $\nu_{yx} = 0.49$ (where z is the direction of the fibers, see Fig. 3.1). These values are in perfect agreement with values already reported in [108] for the same material.

The consolidated plate for the fracture experiments has an average thickness of 6.78±0.07 mm, which represents the width, B, of the DCB specimens. One single plate is used to cut three beam specimens of height $H = 6\pm0.05$mm (hereafter called specimen thickness as also reported in the methodology section, §3) and 280 mm length, with an intralaminar precrack introduced as described in §3.1. In all specimens, stainless steel loading blocks (10×10×8mm^3 with a Ø4mm pin hole) are bonded to the DCB specimens with the 3M™ Scotch-Weld™ Structural Plastic Adhesive DP8010. This adhesive system provides good bonding with many low surface energy thermoplastics, such as several grades of polyethylene without special surface preparation. In order to obtain maximum bonding strength, the specimens are post-cured for 5 hours in 50°C.

In total, three specimens are tested with the same conditions, hereafter designated as SP1, SP2 and SP3. After fracture to the steady state, SP1 is impregnated with resin while fully opened and subsequently transversely sectioned and polished using standard techniques, to obtain the cross-sectional morphology of the bridging bundles. These data provide important input to build the micromechanical model described in §3.6.3 and [67].

The SP2 is instrumented with an optical fiber for longitudinal strain measurements during fracture as described in §3.4. The optical fiber is glued on the upper surface of SP2, which is beforehand treated with a chemical primer specifically designed to enhance bonding with cyanoacrylate adhesives and particular plastics, produced by Forbo (Schönenwerd, Switzerland), to improve the adhesion of the optical fiber. The OLCR technique (§3.5) is employed to determine the exact position of the Bragg gratings on the specimen, after the gluing procedure. For this case the center to center distance is 3.2 mm, resulting in a strain measurement region of ~32 mm along the fracture path.

4.2 Fracture testing

The experiments are performed at an ambient temperature of 22°C using a Shimadzu® AGS electromechanical testing machine equipped with a 5 kN load-cell at a constant displacement rate of 3 mm/min with load and displacement recorded at a 10Hz frequency. Crack propagation is monitored by means of a CCD camera (see also §3.1).

In SP3, the total relative rotation, θ, at the loading points is measured using bonded aluminum arms at the loading blocks, with high contrast, printed targets at a span of ~100 mm length (§4.3.4). Their position is recorded with a second high-resolution CCD camera and an in-house digital image correlation algorithm is employed to calculate the relative rotation, between the two arms of the DCB specimen.

4.3 Results and discussion

4.3.1 Fracture morphology

A typical fractured specimen is illustrated in Fig. 4.2(b) along with a polished cross-section at the steady state region where fiber bridging is fully developed. The depicted fracture surface appears irregular being characteristic of the intralaminar fracture as it is reported also in the following sections (§5.3.1). From such micrographs, at different crack lengths, the calculated cross-sections of bridging fiber bundles are in the range of 0.001 to 0.2 mm^2. Complementary information about the microscopic observations is included in Appendix III.

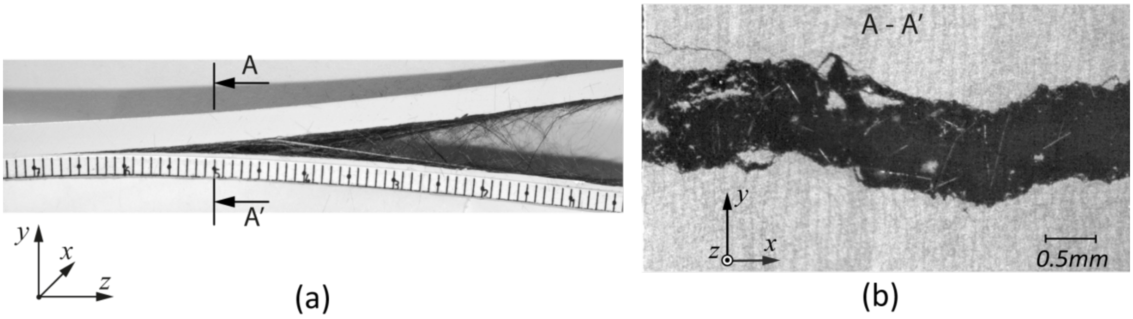

Fig. 4.2: (a) Fractured DCB SP1 and (b) transverse-section, optical microscopy in the fully developed bridging zone.

Photographs of fractured specimen's side views for three different crack lengths are compared with the corresponding snapshots from the micromechanical model, at the corresponding applied displacement, in Fig. 4.3. This comparison demonstrates a perfect match with crack advance for a given displacement, while the activated bridging bundles of the virtual experiment have a similar morphology with the created ones on the actual experiment.

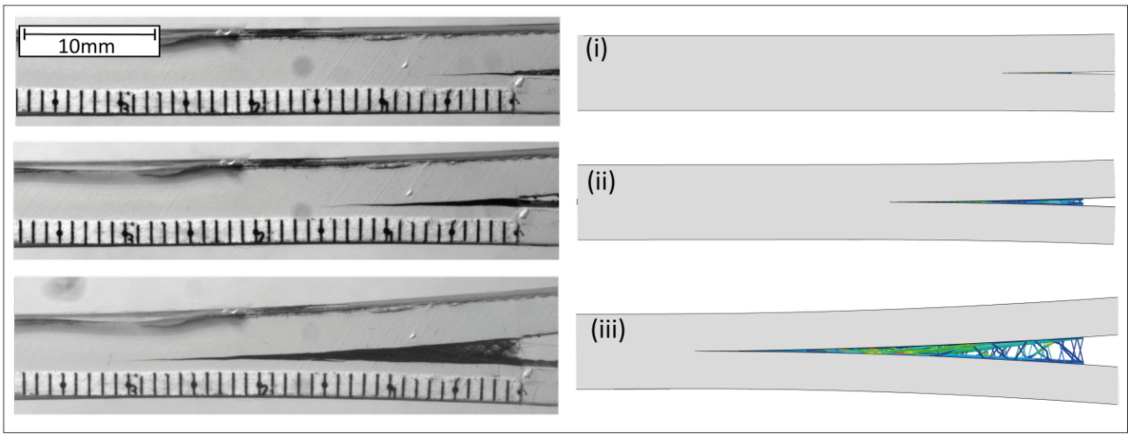

Fig. 4.3: Crack propagation and the development of bridging: photographs of a specimen and snapshots from the micromechanical numerical model at $a = 61$ mm (i), 70 mm (ii) & 85 mm (iii); as published in [67].

4.3.2 Strain measurements

The recorded compressive longitudinal strain's profile vs. testing time for the instrumented SP2 is depicted in Fig. 4.4(a). Three discrete regions can be distinguished here: In region I the recorded strains are essentially equal to zero, corresponding to crack increments well before the array of the FBG sensors. In region II a steep rise is seen, since the crack approaches the individual sensors followed by a 'bend' on the curve when the sensors are after the crack tip and within the bridging zone. The unloading of the specimen at the end of the experiment is observed in the third (III) region. The measurements from the first FBG sensor are rejected due to a dissimilar response compared with the other sensors and, moreover, the strain does not return to zero at the end of the experiment. This is attributed to diameter mismatch on fiber's coated and de-coated region, which prevents smooth bonding on the specimen's flat surface. The fluctuations on the strain data in the bridging zone are attributed to a variation of about 5% in the thickness of the two beams after fracture of the DCB specimen as also depicted in Fig. 4.2(b). The set of data in Fig. 4.4(a) is combined with the crack length, a, over time to create the strain profile vs. a. The created data are subsequently shifted to $a =$ 110 mm, corresponding to a fully developed bridging zone within the steady-state, and employed as the objective strain profile in the identification of the bridging tractions (see Fig. 4.4(b)). To make the optimization scheme less sensitive to noise and more reliable, the individual strain measurements at the FBG locations are enriched by superimposing the strain data taken during $a \pm 1.6$ mm within the steady state based on the observation, that a change of ±1.6 mm in crack length has a negligible effect on the specimen's curvature in the bridging zone. This length is the minimum necessary to create a quasi-continuous strain profile (see Fig. 4.4(b)), being equal to the half mean FBG spacing.

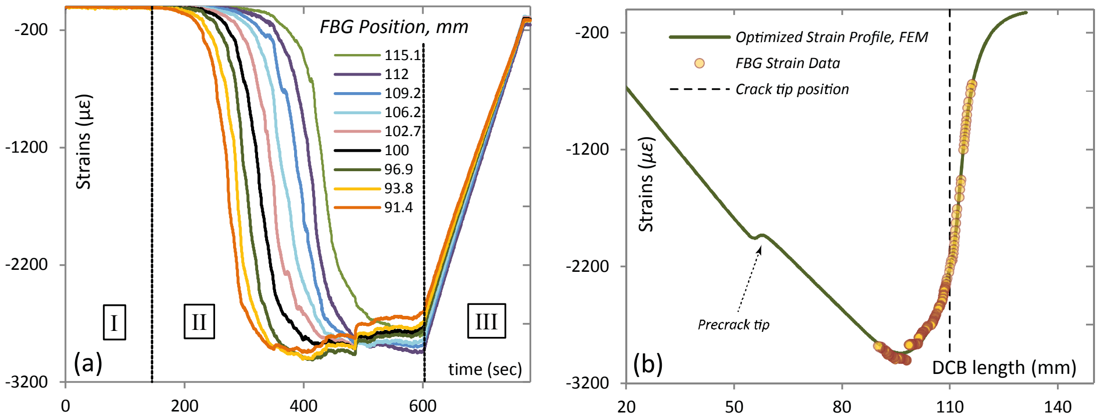

Fig. 4.4: (a) Strains versus time recorded by the FBGs. (b) Experimental strains and optimized numerical strain profiles at $a = 110$ mm; as published in [67].

4.3.3 Traction-separation relation and cohesive model

The strains from the optimized model and the experimental profile are illustrated in Fig. 4.4(b). As depicted in this figure, the crack tip is located at ~3/4 of the maximum recorded strain. The bridging traction parameters (Eq. (3.10)), corresponding to this optimized numerical solution, are as follows: $\sigma_{\max} =$ 4.13 MPa, $z_{\max} =$ 27.75 mm, $\gamma =$ 0.032mm^{-1}. The traction-separation relation, $\hat{\sigma}_b(\delta)$, is obtained by combining the COD, $\delta(z)$, from the optimization scheme with $\sigma_b(z)$. Using $\hat{\sigma}_b(\delta)$, the numerical integration as described in Eq. (3.12) provides an energetic contribution of bridging equal to $J_{I,b} = 1860$ J/m^2. The numerical model used for the optimization is an Abaqus Standard, non-linear analysis, allowing for large displacements. Nevertheless, for the completeness of the analysis, the optimization scheme is re-launched considering only small displacements. The resulting parameters are as follows: $\sigma_{\max} =$ 4.11 MPa, $z_{\max} =$ 25.44 mm, $\gamma =$ 0.024 mm^{-1} and $G_{I,b} = 1779$ J/m^2. Remarkably, the difference between the two solutions is about 4.5% in terms of ERR while the bridging traction parameters are very close, as also illustrated in Fig. 4.5(a). From these two sets of identified parameters, the geometrical non-linearity of the experiment can be considered negligible and with a minor effect on the accuracy of the calculations using a linear model.

The calculated traction-separation relation, $\hat{\sigma}_b(\delta)$, is appended to a cohesive model with a linear softening behavior describing the initial fracture toughness, as designated in Fig. 3.11 at the methodology section. The traction-separation relation from the inverse method and the results of the tractions on the crack face given by the micromechanical model are shown in Fig. 4.5(b) as a function of δ at a crack length in the steady state. These tractions are the sum of the reaction stresses of the numerical connectors that link the solid mesh of the specimen arms with the bridging bundles (§3.6.3). The data in Fig. 4.5(b) demonstrate that the identified traction profile appears as a smooth approximation of the stress-opening relation acquired from the micromechanical model, demonstrating the accuracy of the inverse identification technique and the micromechanical model - virtual testing.

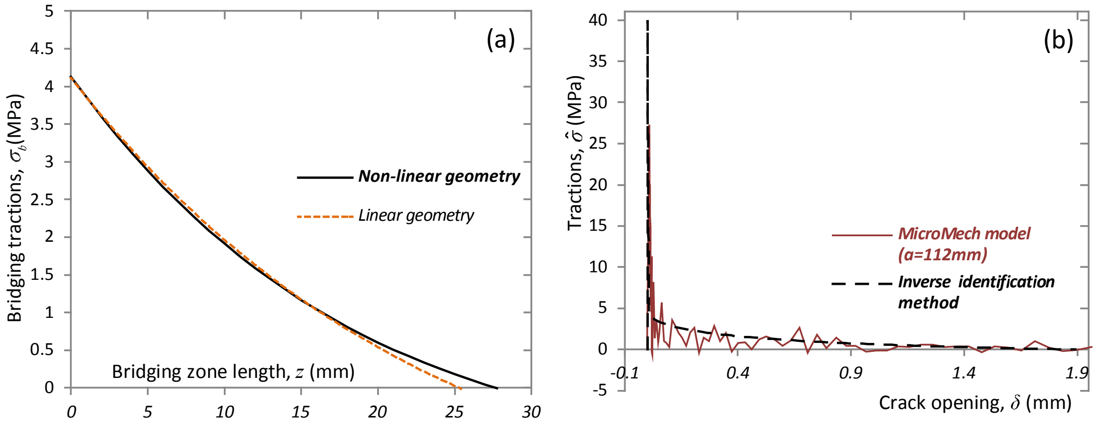

Fig. 4.5: (a) Traction-separation relation inside the bridging zone.
(b) Overall traction-separation relation calculated from the inverse method and corresponding profile from the micromechanical model; as published in [67].

4.3.4 Load-displacement and rotation curves

The recorded load-displacement response of the 3 different specimens is illustrated in Fig. 4.6. The SP2 and SP3 are unloaded at the end of the experiment while the first specimen is impregnated with resin while fully opened for the sectioning procedure (§4.1). The predicted load-displacement response using the identified traction-separation relation in the cohesive model is also shown in Fig. 4.6. As can be observed, the experimental curves are in good agreement with the numerical prediction and, as expected, it is closer to the data of the instrumented SP2 used in the identification scheme, especially after the post peak load where steady state growth starts and the identification is carried out. The difference in the rising part may be attributed to the use of the single traction-separation relation, identified in the steady state, for the entire load displacement curve, assuming no change on the bridging law till steady-state, but just a natural evolution. This assumption appears to have a minor effect on the estimated response.

The load-displacement prediction from the micromechanics based virtual test is also presented in Fig. 4.6. The results of this model provide a scattered response (similar to the experimental one), as the bridging bundles are discretely modeled, yet, they lie within the experimental data range and closer to the data corresponding to SP3.

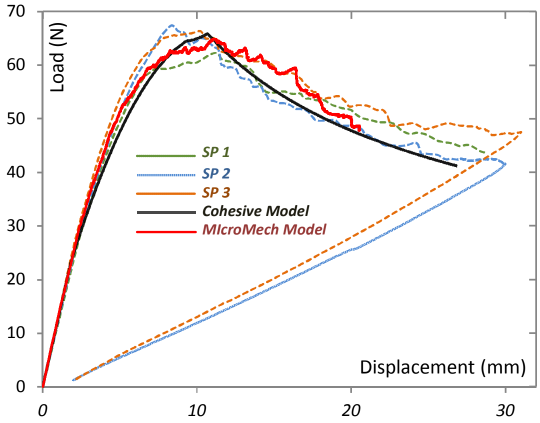

Fig. 4.6: Experimental and numerically obtained load-displacement response. The SP 2 & 3 are unloaded at the end of the test; as published in [67].

Two snapshots of the experimental setup for the measurement of the rotations, θ, at the loading points, at the start and towards the end of the experiment are shown in Fig. 4.7(a). The experimental P-θ response along with the corresponding predictions from the cohesive model and the micromechanical simulation, are displayed in Fig. 4.7(b). In the numerical models, θ is considered as the relative rotation of the loading blocks (Fig. 3.9(b)). The fluctuations of the experimental response in this figure are similar to the data in Fig. 4.6. The experimental data and simulations on the P-θ (Fig. 4.7(b)), are employed to calculate the ERR at several crack lengths using Eq. (3.6).

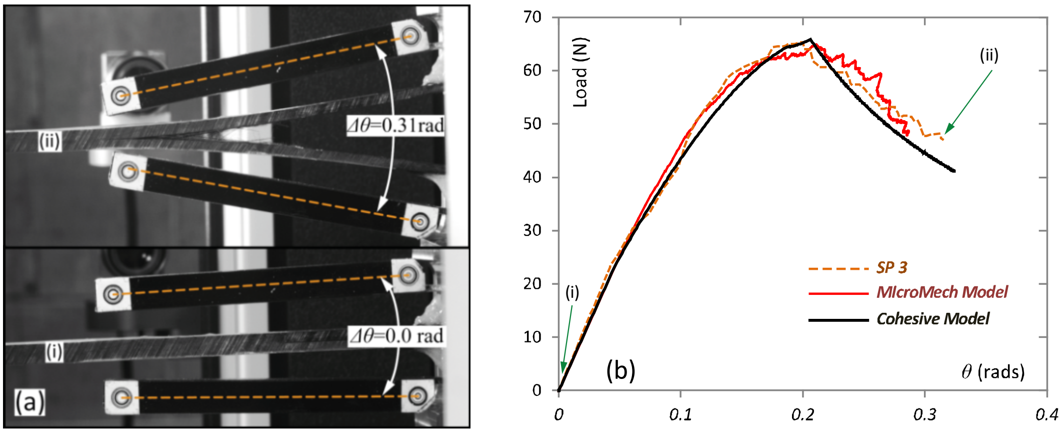

Fig. 4.7: (a) Experimental setup to acquire the rotation at the loading points. (b) Experimental and numerically obtained load-rotation response (see text for details); as published in [67].

4.3.5 Resistance curves

The fracture toughness at initiation, for the three tested specimens using (Eq. (3.3)), is found to be $G_{I,i}$ = 150±10J/m^2, based on the deviation from linearity and visual observation criterion [49], that provide approximately the same value with a load $P \simeq 24$N. Nonetheless, peak loads on the load-displacement curves (Fig. 4.6) are located at a crack advance of ~20mm, being characteristic of the toughening occurring in an intralaminar fracture advance. Furthermore, for intralaminar fracture, with such a precrack no pop-in effect is observed, and the crack advance is smooth from the very first increment. Interestingly, the recorded value of $G_{I,i}$, is practically equal to the initiation value in interlaminar fracture for the same material [35].

The resulting R-curves for the three different specimens, as calculated by the MCC method, are represented in Fig. 4.8(a). As depicted in this figure, intralaminar fracture of fiber reinforced composites displays a relatively high scatter, as reported in the literature [16,17,85] and also the following chapter of this thesis (§5), which is attributed to large discrete bundles that absorb a significant amount of energy before failure.

In addition, the MCC method is used to evaluate the R-curve, using the predictions of the cohesive model on the P-Δ curves and defining the crack tip by the last intact cohesive element (i.e., $D=$ 0), This curve is also included in Fig. 4.8(a) and is in good agreement for the greatest part of the crack advance. Some transition in the rising part exists which may be attributed to transient evolution of the LSB also observed in the study of the carbon/thermoset composite as reported in §5.3.5, §5.3.6 and discussed in Appendix III.

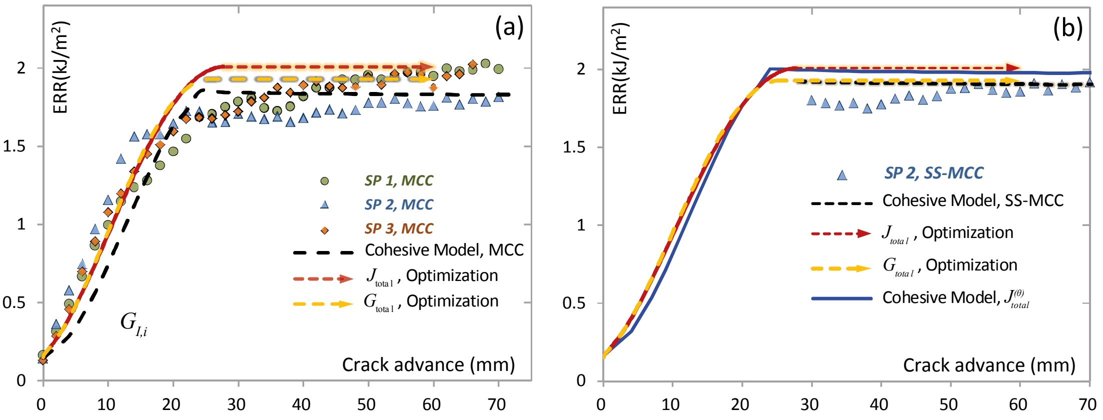

Fig. 4.8: (a) Experimental R-curves compared to numerically predicted R-curves (see text for details). (b) Experimental R-curves and numerical ones, using the SS-MCC method, $J^{(\theta)}_{total}$ and the calculated traction-separation relation; as published in [67]

Also shown in Fig. 4.8(a) is the R-curve formed by incrementally integrating $\hat{\sigma}_b(\delta)$ using Eq. (3.12), for each increment, k, with $\delta_{\max,k}(z_k = \Delta a_k)$ until $\Delta a = z_{\max}$:

$$J_{total}(\Delta a_k) = J_{tip} + \int_0^{\delta_{\max,k}(z_k)} \hat{\sigma}_b(\delta) d\delta, \qquad for\ 0 \le z_k \le z_{\max} \tag{4.1}$$

After $\Delta a = z_{\max}$ the value is considered constant and equal to $J_{total-SS}$. The same procedure is repeated with $\hat{\sigma}_b(\delta)$ calculated using the linear model (i.e., neglecting the geometrical non-linearity in the identification of $\hat{\sigma}_b(\delta)$). As shown in Fig. 4.8(a), the results are very close to the full, non-linear analysis with an error at the steady state of ~4% ($J_{total-SS}$ =2010 J/m^2 vs. $G_{total-SS}$ = 1929 J/m^2). The equivalent error with respect to the cohesive model, using MCC, is ~8%.

Furthermore, the reaction load, P, and rotation, θ, as predicted by the cohesive model, are used in Eq. (3.6) to obtain $J_{total}^{(\theta)}$ as a function of crack increment. The data are shown in Fig. 4.8(b) together with the ERR evolution for the linear and non-linear analyses (also in Fig. 4.8(a)). At this point, it should be noted that $J_{total}^{(\theta)}$ and J_{total} are almost in perfect agreement, as expected since both measures account for geometrical-non-linearity. Moreover, the data in Fig. 4.8(b) show the calculated ERRs using the SS-MCC method for the experimental data of the SP2. Here, the calculated ERR (by SS-MCC) from the cohesive model in the steady state practically collapses with the incremental integration using the identified bridging law, assuming linear geometry on the numerical model, and the same effect is depicted on the experimental data. Thus, the difference between $G_{total,SS-MCC}$ vs. $J_{total-SS}$ and $J_{total}^{(\theta)}$ is ~4%, which is very close to a similar comparison from other studies [109]. A previous study [110] compares the R-curve obtained by the compliance method with and without calibration, reports a similar error (2-10%) depending on the method, while the MCC approach is not compared. The results of the previous analysis imply that, if the full series of data are used (from initiation till steady state), the MCC method cannot capture the ERR evolution very well, while a calibration method using only data from the steady state (i.e., SS-MMC) substantially improves the accuracy as also analyzed in §3.2.1.

The results of the micromechanics based virtual experiment are used to calculate the ERRs and construct R-curves as shown in Fig. 4.9. The position of the crack tip in the micromechanical model is defined by the stress concentration point in the isostress contour plots. The data on P, Δ and θ from this model are used to calculate $J_{total}^{(\theta)}$ as well as the ERR with the MCC method in terms of crack advance to construct R-curves, which are compared with the experimental values from SP3 (Eq. (3.2) &

(3.6)). Remarkably, the micromechanics based virtual experiment and the actual test are in good agreement, demonstrating the robustness of the implemented embedded cell technique, while the error produced considering linear response and the MCC method is ~11%, compared with the more realistic data from $J_{total}^{(\theta)}$. This difference with the experimental data can still be improved by using an SS-MCC fitting scheme at ~8% (Fig. 4.9). Note that the micromechanical model provides the same order of fluctuation in the R-curve, since it is associated with the process of generation and fracture of the fiber bundles.

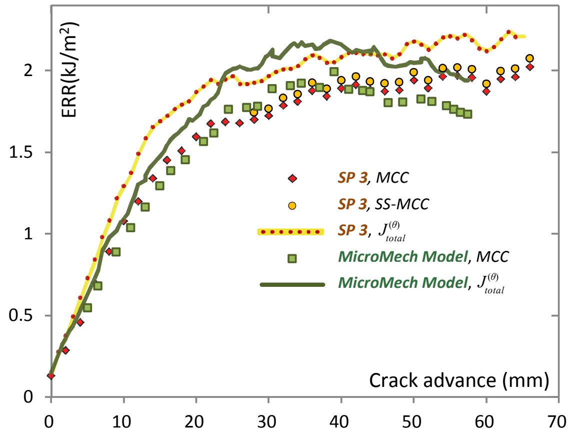

Fig. 4.9: R-curves from experiment and the virtual testing using MCC, SS-MCC and $J_{total}^{(\theta)}$*;*
as published in [67]

A comparison of the ERR results with the corresponding interlaminar values for the same material [11,35] indicates that $G_{I,b}$ or $J_{I,b}$ is about 1.8 - 2.3 times greater than the interlaminar values for similar beam thicknesses, while analogous trends are also described in other recent works [17,85]. However, the initial fracture toughness is practically the same: $G_{I,i} \simeq 150$ J/m^2 [35].

4.4 Summary of key points

- The results of this thorough analysis demonstrate that the response of DCB AS4/PPS specimens subjected to mode I under presence of LSB, can be considered linear elastic with an expected underestimation of the maximum ERR of ~4%, when an appropriate compliance calibration scheme is used (SS-MCC). The weakness of the compliance calibration schemes is that their accuracy depends on the experimental scatter and the chosen fitting scheme.

- The independent inverse identification scheme, that renders the traction-separation relation, provides alike R-curves with the J-integral using the rotations at the loading point.
- Bridging phenomena in fiber reinforced composite materials leads to a clear increase of the material's fracture resistance. Even though the initial fracture toughness of the AS4/PPS composite material system is moderately low, the ultimate fracture resistance can reach the same level of a system with double initial fracture toughness and higher strength as described later (§5). This can be attributed to higher energy absorption on the regeneration of bridging bundles along the length of the DCB specimen as will also be discussed in (§5.5).
- The micromechanics-based implemented virtual test is a very useful tool to characterize the damage tolerant domain of fiber reinforced composites, shedding light on the micromechanical events that take place in the evolution of LSB.
- The maximum calculated ERR at the steady state of an intralaminar fracture configuration is significantly higher than the corresponding values in interlaminar fracture [35] and this can be attributed to the intensity of LSB, while the initial fracture toughness is basically the same. A similar response has also been reported in previous works [85,17].

Chapter 5

Intralaminar fracture of UD carbon/epoxy composite; i) Convectional DCB

5.1 Materials and specimens

For this part of this study, DCB specimens are produced from a composite plate, fabricated by stacking 50 UD layers (cured thickness of 0.2 mm), of the carbon/epoxy prepreg system SE-70 from Gurit SP™, using standard autoclave procedures in vacuum conditions and a uniform pressure of 3 bar. The maximum curing temperature of 78°C is reached after 3 h of a heating ramp at 0.3°C/min and the overall cycle is 16 h, being on the most conservative side of the directions of Gurit SP™ [105], given that the plate is quite thick. The plates are cured using an in-house fabricated mold consisting of 10mm thick spacers and a rigid cup, to ascertain a uniform thickness of the plate and promote repeatability in the fabrication procedure. This mold forces the thickness of the plate to be equal to the nominal, while it allows trapped air to escape and resin flow on the sides. More details are provided in Appendix II. This procedure provides a high quality composite material, with less than 1% of void content.

The cured plate has a thickness of 10±0.07 mm, which represents the width, B, of the DCB specimens for the intralaminar fracture with length of 360 mm and width of 200 mm. Strips of 10 mm in width are cut from the outer parts of the plates to eliminate the effects of the manual lay-up procedure. The specimen production is split into two fabrication batches. For the first batch (#1), one single plate is used to cut beam specimens of thickness $H = 6$ and 10 mm and length 340 mm. The same procedure is repeated for the second batch (#2) of specimens, used for the fabrication DCB specimens with $H = 10$ and 14 mm. The mean resulting tolerance in thickness is ±0.05 mm. Subsequently, a 60 mm intralaminar precrack is introduced in each beam by the use of diamond wire saw, as described on the methodology description section (§3.1) and depicted in Appendix II.

Loading of the specimens is achieved with two cubic steel loading blocks, with sides of 10 mm and pin holes of Ø4mm, glued on each specimen with an Araldite® 5 min epoxy adhesive. The blocks' surfaces and the composite beams are extensively roughened in the region of the adhesion to ensure strong bonding (see Appendix II).

In addition, an optical fiber with 10 multiplexed FBG sensors is glued on the upper surface of two selected specimens of $H = 6$ mm and $H = 10$ mm. The center to center distance per sensor, as measured with the OLCR technique, is ranges for 3.3 to 4.4 mm including the two tested specimens, resulting in a strain measurement region of ~36 mm along the fracture path. More details on this measurement technique are found in §3.5.

For the acquisition of the longitudinal, transversal and in-plane shear modulus, the corresponding ASTM standard experimental procedures are adopted [111,112,113] and the necessary material for this test is produced using the aforementioned procedures. The measured values are as follows: $E_z =$118.7 GPa, $E_y = E_x =$7.7 GPa and G_{zx}, $G_{zy} =$3.8 GPa (where z is the direction of the fibers, see Fig. 3.1). The onset of material non-linearity is evaluated using a uniaxial test for a 90^0 specimen, as shown in Fig. 5.1. Based on these data, a fiber volume fraction $V_f =$54% is evaluated employing the resin properties provided by Gurit SP™ [105] as a resin modulus of $E_m =$3.6 MPa and for a fiber longitudinal modulus $E_f =$217 MPa. The complementary properties for the orthotropic laminate are calculated using the rule of mixtures, with the Halpin-Tsai micromechanical semi-empirical correction [2], for fiber properties obtained by [114]. The corresponding calculated material properties are: $G_{xy} =$3.1 GPa, ν_{zy}, $\nu_{zx} =$0.314 and $\nu_{yx} =$0.427.

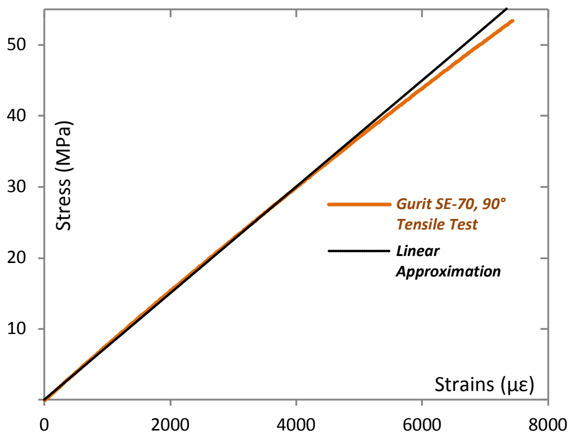

Fig. 5.1: Stress–strain response of the Gurit SP™ thermoset material, under transverse tensile test; as published in [55].

5.2 Fracture testing

The experiments are performed at room temperature using an Instron® 5848 MicroTester equipped with a 2 kN load-cell, with a constant displacement rate of 3 mm/min and data acquisition rate of 10 Hz, while crack propagation monitored by means of CCD camera (see also §3.1). A photo of the testing fixture with a mounted specimen is included in Appendix II.

5.3 Results

5.3.1 Fracture morphology

The fracture of this UD composite laminate is characterized by LSB as it is depicted in the side views of fractured specimens in Fig. 5.2: Typical side views of fractured specimens of all tested thicknesses; as published in [55].Fig. 5.2. From these pictures is suggested that the extent of the bridging zone on the wake of the crack increases with specimen thickness, as also confirmed with forth-presented results. Micrographs of the fracture surfaces and cross-sections of specimens with $H = 6$ and 10 mm, captured at the fully developed steady-state, are illustrated in Fig. 5.3. The depicted images suggest that bridging consists of fiber bundles with section areas in a range of ~0.007 to 0.08 mm^2. Based on the morphology in Fig. 5.2 and Fig. 5.3, the dominant damage mechanisms are fiber-matrix debonding followed by failure of fibers and fiber bundles. In addition, fracture surfaces present quite rough profiles (Fig. 5.3) as compared to similar profiles in interlaminar fracture [14].

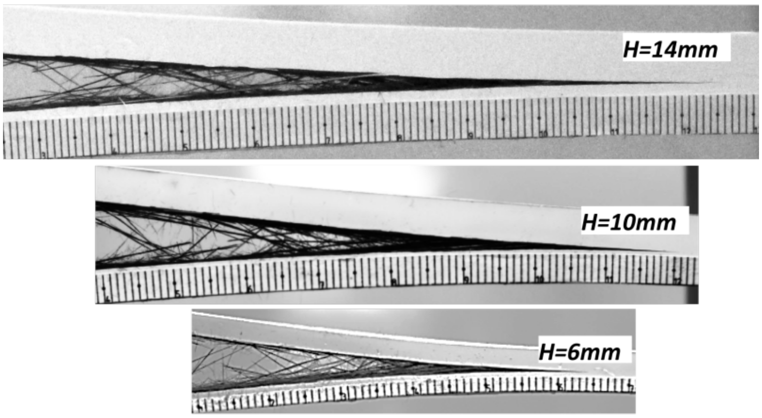
H=14mm
H=10mm
H=6mm

Fig. 5.2: Typical side views of fractured specimens of all tested thicknesses; as published in [55].

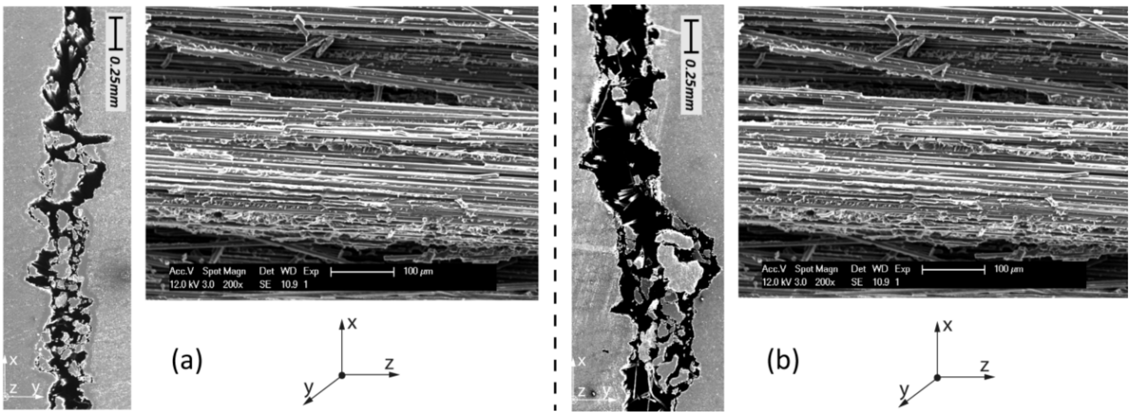
0.25mm
Acc.V Spot Magn Det WD Exp 100 μm
12.0 kV 3.0 200x SE 10.9 1
(a)
x
z
y
0.25mm
Acc.V Spot Magn Det WD Exp 100 μm
12.0 kV 3.0 200x SE 10.9 1
(b)
x
z
y

Fig. 5.3: Fracture surfaces and transverse-sections in the bridging zone at fully developed steady-state for
(a) $H = 6$ mm (b) $H = 10$ mm; as published in [55].

5.3.2 Load-displacement response

The load-displacement curves of all tested specimens, of the three thicknesses investigated in the present study are shown in Fig. 5.4. In this figure (Fig. 5.4) are also included typical unloading curves which are nearly linear while the remaining displacement at zero loads is attributed to the compression of the created fiber bundles. A comparison of the energy under these unloading curves with their linear approximations is below 3%.

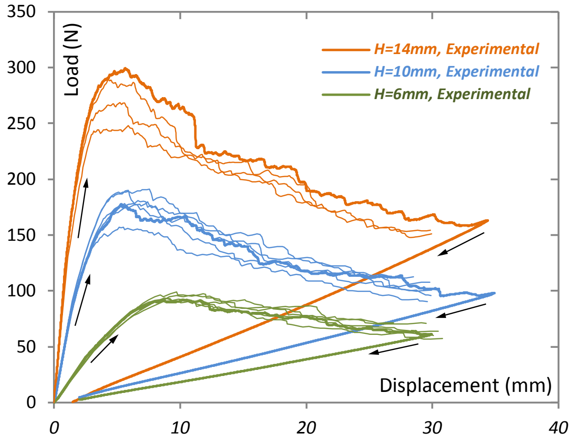

Fig. 5.4: Load-displacement curves for specimens $H =$ *6, 10 and 14 mm and typical unloading response at the end of the test*

5.3.3 Strain data

The compressive strain's profile for the thin specimen ($H = 6$ mm) is depicted in Fig. 5.5(a). The data in Fig. 5.5(a) can be grouped in three distinct regions: the first reflects the zero strains that correspond to the crack length well before the array of the FBG sensors, the second consists of a steep rise, as the crack approaches the individual sensors and subsequent 'bending' of the curve when the sensors are in the bridging zone. The third region corresponds to the unloading of the specimen. The maximum recorded strain value is lower than the elastic limit of this material (see Fig. 5.1), thus supporting the use of a linear elastic material model as mentioned in §3.6.

The strain-time data are combined with crack length-time data to obtain strains in the FBGs as a function of crack length and subsequently shifted to a unique origin $a =$ 107 mm in the steady state (Fig. 5.5(b)). To make the optimization scheme less sensitive to noise and more reliable, the individual experimental strains at the FBG locations are enriched by superimposing the strain data taken during $a \pm 2$ mm within the steady state based on the observation that a change of ± 2 mm in crack length has a negligible effect on the specimen's curvature in the bridging zone. With this technique the reference strain profile used for the optimization scheme, become quasi continuous as illustrated in Fig. 5.6. At this point, it has to be noted that for specimen with $H = 6$ mm, the strains from the FBGs at 93 and 113 mm from the load-point application are excluded from the analysis due to inaccuracies of the measured strains originating from residuals of the optical fiber's original coating and/or defects introduced during the placement of the optical fiber.

The axial strain profile of the specimen with $H = 10$ mm, is non-smooth and discontinuous, which originates from fluctuations on the crack's surface (see also Fig. 5.2 and Fig. 5.3), which cause a variation in created arm thickness of about 2.5% in some specimens, of all the three investigated thicknesses, with negligible effects on the load-displacement response and on the R-curves. This behavior is attributed to the lack of a clear resin zone compared to a delamination case, in which the interlaminar resin region governs the crack propagation path. The aforementioned change in thickness translates into stiffness variation of 7%, taking into account the area moment of inertia of the beam's section, proportional to $(H/2)^3$. Thus, to simplify the analysis, the strain data from 4 FBGs in these regions are allowed to fluctuate by ± 3%, in order to obtain a smooth strain profile, which is then used in the simulations.

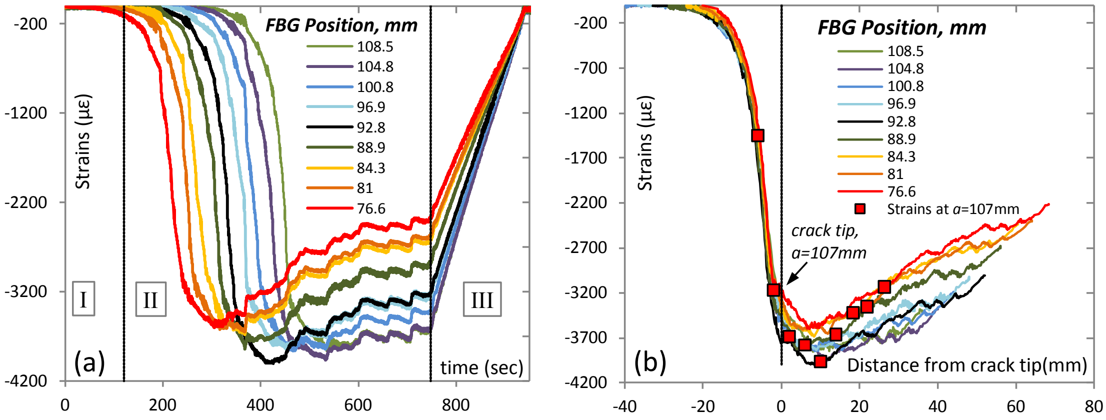

Fig. 5.5: (a) Strains versus time recorded by the FBGs for specimen $H = 6$ mm. (b) Strains versus distance from crack tip shifted to $a = 107$ mm for specimen $H = 6$ mm; as published in [55].

5.3.4 Identification of bridging tractions

The measured and numerically obtained optimized strain data for both thicknesses are illustrated in Fig. 5.6. The corresponding calculated bridging traction parameters (Eq. (3.10)) for the two thicknesses analyzed are: $\sigma_{\max} = 8.19$ MPa, $z_{\max} = 25.5$ mm, $\gamma =$ 0.12 mm^{-1} ($H = 6$ mm) and $\sigma_{\max} = 8.39$MPa, $z_{\max} = 40.5$ mm, $\gamma = 0.082$ mm^{-1} ($H = 10$ mm). Interestingly, a practically independent maximum bridging traction, $\sigma_{\max}$ (Eq. (3.10)), is identified. Given that the volume fraction for all tested specimens is the same, the microstructure around the crack tip is expected also to be the same. Thus, $\sigma_{\max}$, can be considered as a material constant, reflecting an average characteristic strength of the microstructure around the crack tip. When compared with the corresponding parameter in interlaminar fracture on the same material ($\sigma_{\max} = 1.38$

MPa), it is about 6 times greater. Some complementary analysis regarding the effect of microscopy on $\sigma_{\max}$ is included in Appendix III.

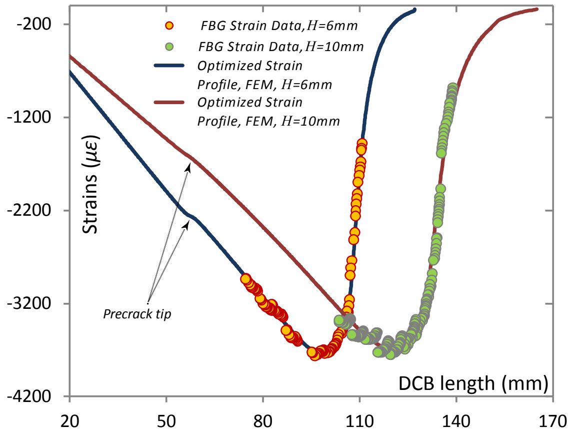

Fig. 5.6: Experimental strains and optimized numerical strain profiles; as published in [55].

Based on the thickness dependency of bridging tractions in interlaminar fracture of glass/polyester [18] and carbon/epoxy unidirectional composites [14], the bridging tractions in the $H=14$ mm specimen are established by utilizing the identification results of the $H=6$ and 10 mm specimens as follows: (a) The maximum bridging traction $\sigma_{\max}$ is considered as a characteristic parameter of the bridging mechanism at the crack tip independent of thickness. Thus, it is taken as the average value of the other two identified thicknesses. (b) The relationship between $z_{\max}$ and H is assumed linear (Fig. 5.9). (c) The exponential softening parameter γ and the corresponding thickness satisfy the relation $\gamma H = const$. Therefore, based on the above considerations, the resulting bridging parameters (Eq. (3.10)) for $H=14$ mm are: $\sigma_{\max} =$ 8.29 MPa, $z_{\max} =$ 55.5 mm, $\gamma = 0.059$ mm^{-1}. The bridging tractions profiles, for all investigated thicknesses, as a function of the distance from the crack tip, are shown in Fig. 5.7.

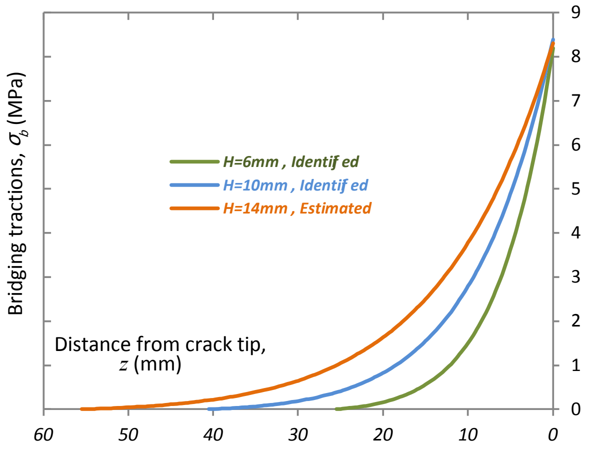

Fig. 5.7: Calculated bridging tractions profiles.

The calculated bridging profiles are coupled with the CODs, acquired from the optimized numerical models to construct the traction-separation relations $\hat{\sigma}_b\left(\delta\right)$ for both thicknesses, as illustrated in Fig. 5.7.

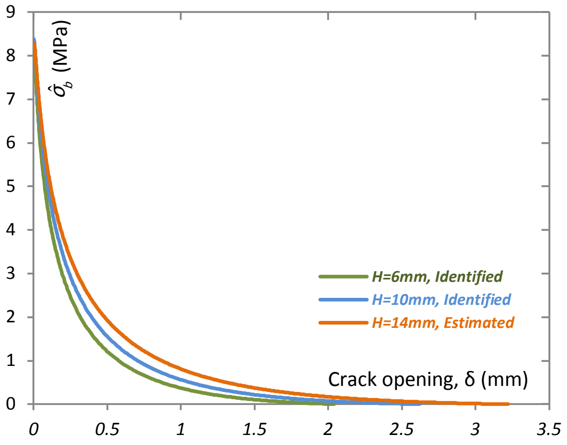

Fig. 5.8: Calculated traction-separation relations; as published in [55].

In addition, the angle of the each DCB arm, within the bridging zone, is calculated as $\varphi \approx \tan\varphi = d\delta / dz$. The maximum angle, $\varphi_{\max}$ and $\delta_{\max}$ at the end of the bridging zone ($z = z_{\max}$) of each specimen thickness as a function of H are shown in Fig. 5.9. These illustrated results indicate that $\varphi_{\max}$ has a similar dependency on H as parameter γ, while $\delta_{\max}$ and H appear to have a linear relation. The calculated $\varphi_{\max}(H)$ has a similar trend with the one reported in [115], where the relation of crack tip opening angle with width (equivalent of B, but for compact tension specimens) is investigated on cohesive laws, of aluminum specimens. With $\hat{\sigma}_b(\delta)$ and $\delta_{\max}$ known, the ERR due to bridging $J_{I,b}$ is calculated from the integral in Eq. (3.12). It is interesting that, for the three specimen thicknesses investigated herein, $J_{I,b} / \sigma_{\max} z_{\max} \tan\varphi_{\max} \simeq 0.068$. This simple scaling relationship suggests that the same damage and fracture mechanisms appear in all specimens with different thickness.

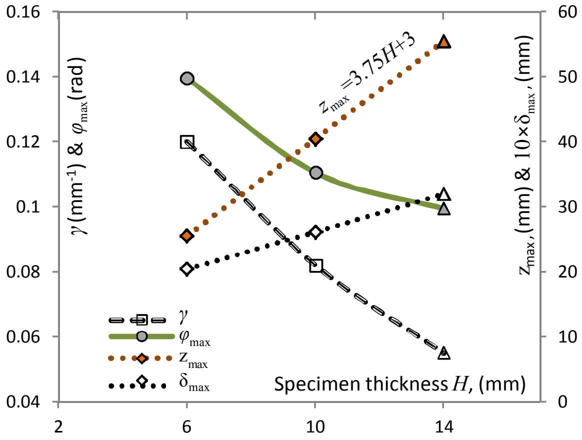

Fig. 5.9: Bridging zone length, exponential softening parameter and maximum angle at the end of bridging zone versus specimen thickness; as published in [55].

5.3.5 Cohesive zone modelling

The identified traction-separation relations for the three thicknesses as presented earlier, are used in a cohesive zone model (§3.6.2) to predict the load displacement response and R-curves. The results of this analysis are illustrated in Fig. 5.10. The data in Fig. 5.10 show that the maximum load is moderately overestimated in all three thicknesses, but the post peak response is very well predicted by the adopted cohesive model. The aforementioned overestimation around the peak load, may be attributed to changes in the growth pattern bridging zone, i.e., from transient growth to a steady propagation, while in the model a single traction-separation, identified at the steady state, is used throughout the fracture process. This may be attributed to some small transition in evolution of the bridging buddle size while further discussion on this matter is included in Appendix III.

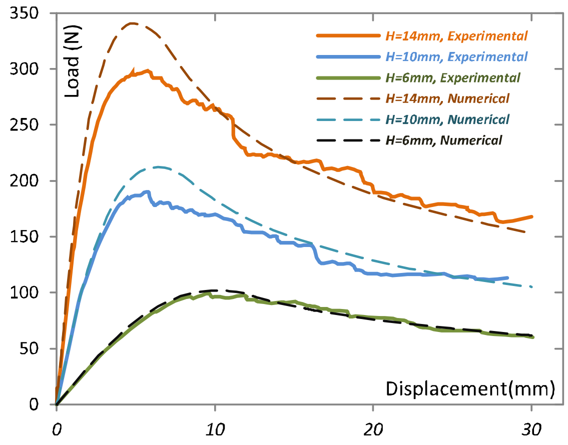

Fig. 5.10: Experimental and corresponding numerically obtained load-displacement response; as published in [55].

5.3.6 Resistance curves

The resulting R-curves, for the three different thicknesses, are represented in Fig. 5.11. These curves are created using the MCC method and are the averages of at least 4 specimens per thickness, while the error bars represent the standard deviation of the total number of experiments per thickness. This intralaminar system intrinsically displays a tendency for fluctuations in the R-curves. This behavior originates from the lack of a well-defined rich resin path, compared with interlaminar fracture. This feature also has a noticeable effect on the size of the bundles (Fig. 5.2), which are generally greater than those in interlaminar fracture.

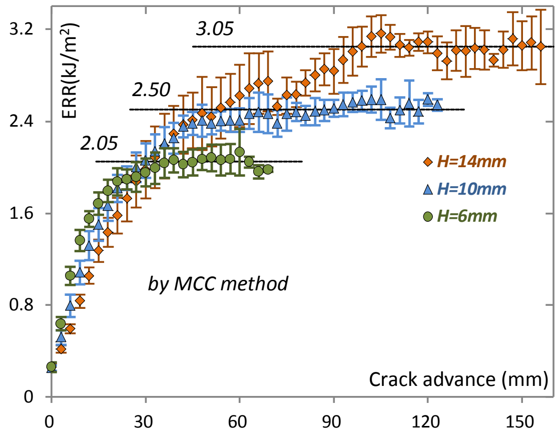

Fig. 5.11: Averaged R-curves, per specimen thickness. The first point indicates the fracture toughness of the composite; as published in [55].

A comparison of the ERR results at steady state propagation, $G_{total-SS}$, with the corresponding interlaminar values [14], indicates that $J_{I,b}$ is at least 2.2 times higher than the interlaminar values for the same material and similar beam thicknesses. Analogous trends have also been described in other recent works [85,17]. However, the initiation toughness is practically the same: $G_{I,i} = 285$ J/m^2 (intralaminar) and 300 J/m^2 (interlaminar) using the CC approach in both cases, and 260 J/m^2 using the MCC in intralaminar case. The data in Fig. 5.11 illustrate an increasing trend of the ERR at the steady-state with ascending steps of 20% per thickness, suggesting a strong thickness effect in maximum fracture toughness, as has also been reported in previous works [14,18] and indicated in [6,7]. The overall shape of the R-curve also varies over the different specimen thicknesses with a steeper initial slope for the thinnest specimen. This behavior has also been previously reported, and can be explained by the increase in bridging zone length along the thickness [8,9].

Based on the aforementioned load history prediction from the cohesive models (Fig. 5.10) and by defining the crack tip in the numerical models by the last intact cohesive element (i.e., $D = 0$), measured from the end of the specimens, R-curves for the three investigated thicknesses are formed, using the MCC method. The predicted R-curves shown in Fig. 5.12 agree very well with the experimental results of the corresponding specimens. Similar to the load-displacement curves (Fig. 5.10), the transitional part is overestimated by the simulations as explained earlier in § 5.3.5 and included in Appendix III.

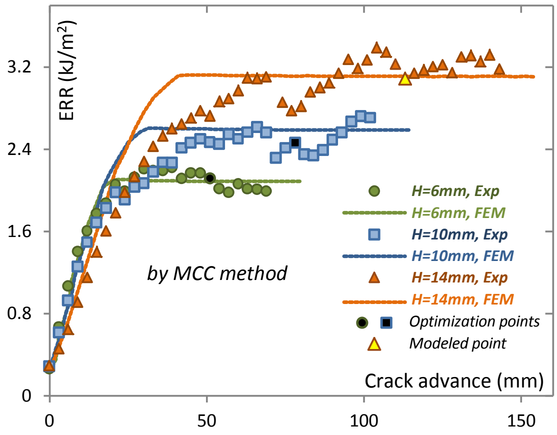

Fig. 5.12: Experimental R-curves compared to numerically predicted R-curves (see text for details).

Alternatively, R-curves can be formed starting from the initial fracture toughness and advance until the fully developed steady-state ($z_{\max}$, J_{total}) using the identified traction-separation relation as described in §4.3.5 and Eq. (4.1). The resulting R-curves, illustrated in Fig. 5.13, are compared with the experimental curves produced by the DCC method. With the exception of a zone around the transition to the steady-state, the predicted values are very close to the experimental results. Notably, the accuracy on the steady-state is increased using the segmented calibration being in agreement with the corresponding analysis for the thermoplastic matrix composite as analyzed in §4.3.5, given that a unique compliance calibrations, tends to underestimate the actual ERR.

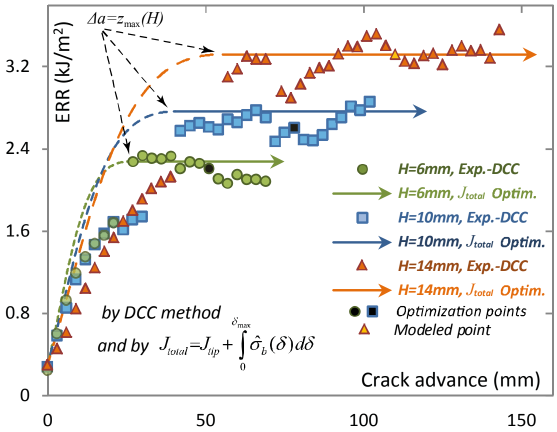

Fig. 5.13: Experimental R-curves using the DCC method and R-curves based on calculated traction-separation relations (see text for details).

5.4 Summary of key points

The main remarks of this section of the study can be summarized in the following:

- Experimental results demonstrate that intralaminar fracture toughening due to LSB, for this carbon/thermoset composite, is about 7.5 ($H=$6mm), 9.5 ($H=$10mm) and 11 ($H=$14mm) times greater compared to the fracture initiation value.
- The maximum ERR is significantly higher than the corresponding values in interlaminar fracture [14] as has been reported in previous works [17,85].
- The bridging zone length is smaller while, maximum bridging traction is 6 times larger compared with the corresponding values in interlaminar fracture [14].
- The maximum calculated bridging traction is thickness independent and equal to 8.3 MPa. This value is ~5 times smaller than the material's transverse strength.

- The corresponding maximum traction reported in previous works [15], as calculated using the direct method is significantly smaller for similar R-curves and this can be attributed to the uncertainties of the direct method.
- For the investigated thicknesses, the plateau values of ERR advance with steps of 20% per specimen thickness. These results, together with previous works [14,18] indicate a different approach on the treatment of R-curves in damage tolerant design with large scale bridging phenomena suggesting the importance of stiffness effects in fracture mechanisms.
- The implemented iterative, semi-experimental method provides very reliable results. This is evident since the cohesive element model, with the determined traction-separation relation, predicts the load-displacement curves very well and moreover, the calculated energetic contribution of bridging traction coincides with the R-curves with increased accuracy at the steady state.

5.5 Discussion on LSB contribution and ERR evolution

On the analysis of the toughening phenomena due to LSB, it is worth comparing the data on ERR at initiation and the contribution of bridging of intralaminar fracture of the same thickness of specimens of carbon/epoxy and the carbon/thermoplastic system reported herein. While the initiation values $G_{I,i}$ differ by a factor of almost 2 (~285 J/m^2 for carbon/epoxy and ~150 J/m^2 for AS4/PPS), the toughening contribution due to large scale bridging for the AS4/PPS composite is very close to the carbon/epoxy system i.e., ~2 - 2.2 kJ/m^2. The identified bridging parameters ($\sigma_{\max}, z_{\max}, \gamma$) are determined to be 4.13 MPa, 27.75 mm and 0.032 mm^{-1}, for the AS4/PPS and 8.19 MPa, 25.50 mm and 0.120 mm^{-1} for the carbon/epoxy. As a result, while the length of the bridging zone at steady state is the same, $\sigma_{\max}$ is the half in the AS4/PPS while γ is much larger. Thus, even though the maximum stress is lower, the different decreasing rates of the bridging tractions result in an equivalent bridging contribution in intralaminar fracture of the two composites.

Phenomenological observations imply that the competition between the failure of the bundles and the regeneration of new ones determines the extension of bridging and the magnitude of the closing tractions. Parametric studies using the reported numerical micromechanical model [66], shows that the interface strength (modeled by the connector elements) is the dominant parameter in intralaminar fracture under presence of LSB, while the initial fracture toughness and the tensile strength of the bundles appear to have very small effect. Nevertheless, interaction of properties/parameters is not investigated. The investigated thermoplastic system is characterized by ~25% lower tensile and compressive strength compared to the thermoset composite [104,105], which coupled with the lower initial toughness, appear to lead on quicker regeneration of the bridging ligaments. As a result, a composite system with low initial fracture toughness and relatively low tensile strength, demonstrates practically the same ultimate fracture resistance compared to a much stronger and initially tougher material.

Chapter 6

Intralaminar fracture of UD carbon/epoxy composite; ii) Pure Moment Configuration

6.1 Design of the test-rig

6.1.1 Loading concept

As it has been already mentioned in §2.6, in reality pure moment cannot be applied directly in any specimen. Thus, for this part of this study, a novel test-rig is designed, fabricated and used, capable of applying symmetric pure moments, on DCB specimens by means of pairs of forces. The working principle resembles the setup illustrated in Fig. 2.8(c) proposed by Lindhagen & Berglund [83], though the designed system is much more advanced from a machine design level. The drawing of the top view of the designed test-rig is shown in Fig. 6.1(a), including a dummy specimen and the forces' diagram. The designed testing setup can be mounted on a conventional universal testing machine, with the moment created and transferred by two sequential pairs of forces (see Fig. 6.1(a)). As a result the reaction moment per DCB arm, M, can be calculated as a function of the reaction load on the supports, F, and the imposed angle, θ, as described in Eq. (6.1).

$$\begin{gathered} M = \frac{F}{2} \cdot L \cdot \cos \theta/2 = F_A \cdot \ell = F_B \cdot \ell \Rightarrow \\ \Rightarrow F_A, F_B = F \cdot \cos \theta/2 \end{gathered} \tag{6.1}$$

In Eq. (6.1) the force, F_A represents the compressive force applied to each arm of the specimen via an aluminum roller, while, F_B, is the opening force applied via the stainless steel loading block. These two forces are assumed to be always normal to specimen's surfaces. The distances $L = 120$mm and $\ell = 60$mm, represent the two levers on which the two consequent pairs of forces are applied, as shown in Fig. 6.1(a).

6.1.2 Effects on loading points

Under the assumption that F_A may be as high as 800N, for the thickest specimen of the series ($H = 14$mm), the compressive roller is designed with an external diameter of 26mm. This diameter, coupled with the stiffness of aluminum, renders a maximum contact pressure of ~87 MPa and a contact width of ~1.2mm, assuming elastic contact with a span equal to the width of the specimen (according to Hertz theory of elastic contact [116]). This resulting maximum pressure provides a safety factor of ~1.6 with respect to the compressive strength of the epoxy. Thus, any effect of local failure and permanent deformation of the specimen on this region can be excluded.

In order to evaluate the effect of the pair of forces and define the domain within which the conditions applied are practically pure-moment, with such setup, three FE, 2D, plain strain models of the DCB specimens with the investigated thicknesses ($H = 6$, 10 & 14mm) are created. In these models, the roller and the block are also included with their precise geometry, while the loading arms of the test-rig are included with a "T-shape" rigid body element as illustrated in Fig. 6.1(b). The created model assumes perfect symmetry, with the applied boundary conditions also presented in Fig. 6.1(b). Moreover, the boundary between the roller and the specimen is modeled using frictionless, "hard" contact properties from the interaction module of Abaqus v6.12 [57], while the interface between the loading block and the specimen is considered perfectly bonded. In this FE model, a pair of forces is applied with such magnitude to create the necessary moment that corresponds to an ERR (Eq. (3.7)) $G_{PM}, J_{PM} = G_{I,i} =$ 285 J/m^2 equal with the initial intralaminar fracture toughness $G_{I,i}$ of the UD carbon/thermoset material (§5.3.6). The variable of this model is the length of the initial precrack, a_0, that varies from 60mm, being the minimum possible equal to the given ℓ, until 200mm depending on specimen thickness. The baseline G_{PM} or J_{PM} is compared with J_{tip} calculated using Abaqus v6.12 contour integral tool as described in §3.6.1 and APPENDIX I. The created models comprise 7,670-13,198 (depending on specimen's thickness) quadrilateral, quadratic, reduced integration plain strain elements (Abaqus CPE8R). The results of this analysis are illustrated in Fig. 6.2, and depict that after 10mm from the compressive load application point the applied loading conditions match perfectly the pure-moment assumptions. Thus, a precrack of 70mm length is considered sufficient. Furthermore, for relatively long crack lengths, corresponding to rotations above 15°, some error is induced due to large displacements as depicted in Fig. 6.2.

These two last described points determine the effects of local tractions on the region where the pure moment is applied. For this study special care is taken to eliminate these effects, avoiding, handy but rather coarse, grabbing fixtures that exist in the literature as summarized in Fig. 2.8. These effects escalate due to the composite nature of the investigated material, and are probably minor for the ceramic specimens tested in [82]. Additionally, in order to eliminate any torsion on the load application points induced by the tolerances in specimens and the bonding of the loading blocks, spherical plains bearing are employed to transfer the loads. Further details are found in Appendix IV.

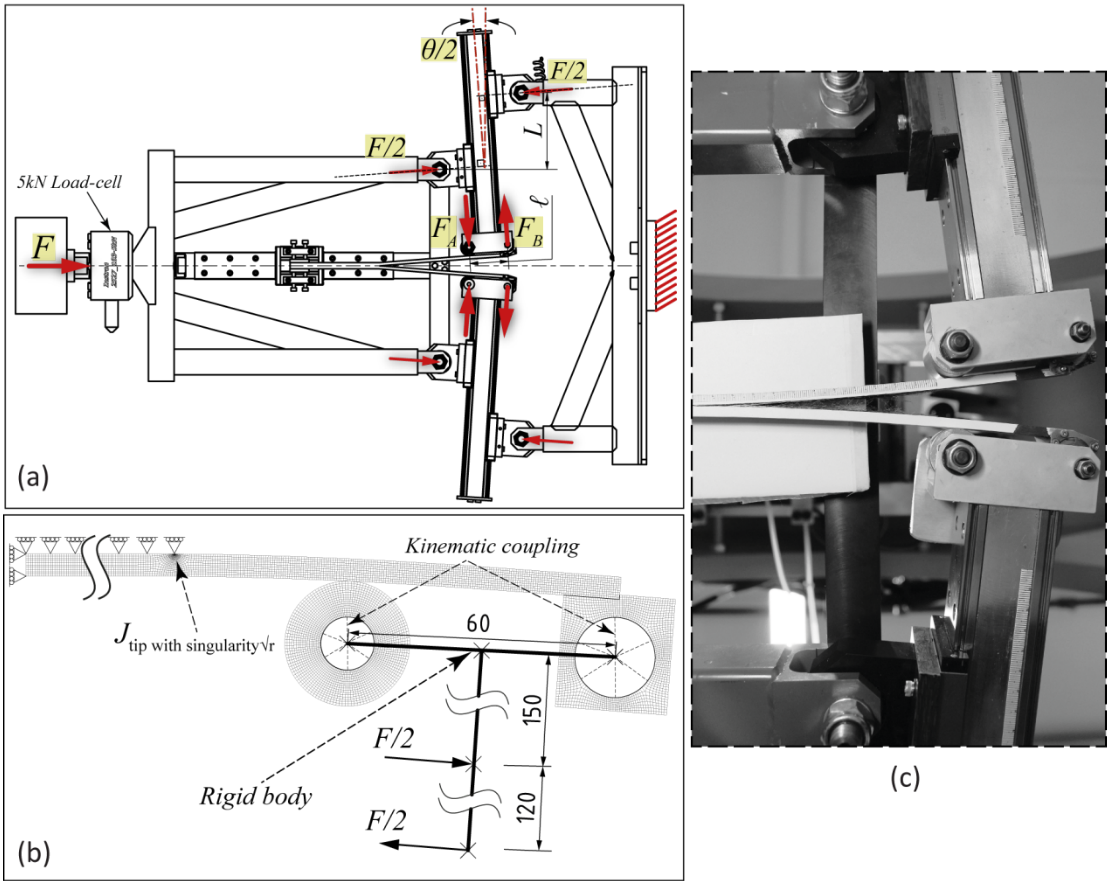

Fig. 6.1: (a) Pure moment test-rig configuration.

(b) Schematic of the numerical model with the DCB geometry employed to evaluate the design parameters.

(c) Photograph of an actual $H = 10$mm specimen at the end of the experiment.

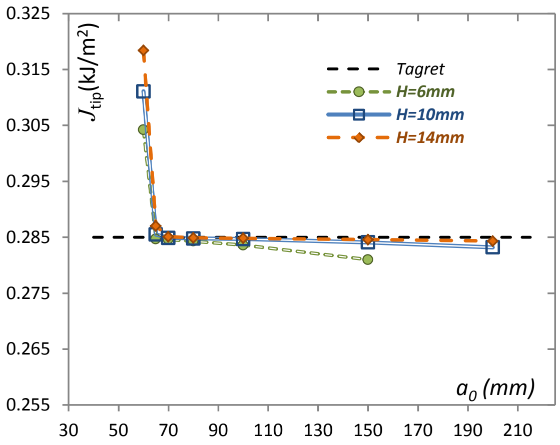

Fig. 6.2: Numerical calculation of J_{tip} *for different precrack lengths.*

6.1.3 Machine design and kinematics

The test-rig designed, as illustrated in Fig. 6.1(a), is actuated by the horizontal translation of a hydraulic cylinder. It comprises two main unequal frame-components, with a Π- shape and while the narrow one is moving along with the actuator, the wider one remain stationary throughout the experiment. These two partial frames are connected with each-other with four ball-bearings (2 normal and 2 self-aligning), mounted on the carriages of four linear bearings (see Appendix IV). Each couple of linear bearings is assembled to form a sandwich beam that leads to a fork-shape mounting for each specimen arm. With this configuration, a geometrically defined rotation angle is imposed to the specimen, while the rails of the linear bearings are allowed to move depending on the stiffness of the tested specimen. A photograph of the key-region of the setup with a mounted specimen, at the end of an experiment, is shown in Fig. 6.1(b). The whole setup is mounted normal to the direction of gravity, as depicted in the drawing of Fig. 6.4(a), to avoid any changes of the loading conditions during the translation of the moving parts.

The initial rotational friction resistance of the ball bearings is trivial, while the initial friction per mounted linear bearing arm, mainly due to the protective seals, is ~1.5N as measured directly by a Newton-meter. Moreover, the chosen linear bearings are from a miniature guidance series with no preloading and a rolling friction coefficient $\mu \simeq 0.005$, provided by the manufacturer and this value is confirmed by an inclination test. As a result the energy dissipated due to friction is expected to be insignificant compared to the strain energy and the fracture energy of the experiment.

An additional linear bearing is mounted uniaxially to the actuation's direction and is employed to prevent any deviation of the specimen from the axis of symmetry that could be induced by the slightest misalignment or any potential unevenness of LSB, since the existing frictional forces are insignificant. To avoid local damage of the specimen, aluminum spacers are bonded on the end of the specimen (Fig. 6.3).

The overall test-rig is designed using Autodesk® Inventor 2014, and all designed components are virtually assembled in a functional manner, in order to create a kinematic CAD model of the designed setup, to predict the relationship between the induced linear translation of the hydraulic cylinder and the resulted angle on the specimen.

6.2 Materials and specimens

For this part of this study, initially, two remaining specimens (SP1 and SP2, -PM-) of $H = 10$mm of batch #2 as described in §5.1 are notched with the diamond wire saw, to introduce a 70mm intralaminar precrack and are consequently tested with the PM test-rig configuration. All specimens are painted with white paint and subsequently a fine ruler is bonded, as exactly described in §3.1. Moreover, SP2-PM is painted white in both sides with the second one being marked with a random speckle pattern introduced with a black spray paint (see Fig. 6.3). This procedure serves the DIC measurements as explained in the following paragraph (§6.3).

In the PM test-rig the opening forces (from the pair of forces) are applied by means of glued loading blocks. However, the local forces are expected to be much higher than the EOF case. For this reason special stainless-steel loading blocks are designed and machined, with such geometry to maximize the adhered surface with the composite specimens, while the load application-point is shifted, so as to reduce the neutral part of the specimen used only for load transferring. Some schematics and photos containing the details of the loading block configuration are included in Fig. 6.1(b) & Fig. 6.3, while a drawing is included in Appendix IV. The loading blocks are glued to the specimens with the same 5 min epoxy used in the series of experiments presented in §5.1, and moreover, in order to obtain maximum bonding strength, the prepared specimens are post-cured for 5 hours in 50°C. For the thicker specimens, where loads as high as approximately 800N are expected, two additional stainless steel plates are fastened to both loading block and specimen, to assure effective load transfer, as depicted in Fig. 6.3.

Moreover, a new batch (#3) of material-plate and specimens are fabricated using the alike autoclave procedures as described in §5.1, from the same material carbon/thermoset prepreg material (Gurit SP™) originating though from a newer production series (#1, #2 fabricated in 2014 and #3 in 2016). The cured plate has a thickness of 10±0.1 mm, which represents the width, B. From this plate (#3), 9 specimens are tested in total, three of each investigated thickness ($H=6$, 10 & 14 mm, tolerance: 0 to +0.1mm).

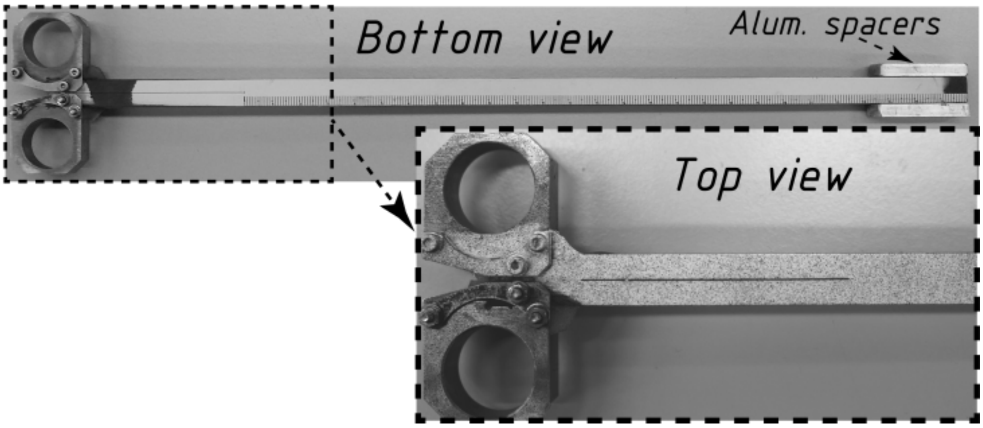

Fig. 6.3: Typical specimen with speckle pattern, ready to test ($H = 10$mm).

6.3 Fracture testing

The constructed PM test-rig is mounted on the horizontal axis of an Instron® biaxial cruciform testing machine (Fig. 6.4(a)) and the total reaction load F, is measured by means of a 5kN load-cell while the translation of the actuator is monitored by the built-in LVDT with a frequency of 50Hz. This frequency is considerably high for a quasi-static experiment because there is a necessity of noise rejection, due to waves introduced by the hydraulic pulses of the servo-valve's actuation. All experiments are conducted at room temperature.

Using the CAD kinematic model and the built-in iLogic programming tool in Autodesk® Inventor 2014, the relation between the horizontal translation and the imposed angle is extracted, since analytic trigonometry cannot be used due to the complexity of the system. Nevertheless, to increase the accuracy in the angle measurement, an angular position sensor (Vert-X 28 from Contelec, Biel-Switzerland) is employed (see detail in Fig. 6.4(a)). The signal of this sensor is monitored by an Arduino™-Uno microcontroller extended by a 16-bit analog to digital converter (ADS1115), to increase the recording resolution. This configuration provides an angle measuring setup with ~0.1° resolution and repeatability, while the acquired data are recorded with a 20Hz frequency using a Matlab® script. A comparison of the recorded angle, with the expected angle based on the cross-head displacement measurements and the CAD model, are presented in Fig. 6.4(b). These two sets of data are in an almost perfect agreement, demonstrating the efficiency of the kinematic CAD model and moreover demonstrate that the designed setup is sufficiently rigid.

In summary, the angle θ is evaluated by the measurements of the angular sensor which are synchronized with the reaction moment M measurements, calculated from the reaction load F, as described in Eq. (6.1). All experiments under PM conditions, are conducted in cross-head displacement control (i.e. θ- control), with a constant rate of 3mm/min, chosen to result in an equivalent crack propagation speed with the EOF series of experiments.

In all specimens the crack tip location is monitored by the same CCD camera used in the EOF series of experiments. Moreover, in order to evaluate the ERR using the $J_{total}^{(\theta_1,\theta_2)}$ (Eq. (3.8)), in SP2-PM, the relative angles θ_1, θ_2 of the two DCB arms, at the loading points are evaluated using the displacement field measured employing the DIC technique. In this technique the commercial software VIC-2D™, from Correlated Solutions Inc. is used to extract the relative opening displacements at the neutral axes of the DCB arms. The measured displacements are initially smoothened with the local regression algorithm "rloess" of Matlab®, before calculating the rotations by finite differences. Pertinent photographs for the DIC analysis are acquired by a color, very high resolution (2048 x 1536), CCD camera, mounted above the loads' application point, following the motion of the linear bearings. One representative photograph of the testing configuration at the end of an experiment is included in Appendix IV.

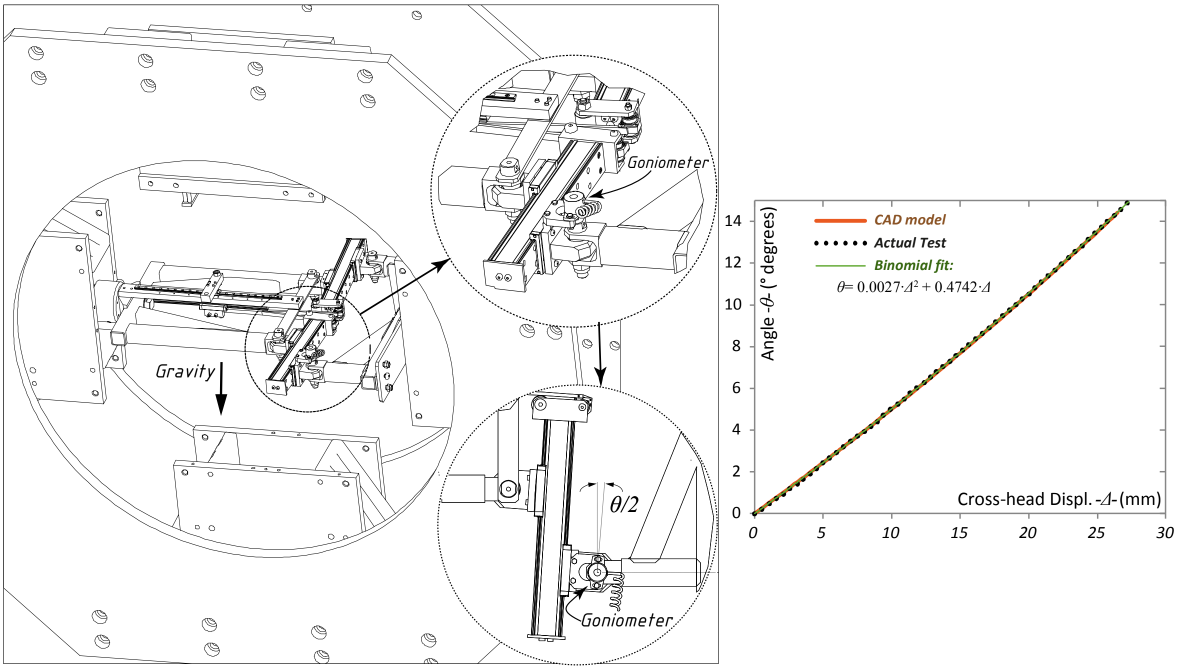
Goniometer
Gravity
θ/2
Goniometer
CAD model
Actual Test
Binomial fit:
θ= 0.0027·Δ² + 0.4742·Δ
Angle -θ- (° degrees)
Cross-head Displ. -Δ-(mm)
0
2
4
6
8
10
12
14
0
5
10
15
20
25
30

(a) (b)

*Fig. 6.4: (a) Drawing of the pure moment test rig and detail of the goniometer.
(b) Comparison of the actual measured angle with the one acquired
from the kinematic model by the CAD.*

6.4 Evaluation of ERRs

For the production of the intralaminar mode I R-curves using the PM configuration, three different methods are employed and evaluated:

(i) The most convenient way of constructing the R-curves is by using only the measured M for a given crack advance Δa, using Eq. (3.7) with the ERR denoted as $J_{total,PM}$. For this approach the material properties E_z and $\nu_{zx} \cdot \nu_{xz}$ are employed, along with the thickness of the specimen as an effective value, $\bar{h}$, accounting for the thickness reduction at the pre-cracked region (see Fig. 6.5(b)). This approach though, may lead to imprecise results, due to the simplifications made to obtain Eq. (3.7).

(ii) Alternatively, R-curves are produced using M, θ and Δa in a compliance calibration scheme, similar to Eq. (3.2) that can be defined as follows:

$$G_{total,PM} = G_{I,i} + G_{i,b} = \frac{M^2}{2B}\frac{\partial C_M}{\partial a},\ C_M = \theta / M \qquad (6.2)$$

Here, the experimentally calculated compliance $C_M(a)$, can be fitted with a linear function as: $C_M(a) = \Re a \Rightarrow \frac{\partial C_M}{\partial a} = \Re$, which is practically an experimental evaluation of the constant part in Eq. (3.7), instead of considering the elastic solution as $\Re = 24(1-\nu_{zx}\nu_{xz})/Bh^3E_z$. To account for the effect of LSB phenomena a quadratic binomial fitting function is used, aiming in increasing the accuracy of the fitting scheme formed as:

$$C_M(a) = \Re a^2 + ma \Rightarrow \frac{\partial C_M}{\partial a} = 2\Re a + m \qquad (6.3)$$

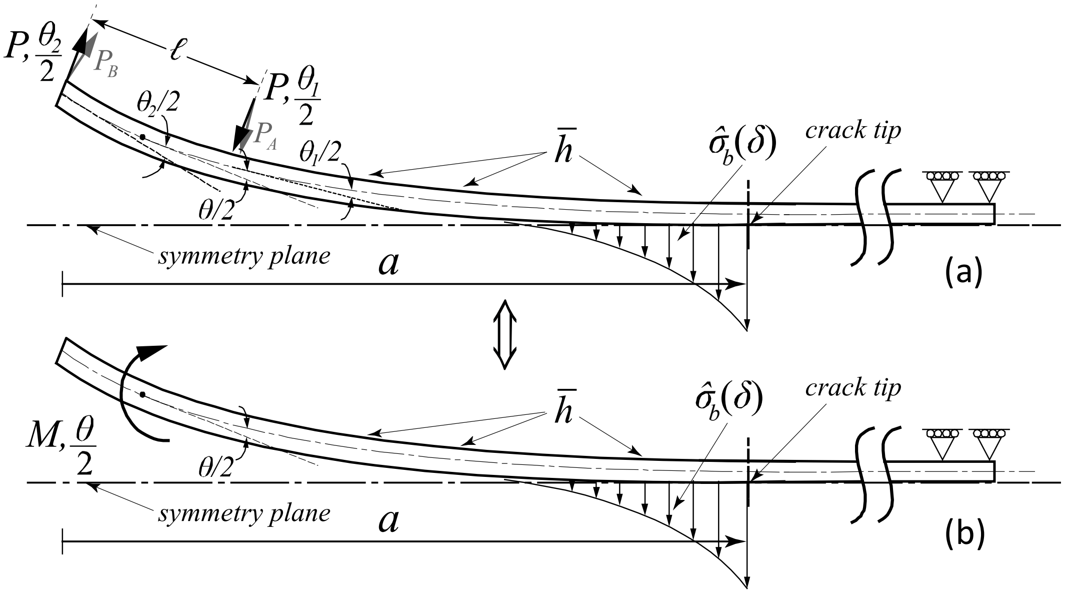

$P,\frac{\theta_2}{2}$
P_B
ℓ
$P,\frac{\theta_1}{2}$
$\theta_2/2$
P_A
$\theta_1/2$
$\bar{h}$
$\hat{\sigma}_b(\delta)$
crack tip
$\theta/2$
symmetry plane
a
(a)
$\bar{h}$
$\hat{\sigma}_b(\delta)$
crack tip
$M,\frac{\theta}{2}$
$\theta/2$
symmetry plane
a
(b)

Fig. 6.5: (a) Specimen's force diagram. (b) Equivalent moment diagram.

(iii) Finally, a more experimentally elaborate scheme is used, employing the experimentally measured angles θ_1, θ_2 and the applied loads $|F_A| = |F_B| = P$ to obtain $J^{(\theta_1,\theta_2)}_{total,PM}$ Eq. (3.8) (see also definitions in Fig. 6.1(a) and Fig. 6.5(a)). This approach has the advantage of being produced using the least possible approximations, similar to $J^{(\theta)}_{total}$ for the EOF case (Eq. (3.6)). Nevertheless, this method is more sensitive to the experimental errors as it is based on the difference of two small quantities ($\theta_1 - \theta_2$) which can be demonstrated by calculating the relative errors for $J^{(\theta)}_{total,EOFs}$ and $J^{(\theta_1,\theta_2)}_{total,PM}$ using the total differential as:

$$\frac{d\left(J^{(\theta)}_{total,EOFs}\right)}{J^{(\theta)}_{total,EOFs}} = \frac{\theta dP + Pd\theta}{P\theta}$$

and (6.4)

$$\frac{d\left(J^{(\theta_1,\theta_2)}_{total,PM}\right)}{J^{(\theta_1,\theta_2)}_{total,PM}} = \frac{(\theta_2-\theta_1)dP + 2Pd\bar{\theta}}{P(\theta_2-\theta_1)},\ d\bar{\theta} = d\theta_2 = d\theta_1$$

In the calculation $J^{(\theta_1,\theta_2)}_{total,PM}$ (Eq. (3.8)) it has been assumed that the pair of forces P are equal to normal forces on the specimens P_A, P_B (see Fig. 6.5(a)) since the $\cos(\theta_2-\theta)$ and $\cos(\theta-\theta_1)$ for the measured angles are greater than 0.995. Thus, $J^{(\theta_1,\theta_2)}_{total,PM}$ is approximated as:

$$\Rightarrow J^{(\theta_1,\theta_2)}_{total,PM} = \frac{P_B\theta_2 - P_A\theta_1}{B} \simeq \frac{P(\theta_2-\theta_1)}{B} \qquad (6.5)$$

The angles θ_1, θ_2, as already stated, are measured using the DIC technique. However, the option of using the deflection equations based on Beam Theory was initially investigated. For this part, a beam as illustrated in Fig. 6.5(a) is considered, and for increasing the accuracy, the measured intermediate angle θ, is taken as the reference, instead of the load P. Additionally, provided that the corresponding Beam Theory case incorporates no rotations at the crack tip location (Fig. 6.5(a)), a correction for the crack length is adopted as described in [90], with the corrected crack length being: $a' = a + xh$ (see also Eq. (3.3)). With all the described assumptions θ_1 & θ_2 are given by:

$$\theta_1 = \frac{a'-\ell}{a'-5\ell/8}\cdot\theta \quad \& \quad \theta_2 = \frac{2a'-\ell}{2a'-5\ell/4}\cdot\theta \qquad (6.6)$$

As explained later, this approach is not providing precise enough values and as a result only the results from the DIC are considered.

6.5 Preliminary analysis and estimated results

One of the objectives of this study is to investigate whether a traction-separation relation identified with a particular mode I loading condition, is also valid for the other mode I loading cases. To examine this, it is initially assumed that the traction-separation relation is unique. Thus, a numerical model of a DCB specimen with $H=$ 10mm is created, introducing a cohesive element zone, at the symmetry plane (as described in §3.6.2), with properties corresponding to the identified $\hat{\sigma}_b(\delta)$, for the EOF loading condition (§5.3.4 and Fig. 5.7). Nevertheless, in this model, the implemented boundary conditions correspond to the pure moment case and are analogous to the loading conditions implemented in the designed experimental setup. The results of this analysis are shown in Fig. 6.6(b), while Fig. 6.6(a) illustrates the FE model, with the calculated longitudinal stress-field and the boundary conditions indicated. From the recorded stress profile, it is visible that the conditions, almost right after compressive load's application point, are matching perfectly the pure-moment stress-state as illustrated in Fig. 2.7(b), even though closing tractions exist via the cohesive elements. In Fig. 6.6(b) are shown, numerical R-curves created using the resulted M, θ and Δa in a compliance calibration scheme (Eq. (6.2) and (6.3)), the $J_{total,PM}$ as in Eq. (3.7), and $J_{total,PM}^{(\theta_1,\theta_2)}$ as in Eq. (3.8). The depicted difference between these three approaches does not exceed ±2%,. Moreover, the calculated R-curves for this cohesive numerical model under PM, are compared with corresponding ERR estimation using the direct integration of the identified cohesive law, for the EOF loading condition, denoted as $J_{total}(\hat{\sigma}_b(\delta))_{EOFs}$ (Eq. (4.1)) and the maximum ERR at the steady-state is almost in perfect agreement with $J_{total,PM}^{(\theta_1,\theta_2)}$. Consequently, the $J_{total,PM}^{(\theta_1,\theta_2)}$ calculations are proven to be the most accurate of the three approaches, as expected (see §3.2.3), provided that the potential error as described by Eq. (6.4), is very low since no experimental data are employed here. Nevertheless, some small difference on the shape of the R-curves of PM vs. EOF is present, as expected, given that the pure-moment conditions result to invariant stress-state all along the crack path.

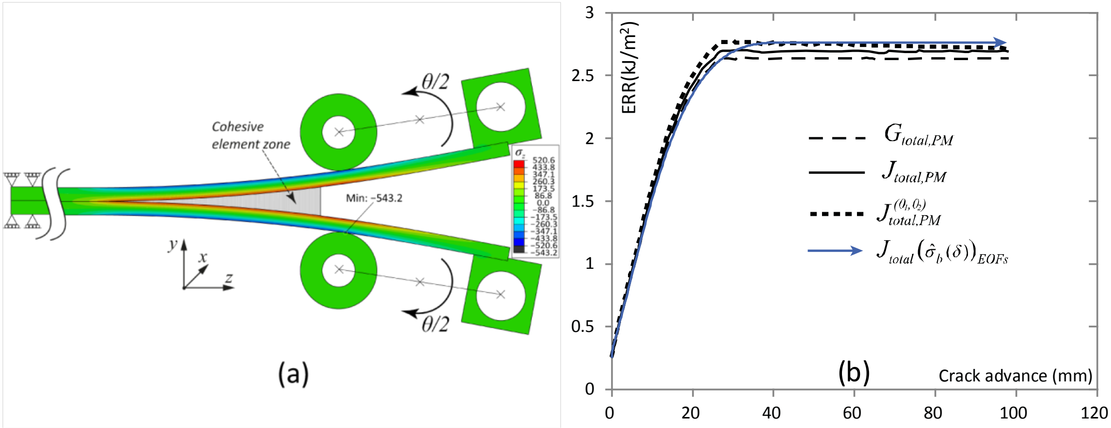

Fig. 6.6: (a) Snapshot of the FE model, with σ_z *results and boundary conditions indicated.*
(b) R-curves based on the response of the cohesive element model, with the pure moment conditions and corresponding response from the EOF identification ($H = 10$*mm)*

6.6 Results of batch #2

The R-curves of the two tested specimens from batch #2, created using the described CC scheme for the PM case, as described in Eq. (6.2) and (6.3), are displayed in Fig. 6.7(a) and compared with the corresponding mean response from the EOF experiments using the MCC method, for the same thickness ($H = 10$mm). Moreover, the ERR at the steady-state is included in this plot, identified using the inverse identification by $J_{total-SS}$ (Eq. (3.12)). The data in Fig. 6.7(a) show that the shape of the calculated R-curves for the PM experiments is slightly different, and the estimated ERR at the steady-state is ~8-10% higher than the corresponding values from the EOF experiment. However, this difference is in the same order with the underestimation related with the MCC method as reported in §4.3.5 and §5.3.6. Hence, the calculated ERRs practically coincide with the corresponding estimation from the inverse identification scheme. In addition, the quality of the compliance calibration fitting scheme used for the PM case is superior to the MCC method, since it involves a polynomial, one degree higher that the expected simple case.

A photograph of a fractured specimen from the PM experiment is illustrated in displayed in Fig. 6.7(b). Remarkably, the depicted bridging phenomena resemble the corresponding ones from the EOF case (Fig. 5.2).

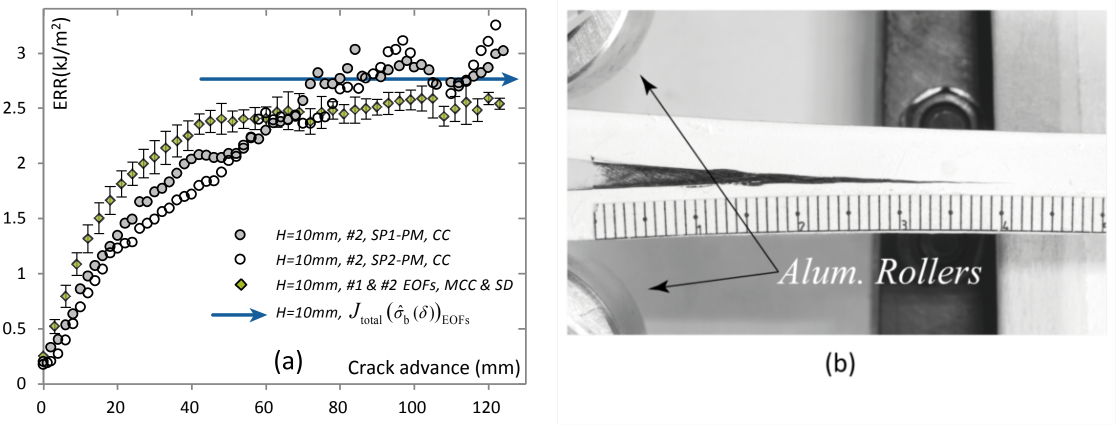

Fig. 6.7: (a) Experimental R-curves batch #2, PM by CC and EOF by MCC, and identified $J_{total-SS}$ *in EOF. (b) Photograph of specimen during fracture test (* $H = 10$*mm).*

As it is already mentioned in §6.3, the DIC technique is used in SP2-PM, to measure the angles θ_1 and θ_2 to calculate the ERR using $J_{total,PM}^{(\theta_1,\theta_2)}$ (Eq. (6.5)). The experimental angles are compared with the simplified prediction using the Beam Theory (see Eq. (6.6)) in Fig. 6.8(a). This comparison demonstrates that this simplified approach has an error of 5-10% with respect to the experimental values, however the error in the difference of the two angles $\left(\theta_2 - \theta_1\right)$ is much higher (~25%). For this reason $J_{total,PM}^{(\theta_1,\theta_2)}$ is only evaluated for SP2-PM, in which the curvature of the arms is experimentally measured using DIC. A typical photograph used in DIC to measure the curvature of the specimen is illustrated in Fig. 6.8(b).

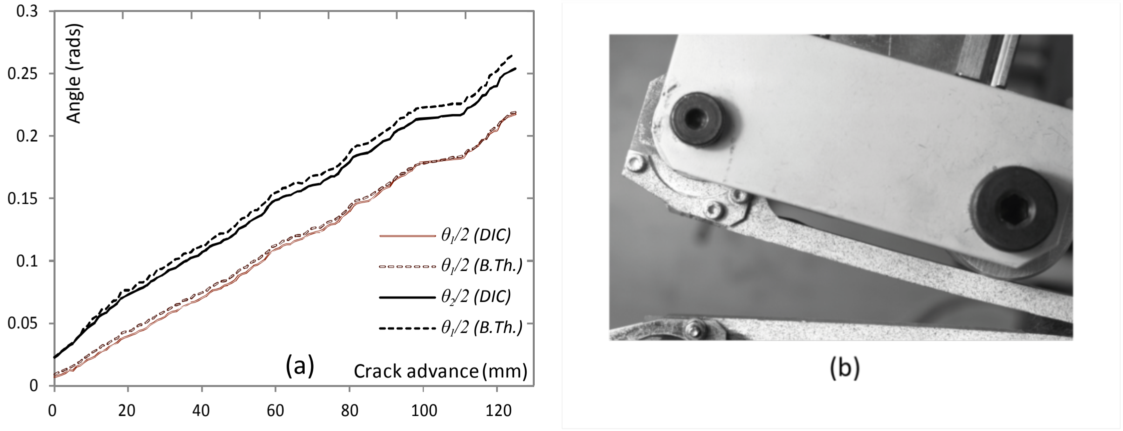

Fig. 6.8: (a) Measured angles from DIC vs. estimation using Beam Theory.
(a) Typical photograph used in DIC to measure the curvature of the specimen.

The R-curves of SP2-PM with all three described approaches (Eq. (3.7), Eq. (6.5), Eq. (6.2) & (6.3)) are displayed in Fig. 6.9. As it is previously explained, the evaluation of an R-curve using $J_{total,PM}^{(\theta_1,\theta_2)}$, is expected to be the most accurate among the described approaches (see §3.2.3), when reliable rotation measurements are obtained. Remarkably, the three employed approaches, on one unique specimen, provide three different R-curves. The plateau state of the compliance calibration scheme and the ERR calculated using the measured rotations, result almost to the same values with a variation of ±7%. The rising part of the CC scheme, underestimates the expected ERR, based on $J_{total,PM}^{(\theta_1,\theta_2)}$, which is attributed to the weakness of the fitting scheme to follow precisely the transitional part as is it is thoroughly explained in §3.2.1.

The initial rising part of $J_{total,PM}^{(\theta_1,\theta_2)}$, for a crack advance of up to 20mm, is in perfect agreement, with the simplistic calculation of J-integral described in Eq. (3.7), however, after some crack advance, the later approach diverges significantly from the other two, with a maximum deviation higher than 35% at the steady-state crack propagation. The region of divergence corresponds to a domain where LSB starts having a very dominant effect.

J-integral as described in Eq. (3.7), is formed using equations from elasticity theory, being a function of E_z, h^3 and M^2. The latter is the only experimental value required from the fracture test. Therefore, any deviation from the elastic assumption considered, in the relation of stresses and strains would provide significant error, while it is very sensitive to E_z and h. For this reason, h is measured with precision along the tested arms and it is corrected with an effective value, $\bar{h}$, accounting also for the thickness reduction at the pre-cracked region as displayed in Fig. 6.5; nevertheless this correction has an effect of maximum 3%.

A significant number of works (see [117] and references therein), report different experimental values of the normal modulus in fibers' direction for UD composites, depending on whether they are measured by tensile, compressive or flexural experiments. The reported deviations [117], can be as high as 20%. This behavior can be attributed to the experimental methods, the waviness of the fibers and/or fiber micro-buckling. The elastic modulus E_z, for this study, is measured experimentally with a 4-point bending experiment as described in §5.1, following the directions in [111] for highly orthotropic material. The measured $E_z =$118.7 GPa, corresponds to $\varepsilon_z <$0.23%, whereas the strains in the steady-state of the PM experiment are expected to be in the range of 0.44% which may also have some influence on the effective modulus of the DCB specimen. In any case, the J-integral in Eq. (3.7) requires precise information of E_z, which can be significantly affected by all the aforementioned particularities.

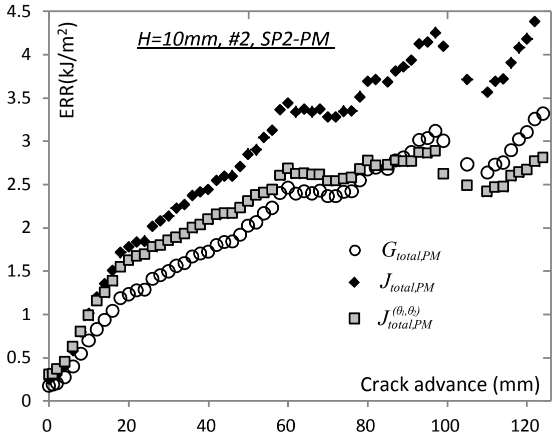

Fig. 6.9: Experimental R-curves, by CC, $J_{total-PM}$ *and* $J^{(\theta_1,\theta_2)}_{total,PM}$

Independent, investigation on the LSB phenomena under PM conditions, employing the embedded cell approach described in §3.6.3 and [66,67], is conducted at LMAF by Dr. L. Canal. The created numerical micromechanical model, comprises the fiber-bundle profile used in [66], that practically corresponds to the tested specimens of batch #1 and #2, while the interfaces between fiber-bundle and homogenized-composite are modeled using cohesive elements (see §3.6.2) allowing for local mixed mode failure, that follows the initial toughness properties reported in [29]. The boundary conditions of this model are equivalent to ones displayed in Fig. 6.6(a).

The moment-rotation response of this model is shown in Fig. 6.10(a), compared with the results from the two PM experiments from batch #2 and the FE model which employs the traction-separation relation identified from the EOF case, in a cohesive element zone as described in §5.3.4 and §5.3.5. Here, it is observed that the shape of the $M-\theta$, response of the micromechanical model and the experiments are in good agreement. At this point it should be noted that, the micromechanical model, shows a more rigid response due to the presence of the fiber-bundles which are superimposed to the homogeneous sections and would correspond to a DCB with equivalent arms of $h_{MM} \simeq$ 5.3mm. Note also that, the linear part of the $M-\theta$ responses finishes at $\theta/2 \simeq$ 1.2°. On the other hand, the response predicted using the identified tractions separation relations from the EOFs has a slightly different shape, especially towards the steady-state, although the measured ERR are very close with the experimental values (see Fig. 6.7(a)). This is attributed to discreteness of the bridging fiber bundles, which are meticulously included in the micromechanical model, while in the cohesive element model is included only a homogenized version of the closing tractions of the bridging fiber-bundles.

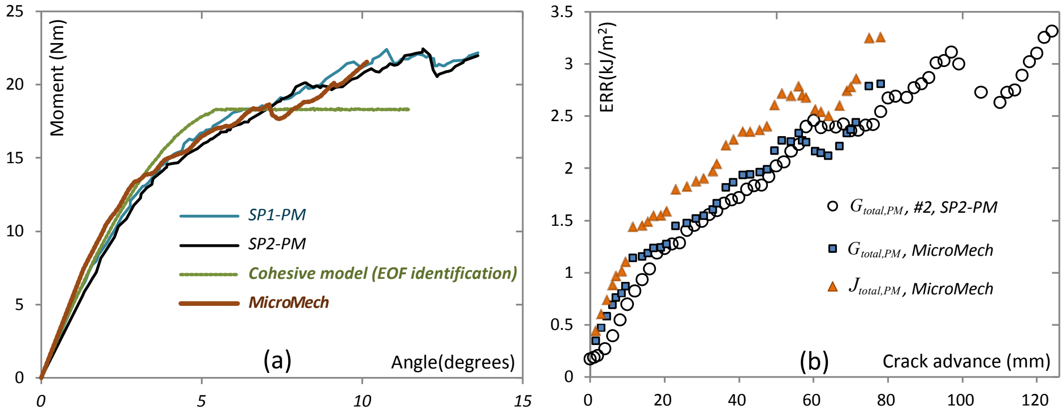

Fig. 6.10: (a) Moment – angle ($\theta/2$) response, experiments, cohesive and micromechanical model; see text for details.

(b) Experimental R-curves, SP2- PM-#2, by CC, compared with R-curves from micromechanical model.

The corresponding R-curves from the micromechanical model, constructed using the CC method (Eq. (6.2) & (6.3)) and the J-integral described in Eq. (3.7), compared with the experimental values from SP2-PM, are illustrated in Fig. 6.10(b). Here, experiment and micromechanical model are in very good agreement, considering the CC method as reference, however, some overestimation is observed on the values from the J-integral as described in Eq. (3.7). In the micromechanical model the difference between $G_{total-PM}$ and $J_{total-PM}$ practically vanishes, after considering the aforementioned corrected thickness h_{MM}, in Eq. (3.7) as displayed in Fig. 6.11.

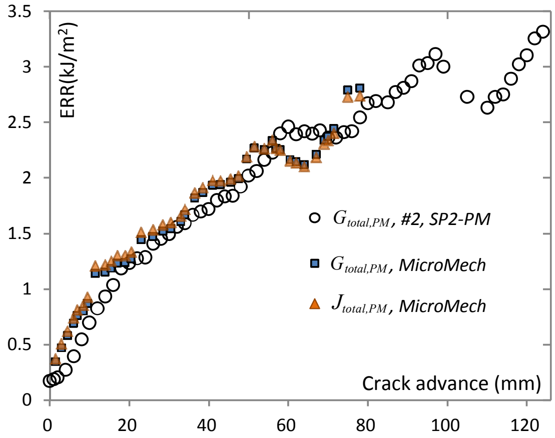

Fig. 6.11: Experimental R-curves, SP2- PM-#2, by CC, compared with R-curves from micromechanical model (modified); see text for details.

In summary, the traction-separation relations identified from the EOF case, appear to have minimal difference with the ones expected for the PM configuration, since the measure ERRs at the steady state are very close. Moreover, calculation of experimental R-curves for the PM configuration, using Eq. (3.7), can result to questionable values very sensitive to the employed magnitude of E_z modulus and any possible variations in thickness.

On the other hand, a well-defined CC scheme can provide more reliable results, when $J_{total,PM}^{(\theta_1,\theta_2)}$ cannot be evaluated. Nevertheless, LSB phenomena of the depicted scale render a non-trivial characterization procedure.

6.7 Results of batch #3 and discussion

The $M-\theta$ response, of the 9 tested specimens from batch #3 of all investigated thicknesses, is shown in Fig. 6.12(a). The depicted experimental scatter is in the same range with all the already reported experiments in intralaminar fracture (§4 and §5), which is attributed to the extent of the formed LSB. Some minor scatter is observed in the liner-response region, originating from the small variation on specimen’s initial dimensions. The $M-\theta$ response and crack propagation data are employed in a CC scheme as described in Eq. (6.2) and (6.3) to produce the R-curves. Having demonstrated in the previous paragraphs that the CC method provides ERR calculations with reasonable accuracy, only this scheme is employed in this series of experiments. The resulted mean R-curves for all specimens are shown in Fig. 6.12(b) and the included error bars depict the maximum and minimum measured value per crack advance.

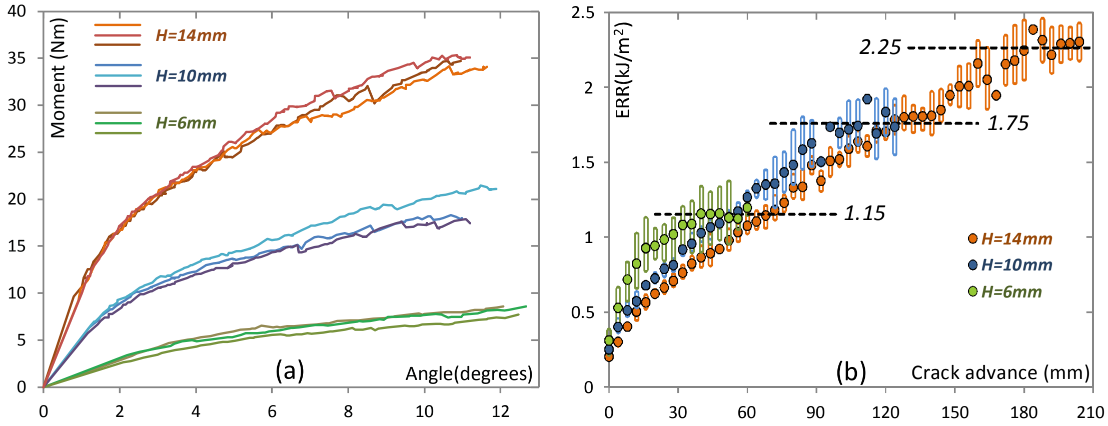

Fig. 6.12: (a) Moment – angle ($\theta/2$) response, experiments from batch #3.

(b) Experimental R-curves by CC, per specimen thickness; batch #3.

A clear thickness effect is present on the illustrated R-curves, and the maximum-plateau value advances with steps of 40-20% per specimen thickness. These results follow the trends reported in §5 and the ones of previous works [14,18]. Moreover, a clear effect on the extent of the bridging zone and on the slope of the R-curves are depicted, with the thicker specimens to require a longer crack extension to attain steady-state crack growth, as also reported in the literature [8,9,10,15].

The R-curves illustrated in Fig. 6.12(b), provide entirely different maximum ERR values for the steady-state compared with the ones form batches #1 and #2 shown in Fig. 6.7 and Fig. 5.11-Fig. 5.13. Nonetheless, the tested specimens, from all three fabricated plates, comprise the same constituents in equivalent volume-fractions, attested also by their bending response. This calculated variation in the maximum ERR values is attributed to the different extents of the formed LSB. This behavior is depicted in the recorded fracture profiles which are illustrated in Fig. 6.13, corresponding to two specimens with thickness $H = 10$mm, both tested in PM conditions, originating though from batch #2 and #3. These profiles are acquired using a digital-optical microscope. The height-magnitude of the recorded profiles may not correspond to the exact thickness of the bridging bundles, since many bundles are totally pulled out from the composite. However, the difference of the fracture profile is representative of the fiber-bundle density. Also illustrated in this figure are the fractured surfaces employed in the acquisition of the profiles. Here, judging mainly by the wavelength of the recorded fracture profile, it is observed that the size of the largest formed fiber-bundles appears similar in both specimens. However, the density of the formed bundles in #2 is much higher than the corresponding one from #3 and this is reflected to the measured ERRs.

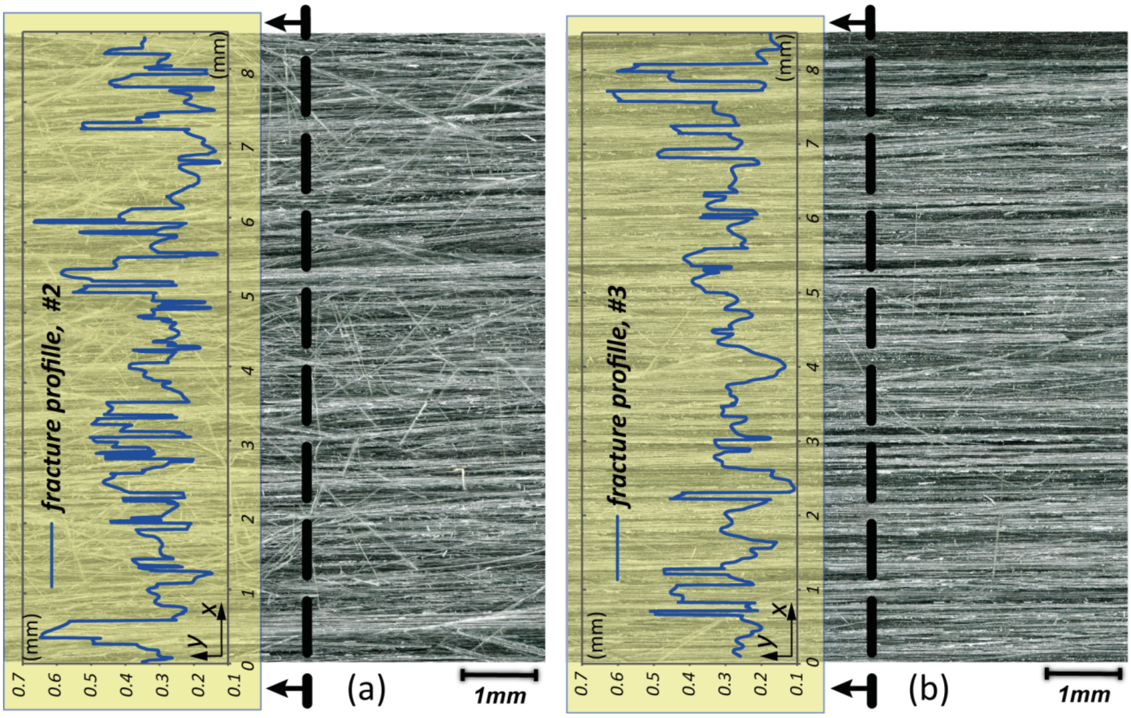
fracture profile, #2
(mm)
0
1
2
3
4
5
6
7
8
(mm)
0.7
0.6
0.5
0.4
0.3
0.2
0.1
x
y
(a)
1mm
fracture profile, #3
(mm)
0
1
2
3
4
5
6
7
8
(mm)
0.7
0.6
0.5
0.4
0.3
0.2
0.1
x
y
(b)
1mm

Fig. 6.13: Fractured surfaces and recorded profile of specimens tested in PM ($H = 10$mm);
(a) DCB from batch #2. (b) DCB from batch #3.

An explanation to the different behaviors can be given by observing the cross-sections, of the two specimens shown in Fig. 6.13. These cross-sections are displayed in Fig. 6.14 with the orientation of the potential crack-plane indicated. These cross-sections reveal different fiber-clustering and dissimilar interlaminar reach resin zones, rendering though to similar volume fractions. The origin of the variation in the microstructure is unknown and it could be attributed to alternation of the fiber spreading or resin impregnation parameters and apparatus, by the manufacturer. Thus, from this qualitative analysis, it can be assumed that the more homogeneous and random the fiber clustering in the composite, the higher the extent of the LSB phenomena.

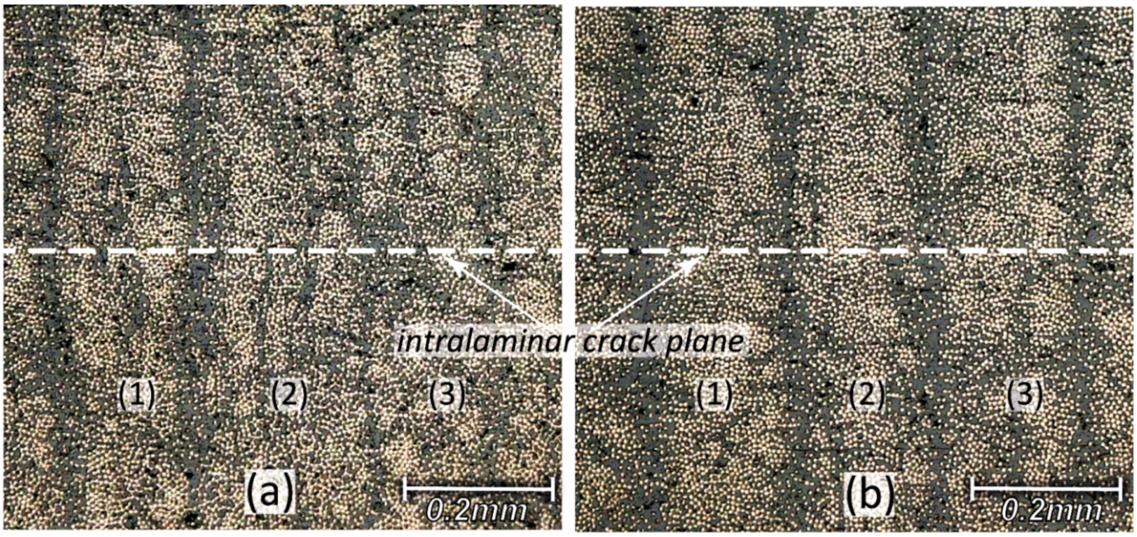
intralaminar crack plane
(1)
(2)
(3)
(a)
0.2mm
(1)
(2)
(3)
(b)
0.2mm

Fig. 6.14: Cross-section views from specimens tested in PM ($H = 10$mm);
(a) DCB from batch #2. (b) DCB from batch #3.

Chapter 7

Traction-separation relations in delamination of a tufted GFRP composite

Tufting is a method to enhance fracture resistance in woven FRP composite materials. In fact, this is achieved by the bridging tractions exerted by the tufts on the wake of the crack propagation between adjacent layers of the composite.

In this chapter, identification of the traction-separation relation is carried out on a tufted, layered fabric GFRP composite. Extensive experimental work has been carried out at LMAF and LPAC (Prof. V. Michaud, EPFL) in the framework of the sabbatical stay of Prof. S. Joncas (ÉTS, Montréal), dealing with the interlaminar fracture characterization in tufted composites and the effects of tuft geometry and surface density. In this chapter, modeling of the bridging phenomena is addressed based on the methods developed in the previous chapters.

7.1 Materials and specimens

7.1.1 Material fabrication and elastic properties

In the previous sections of this thesis, results of studies in fracture of UD laminated composite materials, are described. For this part, a GFRP layered, woven composite material is investigated. The material consists of 30 cross-ply (0/90) twill 2/2, fabric plies, of E-glass fibers, produced by Texonic Inc. (Québec, Canada). In particular regions, the plies are tufted together by CTT GROUP (Québec, Canada), with carbon-fiber filament yarns (Tenax® HTA40 F15 1K 67tex 15S) with a square pattern of 5mm spacing (hereafter refer to as 5-SQ). The fabricated preforms are infused in-house, under vacuum conditions, with an Araldite® 8615, two component epoxy system. The composite is initially cured at 40°C for 24h and later post-cured at 180°C for 3h. With this technique plates with a surface of 600 × 400 mm^2 are fabricated. The single plate used herein, is designed to accommodate specimens for material moduli and strength characterization as well as, for DCB delamination testing of both tufted and neat GFRP. The cured plate has a thickness of 7.3±0.25mm, while a 13 μm thick ETFE film is introduced in specific regions of the preform, to create the necessary pre-cracks for the DCB delamination experiments and to obtain specimens with the half thickness for tensile testing.

For the elastic material moduli characterization two parallel approaches are adopted:

1. The aforementioned technique in §4.1, based on modal analysis [107] is initially adopted. For this purpose one coupon of the neat GFRP is cut from the infused plate, with dimensions 100×90×7.05 mm^3 and a second coupon of the tufted 5-SQ GFRP (from another infused plate) with dimensions 100×100×7.5 mm^3. These coupons are tested according to the technique described in [107] with excitation frequencies up-to 10kHz and the acquired results are treated with the designated procedures in [107].

2. Tensile testing of the neat GFRP composite is conducted according to [112]. For this purpose 4 coupons with dimensions 250×25×3.6±0.05 mm^3 are cut from the main plate in pairs of two since a the release film is used in the middle plane to obtain the half thickness. Three specimens are finally tested to acquire the longitudinal modulus, which is considered the same with the transverse one attributed to the cross-ply architecture, the Poisson's ratio, and the elastic and ultimate failure of this material.

The results of the two approaches are listed in Table 1, while for the normal to the thickness engineering constants, that could not be identified using the two mentioned procedures, values from the literature are used [2], for a material with similar reported in-plane properties. Also listed in Table 1, are the volume fraction values V_f of the fiber constituents, as acquired using the standard burnoff procedure [118]. The through the thickness properties, of the tufted composite of this study, are considered the same with the neat GFRP for simplicity. Thus, it is expected that the necessary bending properties are dominated by the in-plane engineering constants. The indices in Table 1 are explained in Fig. 3.1 and Fig. 7.2.

Furthermore, the elastic and ultimate tensile strength in the directions of the fibers, 109±3MPa and 457±5MPa respectively, with a mainly XVM failure mode (according to [112]), are acquired from the tensile experiments. The elastic limit, in terms of strains is calculated as ±4400 $\mu\varepsilon$.

Table 1: Material Properties-Engineering constants of woven cross-ply GFRP (Bold: experimental, Underline: modal analysis, rest literature [2]).

	E_z (GPa)	E_x (GPa)	E_y (GPa)	G_{xz} (GPa)	$G_{xy} = G_{zy}$ (GPa)	ν_{zx}	ν_{zy}	ν_{xy}	V_{f-Gf} (%)	V_{f-Cf} (%)
Neat GFRP	***24.9***	*11.6*	***24.9***	*5.5*	*6.4*	***0.12***	*0.15*	*0.2*	***52.5***	-
5-SQ	*29.8*	-//-	*26.5*	*5.7*	*5.7*	-//-	-//-	-//-	***48.8***	***0.49***

7.1.2 DCB specimens

The objective for this part of the work is to identify the effect of tufting as TTR on the investigated GFRP, in terms of fracture resistance and calculate the corresponding traction-separation relations. To do so, the neat GFRP composite is initially characterized before the tufted one, using for both cases simple DCB experimental configuration with EOFs.

In this document, results from 8 DCB specimens in total, 5 neat GFRP and 3 tufted specimens are presented. Theses specimens have a total length of 250mm, a width (B) of 25±0.1mm, as directed by [49], while the thickness (H_1) for the neat (Nt) is 7.1±0.1mm and 7.4±0.15mm for the 5-SQ. The resulted thickness per DCB arm is denoted as h_1. A schematic of the 5-SQ DCB specimen is illustrated in Fig. 7.1.

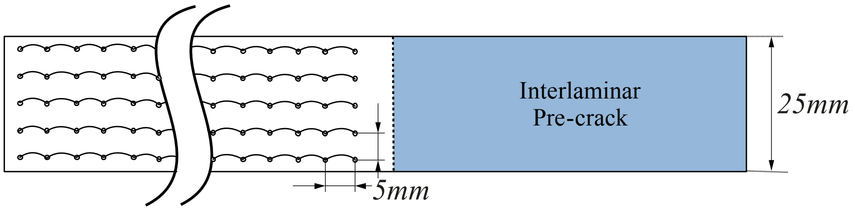

Fig. 7.1: Schematic of a 5-SQ DCB specimen.

Preliminary DCB experiments on the tufted composite demonstrate that, for the reported dimensions, bending failure on the arms precedes complete delamination and full tufting breakage. Therefore, stiffening of the DCB arms is required in order to complete successfully a DCB experiment with the tufted material. This stiffening is achieved by two, symmetrically bonded polymethyl-methacrylate (PMMA) beams of $h_2 =$14.5±0.15mm and the standard $B =$25mm. The bonding is done with a Loctite® 454, gel form, cyanoacrylate adhesive, after sandblasting the PMMA surfaces. This combination of transparent added material and adhesive, render a transparent finishing, providing a clear view of crack front advance, likewise to the neat GFRP composite (see Fig. 7.2).

The PMMA beams are manufactured by the “IM30” extrusion procedure by Perspex® and the manufacturer provides a Young’s modulus $E_P = 2250$ MPa, while a typical Poisson’s ratio $\nu = 0.4$ is considered. The aforementioned thickness of the PMMA reinforcement is chosen in such a way to have the bending neutral axis as close as possible to the adhesive layer, applying the lowest stress possible at the glue and moreover, the maximum bending stress on the PMMA to be much lower that its yield strength (~70 MPa, by Perspex®). Thus, the resulted neutral axis lies at ~0.5mm above the adhesive layer, for the described dimensions and material properties.

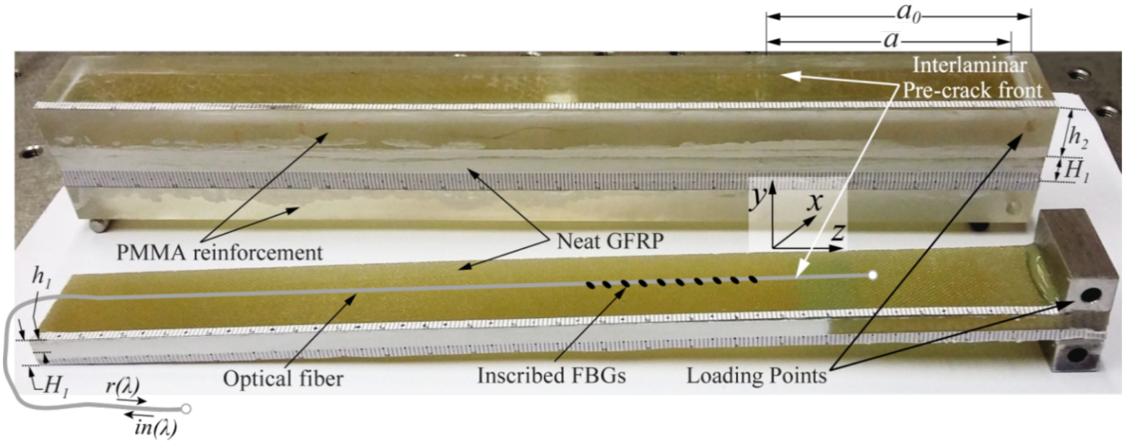

Fig. 7.2: Bottom: Typical neat GFRP with a schematic of an optical fiber bonded on the surface. Top: Typical neat GFRP specimen reinforced with PMMA beams.

Since, a scale-effect on the traction-separation relation is expected, caused by the DCB arm stiffening, 2 specimens of the neat GFRP are also reinforced with the described PMMA beams (Nt-PMMA) to identify the traction response of this stiffened DCB.

One neat GFRP specimen (Nt-3), is instrumented with an optical fiber for longitudinal strain measurements during fracture as described in §3.4, glued on the upper surface of this specimen. The employed OLCR technique (§3.5) for this case, revealed a center to center distance of 3.2 mm, resulting in a strain measurement region of ~32 mm along the fracture path. Embedding the optical fiber inside the composite during the stacking is not considered as an option because of the waviness of the fabric plies. Moreover, bonding an optical fiber on the top surface of the PMMA reinforced DCBs is also rejected since the strain sensitivity on the closing tractions of the crack faces is very small.

For all specimens with the PMMA, loading is applied directly on the arms with two pin-holes (Ø4mm) and for the non-reinforced ones simple steel loading blocks with a square cross-section (10×10×8mm^3 with a Ø4mm pin hole), as proposed also in [49]. These blocks are bonded with the 5 min Araldite® epoxy adhesive.

In these specimens, apart from the described white painting and the fine printed paper ruler on the side (§3.1), a second ruler is attached on the top to assist in monitoring the crack tip from both side and top-view.

All the described geometrical and physical characteristics of the created DCB specimens are depicted in the following Fig. 7.2.

7.2 Fracture testing

The experiments are performed at an ambient temperature of 22°C using a Shimadzu® AGS electromechanical testing machine equipped with a 5 kN load-cell with load and displacement recorded at a 10Hz frequency (see also §3.1). The experiments are conducted in displacement control at a rate of 2 mm/min. Two CCD high-resolution cameras are used, with one camera to always monitor the crack propagation on the side of the specimens. The second camera depending on the specimen, is either used to monitor the crack propagation from the top of the specimen, or employed to acquire images of the high contrast printed targets on bonded aluminum arms on the loading points as described in §4.2 and §4.3.4 (Fig. 4.7). The latter images are processed with an in-house digital image correlation algorithm employed to calculate the relative rotation, θ, between the two arms of the DCB specimen and calculate the ERR using Eq. (3.6). The image acquisition frequency is 1Hz.

7.3 Fracture morphology

Typical photographs of the side and top view from fractured specimens are presented in Fig. 7.3, as obtained by the CCD cameras during the experiments. A small difference on the detected crack advance, between the side and top view, is observed, with the top view to lead with 1-2mm. This can be attributed to a finite process-zone formation at the crack front, caused by the architecture of the fabric plies that forms a particular delamination plane. Moreover, observations on the side views of the neat GFRP reveal that single fiber-tow and/or partial ply bridging evolves during crack propagation, and this is also depicted on the created R-curves (§7.4.1 and §7.5.1). In the tufted DCB specimens both E-glass fiber-tows and tufts are bridging the crack faces.

Photographs and SEM micrographs of the fractured surfaces are displayed in Fig. 7.4. Here, tows bridging the crack are visible in both the neat GFRP and the tufted one. The main depicted damage mechanism is tow debonding with minimal E-glass fiber breakage. Additionally, on the tufted GFRP, total rupture of the tufted yarns is observed, comprising fiber-matrix separation and fiber breakage (Fig. 7.4(b)). The damage mechanisms around a broken tuft appear very similar to the ones of the neat GFRP. These observations of the fracture morphology provide useful information for the occurring damage mechanism and outline the numerical modeling techniques.

A typical inserted tuft in a cured plate, before testing is shown in Fig. 7.4(c). A typical tuft consists of two twisted threads.

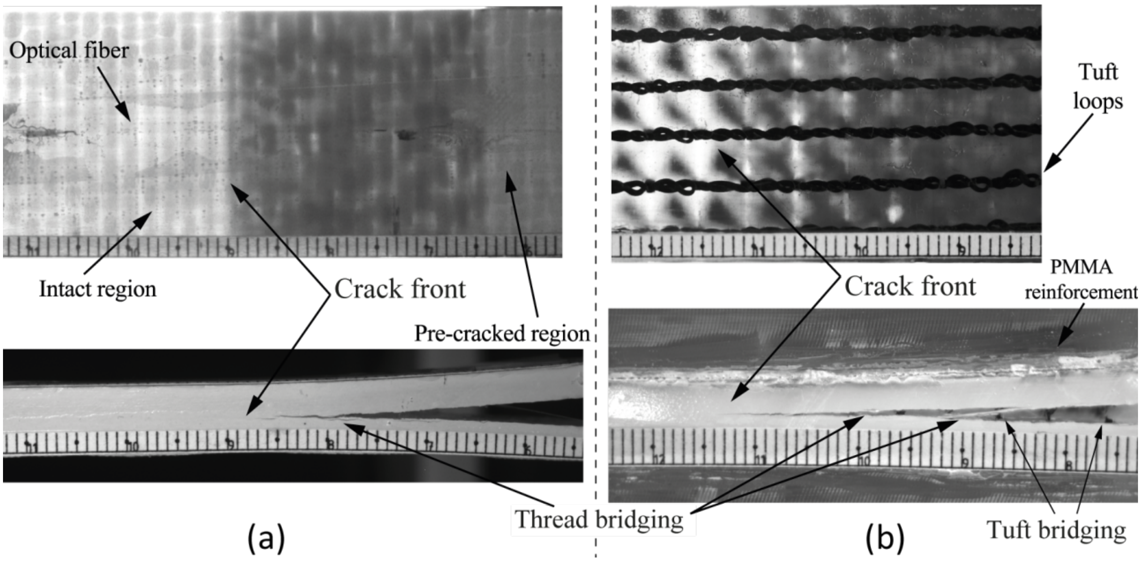
Optical fiber
Intact region
Crack front
Pre-cracked region
Thread bridging
(a)
Tuft loops
Crack front
PMMA reinforcement
Tuft bridging
(b)

Fig. 7.3: (a) Side and top view of DCB, neat GFRP specimen instrumented with an optical fiber. (b) Side and top view of DCB, tufted GFRP specimen.

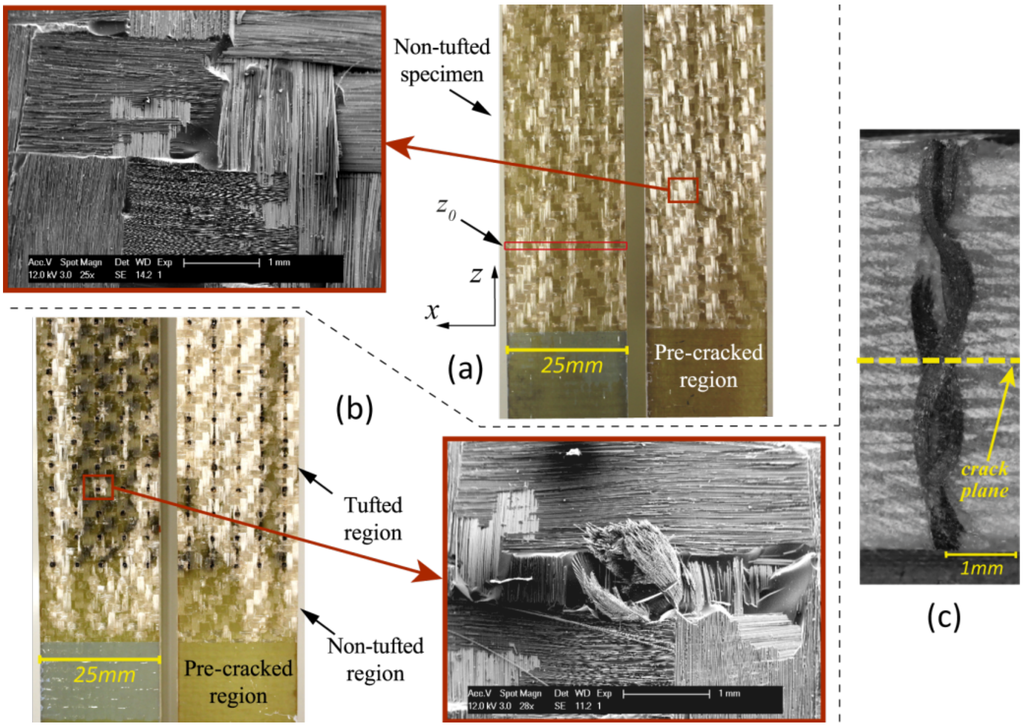
Acc.V Spot Magn Det WD Exp 1 mm
12.0 kV 3.0 25x SE 14.2 1
Non-tufted specimen
z_0
z
x
(a)
25mm
Pre-cracked region
(b)
Tufted region
Non-tufted region
25mm
Pre-cracked region
Acc.V Spot Magn Det WD Exp 1 mm
12.0 kV 3.0 28x SE 11.2 1
crack plane
1mm
(c)

Fig. 7.4: (a) Photograph of fractured neat GFRP with PMMA specimen and SEM detail.
(b) Photograph of fractured tufted GFRP specimen and SEM detail.
(c) Microscopy of an inserted tuft.

7.4 Results of neat GFRP

7.4.1 Experimental R-curves

The load, displacement and crack advance data from the neat GFRP DCBs, are employed to form R-curves based on the MCC method, shown in Fig. 7.5(a). The first point on the curves corresponds to first crack advance after the "pop-in" based on the deviation from linearity and visual observation criterion, (see [49]). The calculated critical ERR is $G_{I,i} = 270±30\text{J/m}^2$, for both regular and the reinforced DCBs. In all experiments, a very first fracture event before the "pop-in" is depicted, only on the top-view and the load-displacement curves and it corresponds to an ERR of 140-190J/m^2. This value is practically equal to fracture toughness of the epoxy resin given by [119]. The difference between the measured $G_{I,i}$ and fracture toughness of the pure matrix is attributed to the development of the finite process zone as described in §7.3.

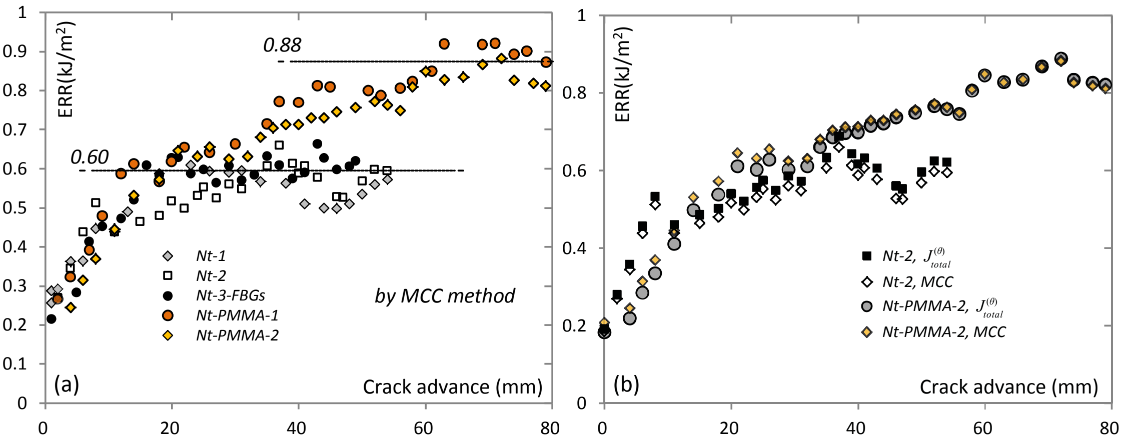

Fig. 7.5: (a) Experimental R-curves by MCC, of neat GFRP; with and without PMMA reinforcement. (b) Experimental R-curves by $J^{(\theta)}_{total}$*, of neat GFRP; with and without PMMA reinforcement.*

Important R-curve phenomena are present for this delamination mechanism, caused by the presence of tow bridging that may extend to partial ply-fabric bridging the crack. The maximum measured ERR for the reinforced DCBs, is approximately 45% higher than the corresponding values of the regular DCBs. This behavior resembles the results included in §5.3 and older studies [18,14]. As a result, the increase in fracture resistance is attributed to the higher bending stiffness of the DCB arms, due to the compound beam-arms whereas in §5.3 and [18,14], due to the thickness of the specimens.

As it is already mentioned, in selected specimens, the total rotations θ at the loading points are measured, to form R-curves using $J^{(\theta)}_{total}$ (Eq. (3.6)). These results are shown in Fig. 7.5(b), compared with the corresponding data from the MCC method. The depicted differences between the two methods are insignificant and even smaller compared to the results in §4 and [109], since the bridging phenomena are less dominant. Furthermore, the error in the reinforced specimen practically vanishes, thanks to the stiffer nature (i.e. small rotations) of this DCB, especially at the steady-state, where the fitting scheme for the MCC method is more stable in general.

7.4.2 Strain data

The recorded strains versus time for the instrumented neat GFRP specimens are shown in Fig. 7.6(a). This set of data depicts a quasi-brittle fracture response with relatively discrete steps at every crack advance event. These strain data are treated with the same method described in §4.3.2 and §5.3.3 to form the objective strain profile for the optimization procedure.

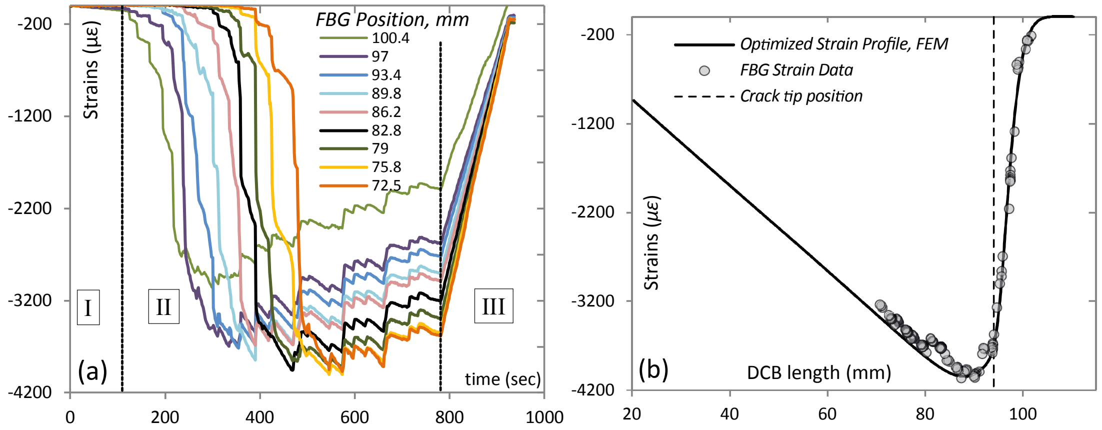

Fig. 7.6: (a) Strains versus time recorded by the FBGs. (b) Experimental strains and optimized numerical strain profiles at $\Delta a = 30$ *mm.*

7.4.3 Identification of traction-separation relations

Provided that a finite process zone is observed at the crack tip (§7.3), the identification scheme employed for the calculation of the traction-separation relations follows the scheme described in §3.6.1.2. In this scheme σ_c is considered equal to the tensile strength of the matrix, i.e. 40MPa as provided by the manufacturer [119], z_0 is constrained between 0-3mm and the other parameters are within the domains described in §3.6.1.1. The created numerical model for the inverse identification of this specimen consist of 6,139 quadrilateral, quadratic, reduced integration plain strain elements (Abaqus CPE8R) and it comprises the full geometry of DCB, in order to follow accurately any variations in h_1.

The adopted identification procedure for the regular, neat GFRP DCB specimen provides the following values: $\sigma_{\max} =$ 2.7 MPa, $z_{\max,1} =$ 25 mm, $\gamma_1 = 0.18$ mm^{-1} and $z_0 = 1.25$ mm. As a result, the initial assumption for a finite process zone is corroborated and its size appears to be related with pattern of the fabric (see (Fig. 7.4(a)). The strains' profile of the optimized solution and the objective experimental profile are shown in Fig. 7.6(b). Using the CODs from the FE model and the optimized tractions distribution, the traction-separation relation components $\hat{\sigma}_{pz}(\delta)$ and $\hat{\sigma}_b(\delta)$ are also identified. The calculated J_{pz} (Eq. (3.16)) is about 260 J/m^2, which is in good agreement with the measured $G_{I,i}$.

To obtain the traction-separation relation for the PMMA reinforced DCBs, a scheme similar to the one described in §5.3.4 is created:

(iii) Initially, it is assumed that the first component of the traction-separation relation, $\hat{\sigma}_{pz}(\delta)$, is independent of the arm's stiffness and, $\sigma_{\max}$ is considered unique, characteristic of the fracture mechanism. With these two assumption the first linear softening part of $\sigma(\delta)$, is defined.

(iv) To predict the cohesive law, $\hat{\sigma}_b(\delta)$ within the bridging zone, $\sigma_b(\hat{z})$ (Eq. (3.14)) is employed. Here, only one specimen, with a given stiffness is identified, with the inverse identification scheme based on the FBG strain measurement. Therefore, a relationship for $z_{\max}$, as in Fig. 5.9, cannot be established. However, $z_{\max}$ practically, represents the point on the R-curve that the steady-state propagation begins, and for the Nt-PMMA specimens is approximated to 60mm, based on the results illustrated in Fig. 7.5.

(v) To complete the definition of $\sigma_b(\hat{z})$ the parameter γ, needs to be assessed. To this end, the bending stiffness of the DCB arm is considered in order to generalize the $\gamma H = const$ relationship, established in the results of §5.3 and [18,14]. Assuming that the key parameter for the presented scale-effect on the traction-separation relations in the UD composites, is the different stiffness, reflected on the unique variable of these studies, i.e. the thickness of the arms, h, or H (for the total one), $\gamma H = const$, or $\gamma h = const$ can be reformulated as:

$$\gamma^3 k = const \qquad (7.1)$$

Here, k is the corresponding bending stiffness, as $k = EI$ where E is the bending modulus of a beam and I is the second moment of the cross-sectional area (i.e. $I = Bh^3/12$). Here, the Beam Theory approach for composite beams is implemented, since the stiffened DCB consists of two compound arms. Thus, the total area moment of inertia $I_{1,2}(h_1, h_2, E_P)$ is calculated and the bending stiffness is $k_{Nt-PMMA} = E_z I_{1,2}$. The corresponding bending stiffness for the regular neat GFRP is $k_{Nt} = E_z I_1$, with $I_1 = Bh_1^3/12$. With the bending stiffness calculated, for both DCB types and by using Eq. (7.1), the ratio $k_{Nt-PMMA}/k_{Nt} = \gamma_1^3/\gamma_2^3$ is approximately 29.5, thus, $\gamma_2 \simeq 0.06$.

To this end, the parameters $\sigma_{\max} =$ 2.7 MPa, $z_{\max,2} =$ 60 mm, $\gamma_2 = 0.06$ mm^{-1} and $z_0 = 1.25$ mm are implemented in Eq. (3.13) and (3.14), to form the closing tractions profile.

The calculated closing tractions profile with the aforementioned procedure for both the regular and the PMMA reinforced DCB are shown in Fig. 7.7. These tractions are subsequently applied in a numerical model similar to the one depicted in Fig. 3.10, this time with the PMMA reinforcement included, instead of the loading blocks. In this model perfect interface is considered between the composite and the PMMA beam, while the thickness of the glue (~0.15 mm) is added to the PMMA arms, assuming alike acrylate nature (i.e. unique E_P). In this model, perfect symmetry is assumed, and the modeled compound arm of the specimen is discretized with 14,730 quadrilateral, quadratic, reduced integration plain strain elements (Abaqus CPE8R). The modeled crack length and the displacement applied correspond to a point within the steady-state of the tested specimens.

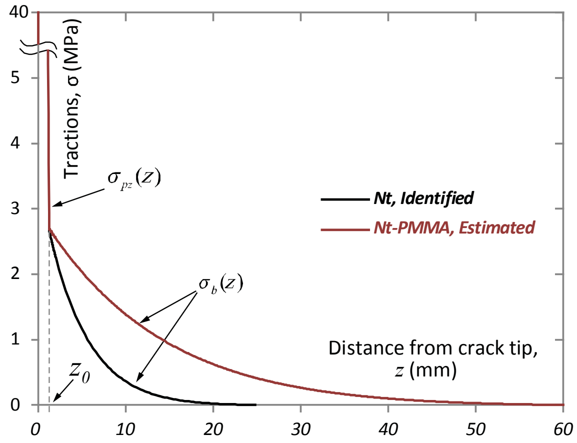

Fig. 7.7: Calculated tractions profiles.

From the resolved numerical model, the CODs corresponding to the estimated tractions profile are acquired, to form the traction-separation relation inside the bridging zone. Then, the estimated $\hat{\sigma}_b(\delta)$ is appended to the identified $\hat{\sigma}_{pz}(\delta)$, to form the complete relation. The two calculated traction-separation relations, for both the regular neat GFRP and the reinforced DCB specimens, are depicted in Fig. 7.8(a).

The incremental integration procedure as summarized in Eq. (4.1), substituting J_{tip} with J_{pz} (see Eq. (3.16) and insert in Fig. 7.8(a)), is used to form R-curves based on the calculated traction-separation relations. These R-curves are compared with the experimental ones in Fig. 7.8(b). It should be noted here that the energetic calculation, especially for the fully developed region, is in good agreement with the experimental values using MCC method. Some overestimation is observed on the rising part (10-20%), which may correspond to a transitional phase in the development of the tow bridging phenomena. Similar behavior is observed in the studied UD layered composites (§4.3.5 and §5.3.6), where it is attributed to the evolution of bridging bundles size (see Appendix III).

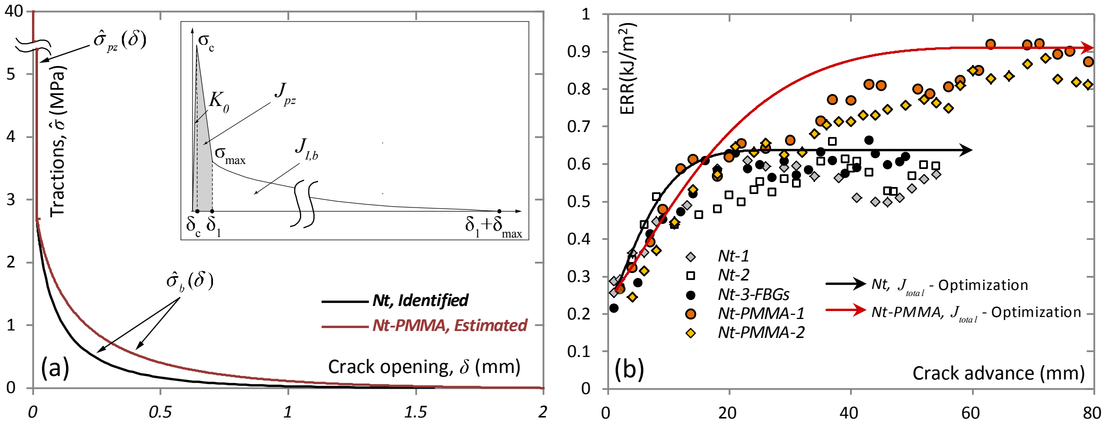

Fig. 7.8: (a) Overall traction-separation relations.

(b) Experimental R-curves and numerical ones, using the calculated traction-separation relations

7.4.4 Load-displacement response and cohesive zone modelling

The calculated traction-separation relations are implemented in a FE model with a zone of cohesive elements, as described in §3.6.2. Two models are created, one for the regular neat GFRP and one for the reinforced, comprising 23,638 and 35,960 respectively. The acquired load-displacement curves are compared with the experimental ones in Fig. 7.9.

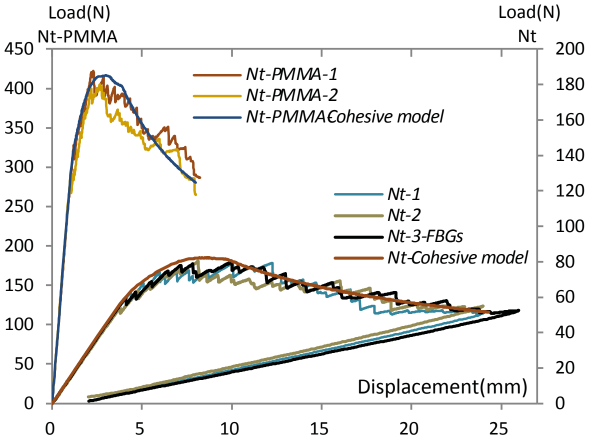

Fig. 7.9: Experimental and numerically obtained load-displacement response.

7.5 Numerical approach and experimental results of the tufted GFRP

7.5.1 Experimental R-curves

As it is already mentioned, three 5-SQ tufted DCB specimens are tested. In two of them, the initial precrack front is positioned at ~20mm before the first row of tufts. As a result, there exists sufficient path for the initial "pop-in" crack advance, and a natural crack tip is formed before reaching the first row of tufts. The resulted R-curves, for these two specimens, using the MCC method are illustrated in Fig. 7.10(a). As seen in this figure, these specimens practically reached the expected, maximum ERR value (Fig. 7.5 and Fig. 7.8(b)), for the non-tufted DCB (Nt-PMMA) before the depicted steep rise of the R-curves, as soon as the crack front reached the first row of tufts. Finally, the depicted R-curves reach a maximum ERR of 3.1 kJ/m^2 followed by steady-state crack propagation. The crack advance in the plateau region shows small jumps of 3-4mm, since in the experiment it is observed that 1-2 rows of tufts break at the same instance.

In the third specimen (5-SQ – 3), the release film is positioned just 2-3mm before the first row of tufts. The R-curve of this specimen is also shown in Fig. 7.10(a). Here, the initial fracture toughness is practically the same, while after the "pop-in", crack propagation is constrained after crossing the first row of tufts. From this experiment, it is demonstrated that tufting will not prevent an initial delamination when the provided crack driving force, is higher than the critical $G_{I,i}$ of the neat composite material. However, the crack propagation will arrest once the first tufts start bridging the crack faces, resulting to a maximum ERR that is more than 3.5 times higher than the maximum value recorded for the neat GFRP composite. As a result, the toughening effect of tufting is of high importance as also reported in previous studies [75,76]. Nevertheless, the magnitude of toughening is strongly related with the material, the geometry and the density of the tufting pattern.

For completeness, the rotation θ is measured in one 5-SQ DCB, in order to calculate R-curves using $J_{total}^{(\theta)}$ as in Eq. (3.6). These results are shown in Fig. 7.10(b) and they are compared with the corresponding ones using the MCC method. The depicted differences between the two methods are insignificant, even though important closing tractions are imposed by the bridging tufts. Nevertheless, the flexural rigidity of these DCB specimens and the absence of loading blocks, minimizes the effects of large displacement thus, the linear approximation and the generic ERR calculation converge to very close ERR values.

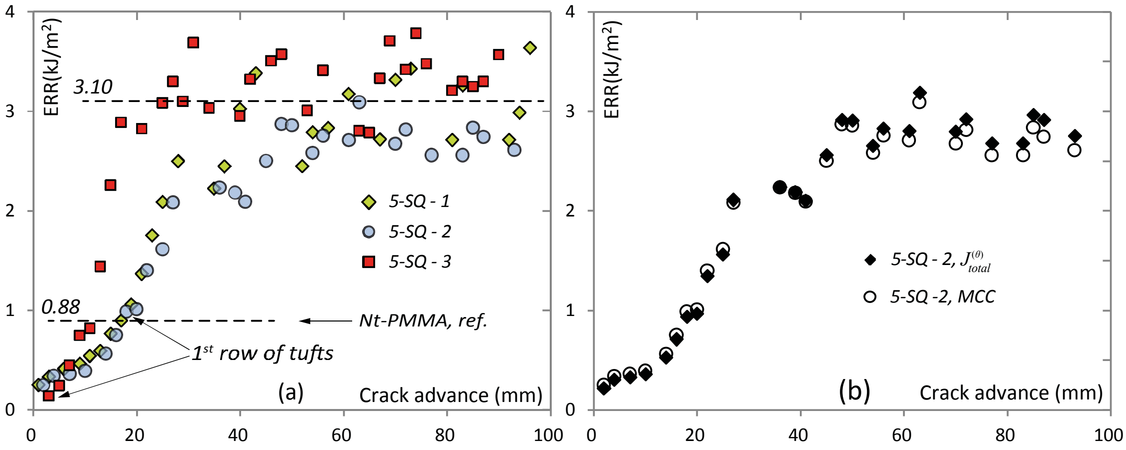

Fig. 7.10: (a) Experimental R-curves by MCC, of 5-SQ GFRP; read text for details.

(b) Experimental R-curves by $J^{(\theta)}_{total}$*, of 5-SQ – 2 DCB specimen.*

7.5.2 Uniaxial tuft pulling tests

Based on the fractographs depicted in Fig. 7.4, it is presumed that the final closing tractions profile on the DCB is a superposition of the tractions profile induced by the tow bridging phenomena and the bridging tufts. As a first order approximation, it is assumed that the two phenomena are completely decoupled. To this end, uniaxial tuft pulling tests are designed and conducted to isolate the contribution of bridging tufts on the traction-separation relations.

To create these testing coupons, some regions of the preform are separated with a release film, in the symmetry plane of the stacking, before being tufted. As a result, these regions, after the resin infusion, are only held together by the infused tufts. Five square plate-coupons (20×20mm^2) are cut from the described regions containing 9 tufts of a 5-SQ pattern (see Fig. 7.11(a)). These coupons (referred to as 5F-SQ) are later bonded to aluminum cross-drilled blocks using the 5 min Araldite® epoxy. The resulted specimens are uniaxially pulled in the same testing machine that the DCB experiments are conducted, using assisting components as illustrated in Fig. 7.11(a). This gripping mechanism induces only axial pulling forces without allowing any moments to develop. A comparison of the SEM micrographs of the broken tuft of the DCB specimens in Fig. 7.4(c), and the corresponding ones in Fig. 7.11(a), show a similar failure mechanism of per individual tuft.

These experiments are conducted in displacement control at a 0.5mm/min constant rate, while one coupon without the release film is also tested to deduct the compliance of testing setup. The resulted load-displacement response of all specimens, reduced per single tuft, is depicted Fig. 7.11(b). In this graph, four key points can be located: (A) is the end of linear response of the tuft. After this point, a quasi-linear hardening is observed up to point (B) which is located at the ultimate strength of the tuft. In the region between (A) and (B) some damage occurs, as the tuft threads appear to be circumferentially debonded from each other and/or the host GFRP material, while the carbon fibers are still intact. After point (B), major failure of the tuft threads is observed, depicted on the load displacement-response as a sudden drop until point (C). The last part of the failure mechanism comprises breaking of the residual matrix and intact fibers, until the ultimate failure of the tuft at point (D). The overall energy absorbed per tuft before the ultimate failure is calculated by numerically integrating the load-displacement response as $\Psi_{tuft} = 41.2$ mJ ±7.3%. An equivalent G_{tuft} can be calculated, assuming that the effective cross-section of a tuft is circular with a diameter of 1mm, as $G_{tuft} = 52.5$ kJ/m^2.

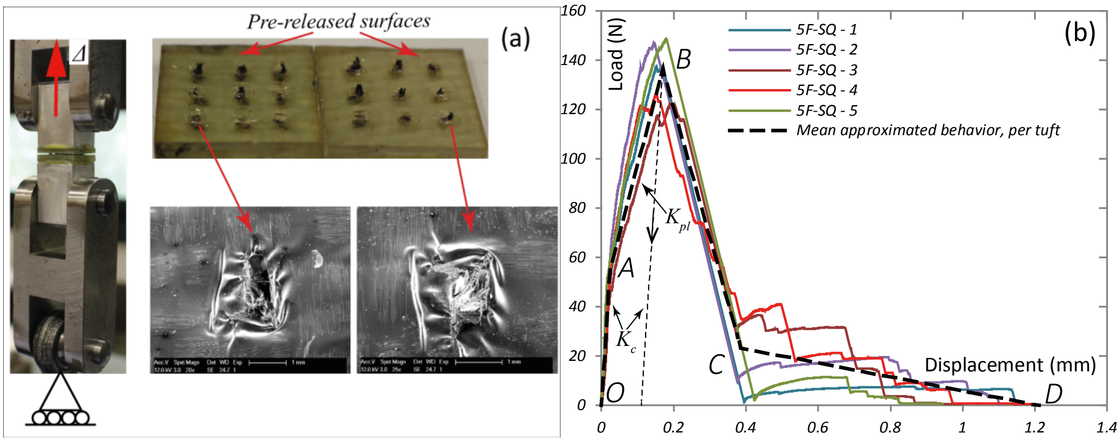

Fig. 7.11: (a) Uniaxial pulling testing setup and fractured surface: photographs and SEM. (b) Experimental load-displacement response, normalized pet tuft and mean approximation.

7.5.3 Load-history prediction modeling

To simulate the fracture response of the tufted DCB specimens it is assumed that the two bridging phenomena (tow/ply and tuft) are completely decoupled. In this framework, a 2D plain strain model is built, where a homogenized cohesive element zone is employed to model the delamination phenomena with the tow bridging contribution, while discrete connector elements are used to simulate the response of the tufts.

In this model, the compound DCB arms are modeled with two sections, one isotropic for the PMMA and one composite, with the anisotropic properties reported in Table 1 for the 5-SQ. Similar to the previously described models, perfect interface is assumed between the composite and the PMMA section. These arms are discretized with 17,880 quadrilateral, quadratic, reduced integration plain strain elements (Abaqus CPE8R). The two symmetric arms are connected together with a zone of cohesive elements, as described in §3.6.2, with the estimated traction-separation relation for the Nt-PMMA specimen, displayed in Fig. 7.8(a).

Moreover, connector line-elements are superimposed to the cohesive zone (one element for each row of 5 tufts) and are connected with the two DCB arms by a kinematic coupling transferring only displacements, with an influence zone of 1mm (approximately equal to tuft's diameter as in Fig. 7.4(c)). The connector elements (Abaqus CONN2D2) are of Cartesian type, and their response is designed to follow the mean approximated behavior (Fig. 7.11(b)) per tuft × 5 (for each row). This behavior comprises four parts as also presented in Fig. 7.11(b):

The first one, -OA-, represents the linear-elastic region of the tufts with an elastic stiffness K_c. The second segment, -AB-, represents the linear hardening response which is simulated as plastic isotropic hardening, with a slope K_{pl}. The last two parts, -BC- and -CD- contain the damage evolution that is considered as a bilinear softening response. The overall force-separation relation is summarized in Eq. (7.2), where $F_{c,X}$ is the reaction force of the connector at each key-point X, and $\delta_{c,X}$ is the corresponding relative displacement of the two connector's nodes.

$$F_c\left(\delta_c\right)=\begin{cases} K_c\delta_c,\ for\ 0\leq F_c\leq F_{c,A} \\ K_{pl}\left(\delta_c-\delta_{c,A}\right)+F_{c,A},\ for\ F_{c,A}<F_c\leq F_{c,B} \\ \left(1-D(\delta_c)\right)\left(K_{pl}\left(\delta_c-\delta_{c,A}\right)+F_{c,A}\right),\ for\ F_{c,B}<F_c\leq F_{c,D} \end{cases} \tag{7.2}$$

The values for the main variables of Eq. (7.2) are included in Table 2. The elastic limit, $F_{c,A},\delta_{c,A}$ and the ultimate strength point, $F_{c,B},\delta_{c,B}$, as well as the maximum opening $\delta_{c,D}$, are simply the mean recorded experimental values. The first segment of the bilinear softening (point (C) in Fig. 7.11(b)) is defined in such a way that the overall approximated energy, matches the mean Ψ_{tuft}. Moreover, the damage parameter,

$D(\delta_c)$, is evaluated for ~40 increments, based on and the load-displacement values at points (B), (C) and (D) and the effective response described in Eq. (7.2). The parameter $D(\delta_c)$ is implemented in the connector properties in a tabular form.

Table 2: Mean aproximated behavior per tuft and per connector element.

	K_c (N/mm)	K_{pl} (N/mm)	$F_{c,A}$ (N)	$F_{c,B}$ (N)	$F_{c,C}$ (N)	$\delta_{c,C}$ (mm)	$\delta_{c,D}$ (m)
Per tuft	*2307*	*574*	*55*	*136.5*	*23.5*	*0.385*	*1.21*
Per connector i.e. tuft ×5	*11535*	*2870*	*275*	*682.5*	*117.5*	*-//-*	*-//-*

An illustration of the created FE model, with the calculated equivalent stress-field and the boundary conditions indicated, is shown in Fig. 7.12(a). Also indicated in this figure are the cohesive element zone and the connector elements. The created model is solved using Abaqus implicit dynamic quasi-static solver and the density for both PMMA and GFRP section is considered equal to a mean density of 1.5g/cm^3, corresponding to representative values for such polymers (1.15g/cm^3 for PMMA and 1.9g/cm^3 for GFRP).

The load history prediction from this model and the experimental load-displacement response are compared in Fig. 7.12(b). At this point it should be noted that the created FE model follows the geometry of 5-SQ – 1 & 2. The data in Fig. 7.12(b) show that the model predicts very well the response until the maximum force, while later tends to underestimate DCB's load history by ~10%. This can be attributed to the fact that the created model is 2D and as a result each connector's failure represent the failure of one complete row of tufts, while in the actual experiments it is observed that a combination of 2-3 rows contributes. A 3D model would require a random distribution of tuft properties within the experimental range, to capture such effects. Furthermore interaction of the tuft and tow/ply bridging mechanisms may occur, while in this approach complete decoupling is considered. In any case, the created model is a very good approximation of the actual experiment.

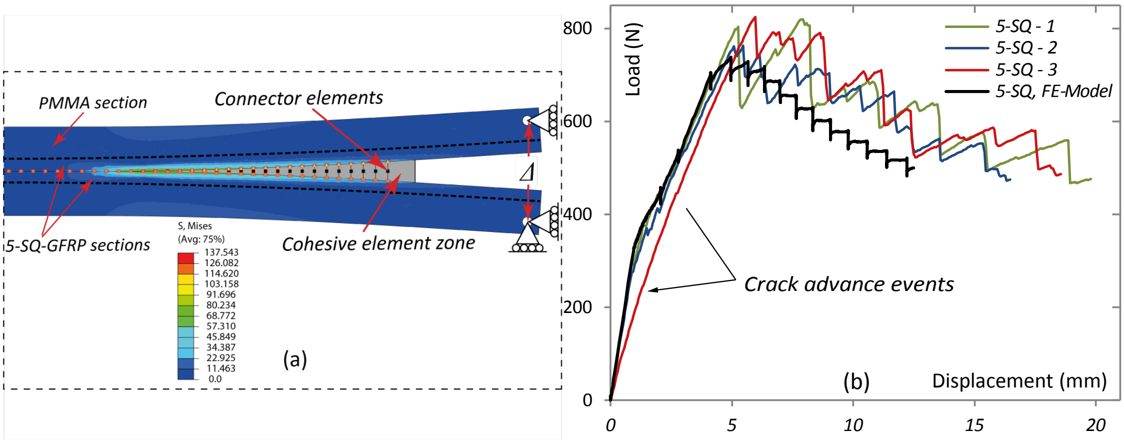

Fig. 7.12: (a) Snapshot of the FE model with key-regions and boundary conditions indicated. (b) Experimental and modeled load displacement response.

7.6 Key points summary and discussion

As it is derived by this study, tufting has a very important toughening effect in the tested GFRP system, similar to what is as also reported in previous studies [75,76]. Moreover, the tow/ply bridging phenomena are of quite high importance, and cannot be neglected on the modeling of the delamination response of the tufted GFRP, compared to previous studies [76] where only matrix failure is considered.

The designed and conducted uniaxial pulling test, with 9 tufts instead of single one provides stability to the experiment, improving the repeatability. Furthermore, data of 9 tufts are already averaged, reducing the amount of required experiments to acquire a reliable statistical sample.

The proposed numerical modeling technique is very successful using a 2D model allowing for a very fine mesh keeping low the processing cost. Moreover, the employed connector elements and the implemented constrains, can simulate very well the failure of the bridging tufts eliminating the need for an embedded cell approach and complicated models. Superposition of the tufting failure mechanism and the tow/ply bridging phenomena stands as a good approximation, while some small interaction between the two mechanisms might be present.

Additionally, the proposed generalization of the empirical formula to calculate the bridging traction profile exponent as $\gamma^3 k = const$, allows for a realistic estimation of the traction-separation relation $\hat{\sigma}_b(\delta)$, for the investigated range of DCB arms' stiffness.

Chapter 8

Concluding remarks

8.1 General discussion & conclusions

The conducted study is dealing with the characterization of R-curve phenomena in crack propagation of FRP composite materials due to LSB and TTR. In particular, identification techniques of the traction-separation relations are proposed while mechanistic investigations and qualitative analysis is performed based on microscopy.

The characterization of the UD carbon/thermoplastic system demonstrates that the toughening effect of LSB in intralaminar fracture is almost double compared to the corresponding interlaminar values. A similar response is depicted on the carbon/thermoset system. The tractions-separation relations produced by the proposed inverse identification method compare very well with the results from a numerical micromechanical model using the embedded cell approach. Moreover, the ERR calculated employing the traction-separation relations are in good agreement with the experimental R-curves.

The comparison of the mode I R-curves, of the investigated carbon/epoxy system, with EOF and PM loading conditions show minor differences on the maximum ERRs, with some small difference on the shape of the R-curves.

The calculated R-curves for the whole series of experiments, demonstrate some sensitivity of the calculated ERR with respect to the employed formulation of G or J. Consequently, the direct method proposed in the literature [8,9,10,15] etc., to identify the traction-separation relations that employs the measured CODs and ERRs, may provide questionable results since, a typical tractions profile consists of high stress gradient near the crack tip, and nearly asymptotic fields towards the tail.

In most of the studies in the literature dealing with LSB and specimen size, a dependency on the shape of the R-curves and specimen size is reported, but the traction-separation relation is considered independent of specimen geometry and is treated as a material parameter. However, this study demonstrates apparent scale effects on the traction-separation relations under the presence of LSB, with a strong influence of specimen thickness (§5), also reported in [18] and [14], that can be practically related to the stiffness of a specimen as shown here (§7.4). The outcome of this work is a proposition of traction-separation identification scheme, based on the closing tractions profile. According to the described procedure a closing traction profile can be identified using specimens with a reference geometry, and extrapolate the acquired profile using the proposed relation: $\gamma^3 k = const$, to predict the closing tractions for a structural component with different bending stiffness k. The applicability of this relation is verified for stiffness ratios up to 30. As a result, instead of identifying a traction-separation relation for each possible component's stiffness, for example using the described inverse method, the proposed extrapolation procedure can be initially applied to evaluate the closing tractions profile and consequently estimate the traction-separation relation.

The described approach facilitates significantly the process of traction-separation relation estimation. Yet, experiments on specimens with stiffness that corresponds to the structural component of interest needs to be conducted, to define the boundary conditions of the numerical model and the extent of the bridging zone, even though no elaborate identification procedure is needed. Therefore more elegant solutions are in quest. A recent study [120], proposes the creation of cohesive elements that take into account the tractions as a function of both COD and local angle. This methodology provides a useful tool to treat toughening phenomena like LSB. However, it is built for a generic case, where complex data sets are needed to create a 3D surface for the function of the tractions with respect to CODs and local angles.

The results of the current study in the carbon/epoxy system render $J_{I,b} / \sigma_{\max} z_{\max} \tan\varphi_{\max} \simeq 0.068$ regardless of specimen thickness (§5.3.4). Therefore, the traction-separation relation can be enriched with a complementary kinematic parameter, i.e. the local crack opening angle (COA), φ, to form a traction's relation defined as $\hat{\sigma}'_b(\delta,\varphi)$. The COA criteria have been proposed also in the past to model the fracture response of metals as described in [115,88] and references therein. For simplicity it can be assumed that $\varphi \simeq \tan\varphi$. In particular, the relation between $\hat{\sigma}_b$ and the product $\tan\varphi \cdot COD$ or, equivalently $\hat{\sigma}'_b(d\delta/dz \cdot \delta(z))$ for all investigated thicknesses of the carbon/epoxy system, is plotted in Fig. 8.1. Remarkably, the three curves presented in Fig. 5.7, practically collapse to one single curve.

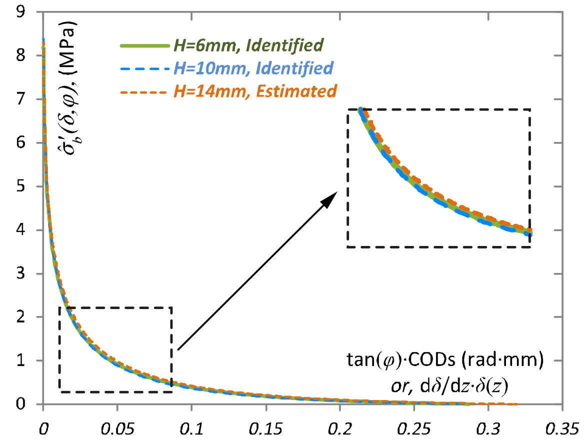

Fig. 8.1: Calculated traction-separation relations as a function of CODs and local angle, per specimen thickness; UD carbon/epoxy system.

Similar results can be obtained for $\hat{\sigma}'_b(d\delta/dz\cdot\delta(z))$ of the investigated woven neat GFRP composite. Consequently, the bridging parts of the two curves showed in Fig. 7.8(a), collapse to one single curve as illustrated in Fig. 8.2. In this case, the maximum COD × COA, is not as clearly defined as in the aforementioned carbon/epoxy series, nevertheless, the calculated $\hat{\sigma}'_b(d\delta/dz\cdot\delta(z))$ demonstrates a nearly asymptotic behavior towards the end of the bridging zone, with minor energetic contribution for $d\delta/dz\cdot\delta(z) >$ 0.11rad·mm.

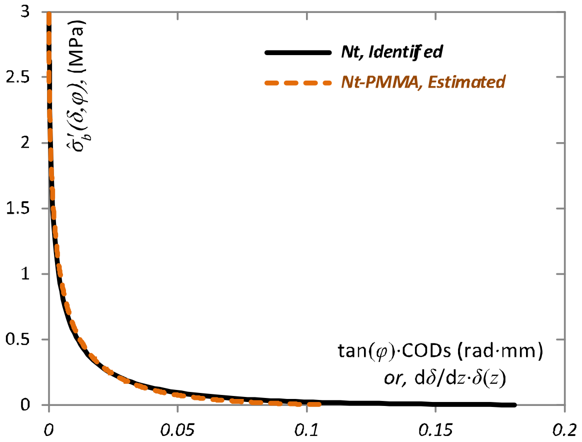

Fig. 8.2: Calculated traction-separation relations as a function of CODs and local angle, per investigated stiffness; Woven GFRP system.

These results provide a relatively simple traction-separation and angle relation that can be considered as material/fracture mechanism property (within the range of stiffness and local angle investigated here), to be used in a cohesive model, like the one proposed in [120]. Such a result is a very useful tool in the damage tolerant design given that characterization of only one specimen is sufficient to describe fracture response of a structural component, provided that the local rotations on the wake of the crack are known.

8.2 Research perspectives and future work

One of the objectives of this study was to investigate whether a traction-separation relation, of a certain fracture mode, identified from one loading case is valid on other loading conditions of the same fracture mode. A comparison between the results of the EOF and PM series, demonstrates that minor differences are expected when the loading conditions change. Nevertheless, more experiments can be conducted with other mode I loading condition to inspect the range of validity of the aforementioned findings and further investigations may be carried out, with different systems that demonstrate R-curve phenomena.

The traction-separation relation is proven to be geometry dependent and not a material property as often considered in the literature. The effect of scale and the definitions of the proposed tractions-separation and angle relation as a material property needs to be further investigated.

Moreover, similar analysis and experimental program can be carried out with different fracture mode mixity involving all the pure moment configurations which are assumed to provide J-integral measurements ‘independent of the details of the traction-separation relations’ according to [8,9,27], which are the equivalent of the EOF cases described in [121]. To this end an adaptation of the designed and built pure-moment testing apparatus for mode II and mixed-mode cases is already in designing process at LMAF. Implementation of this adaptation can lead to a new series of experiments with this meticulously designed testing setup. Similar experiments are presented in [27], but those results have never been compared with the corresponding ones from the EOF cases. Of great interest would be to verify the validity of the aforementioned mixed-mode cases in PM under fatigue conditions and furthermore, investigate the effect of stiffness similar to the analysis conducted for the mode I case in [122].

The results of this work show that the role of microstructure (fiber distribution and clustering) plays an important role in the extent of LSB. Thus, investigations on microstructures that favor LSB phenomena may be carried out. Moreover, effects of fiber clustering on the extent of LSB have been also reported on delamination and bridging phenomena of thin ply composites as a function of ply thickness [45].

Therefore, those results, along with the findings of §6.7, pose new questions on the effect of fiber clustering in damage accumulation and its extent. To this end, the presented micromechanical approach can be applied in conducting virtual tests that incorporate the aforementioned differences in the microstructure.

Appendix I

Numerical calculation of J-integral

The J-integral is calculated numerically and compared with the ERR at initiation, $G_{I,i}$, in the optimization scheme (§3.5.1). In this section it is shown that the ERR at the crack tip, J_{tip}, calculated numerically, can be considered path-independent, even inside the bridging zone. Details of relevant definitions are illustrated in Fig. I.1.

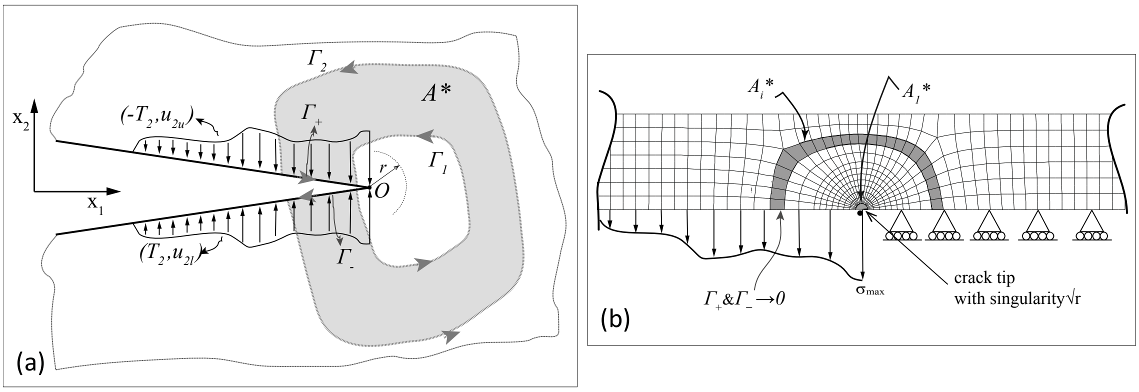

Fig. I.1: (a) Definition of the contour J-integral in presence of bridging tractions.
(b) Domain integral definition.

The general definition of the J-integral as given by [30] can be formed as:

$$J\big|_{\Gamma} = \oint_{\Gamma}\left(w dx_2 - T_i \frac{\partial u_i}{\partial x_1} ds \right) \text{ or, for investigated mode I case:}$$

$$J\big|_{\Gamma} = \oint_{\Gamma}\left(w dx_2 - T_2 \frac{\partial u_2}{\partial x_1} ds \right) \qquad \text{(I.1)}$$

The calculation tool of Abaqus v6.12 [57] uses the numerical implementation of Eq. (I.1) [123] as a result of the divergence theorem for an area domain A^* with q being an arbitrary, but smooth function that is equal to unity on Γ_1 and zero on Γ_2 (Fig. I.1(a)):

$$J_{num} = \underbrace{\int_{A^*}\left[\left(\sigma_{ij}\frac{\partial u_j}{\partial x_1} - w\delta_{1k}\right)\frac{\partial q}{\partial x_i}\right]dA}_{J_{tip}} - \int_{A^*}\left[\xcancel{F_i\frac{\partial u_j}{\partial x_1}q}\right]dA - \int_{\Gamma_+ + \Gamma_-}\xcancel{T_2\frac{\partial u_j}{\partial x_1}q}\,d\Gamma \tag{I.2}$$

Here the contribution of body forces is neglected and the crack faces are traction free. When tractions are applied on the crack faces, σ_{ij} and u_j are the combined results due to the implemented boundary conditions and bridging tractions.

Based on the energy balance, the fracture energy of a specimen with bridging tractions, along part of the crack faces (Fig. I.1 (a)), can be calculated using the J-integral expression [8] or numerically by the domain integral [123] given by:

$$J_{A^*} = J_{tip} + \int_0^{\delta^*}\hat{\sigma}_b(\delta)d\delta \overset{(8)}{=} \int_{A^*}\left[\left(\sigma_{ij}\frac{\partial u_j}{\partial x_1} - w\delta_{1k}\right)\frac{\partial q}{\partial x_i}\right]dA - \int_{\Gamma_+ + \Gamma_-} T_2\frac{\partial u_j}{\partial x_1}q d\Gamma \tag{I.3}$$

Conventionally, calculation of J_{tip} under the presence of surface tractions is carried out using domain $A_1{*}$ Fig. I.1 (b) including only the near tip region $r \to 0^+$ [123]. Alternatively, for a radial mesh around the crack tip (Fig. I.1 (b)), with a very fine step and defined domains $A_i^*(i = 1,2,3,...)$, the contribution of the tractions on contours Γ_+, Γ_- is infinitesimal and can be neglected. Thus, the calculated domain-integral $J_{A_1*}$from area A_1^* can be approximated by the integrals of any of the following domains, $A_2^*, A_3^*, A_4^*,....$:

$$\begin{gathered} for\,\Gamma_+,\Gamma_- \to 0 \Rightarrow \int_{\Gamma_+ + \Gamma_-} T_2\frac{\partial u_j}{\partial x_1}q d\Gamma \to 0 \Rightarrow \\ G_{I,i} = J_{tip} = J_{A_1*} \approx J_{A_2*} \approx ... = J_{A_i*} = \int_{A_i*}\left[\left(\sigma_{ij}\frac{\partial u_j}{\partial x_1} - w\delta_{1k}\right)\frac{\partial q}{\partial x_i}\right]dA \end{gathered} \tag{I.4}$$

This can describe a domain-independent tool, similar to the path-independent subcase of the J-integral under existence of bridging tractions for body contours, that start and finish on the same $x_1$coordinate as described by [124]. Therefore, J_{A_i*} is considered equal to the initial fracture toughness,$G_{I,i}$, independent of the domain.

The validity of the previous calculation can be seen in the following Fig. I.2 for the calculated J_{num} using Abaqus domain integral tool in several contours (starting from the tip A_1^*, for the $H = 10$ mm) using the identified bridging tractions and the corresponding values at crack initiation (i.e. without bridging), for the carbon/thermoset composite. The results in Fig. I.2 illustrate a domain dependency with a variation of 0.14%, which is considered negligible.

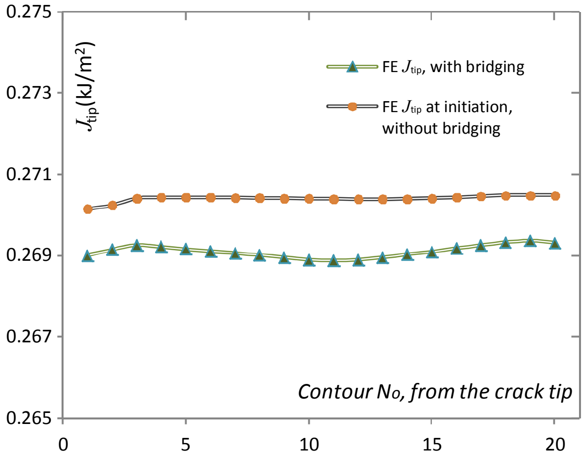

Fig. I.2: Resulting values of J_{tip} *for different contours, with and without bridging,* $H = 10$*mm; as published in [55].*

Appendix II

Material and specimen fabrication

A schematic of the specimen preparation procedure, for the UD carbon/epoxy system, from the autoclave curing, to the specimen testing, is shown in Fig. II.1. A photograph of the fabricated mold to accommodate the composite plates, positioned on the rack of the autoclave, is displayed in Fig. II.1(a). This mold comprises a rigid cup and a rectangle sub-frame, designed to restrain the resin flow on the direction normal to the fibers and moreover, to assure repeatability on plate's thickness and volume fraction. This mold allows resin flow, under vacuum conditions, from the two short edges, as it is depicted on the photograph of the cured plate in Fig. II.1(b). This curing process with the described mold, vacuum and supplementary pressure of 3 bar, provides a material with very low void content, as depicted in the cross-section micrograph of Fig. II.2(a).

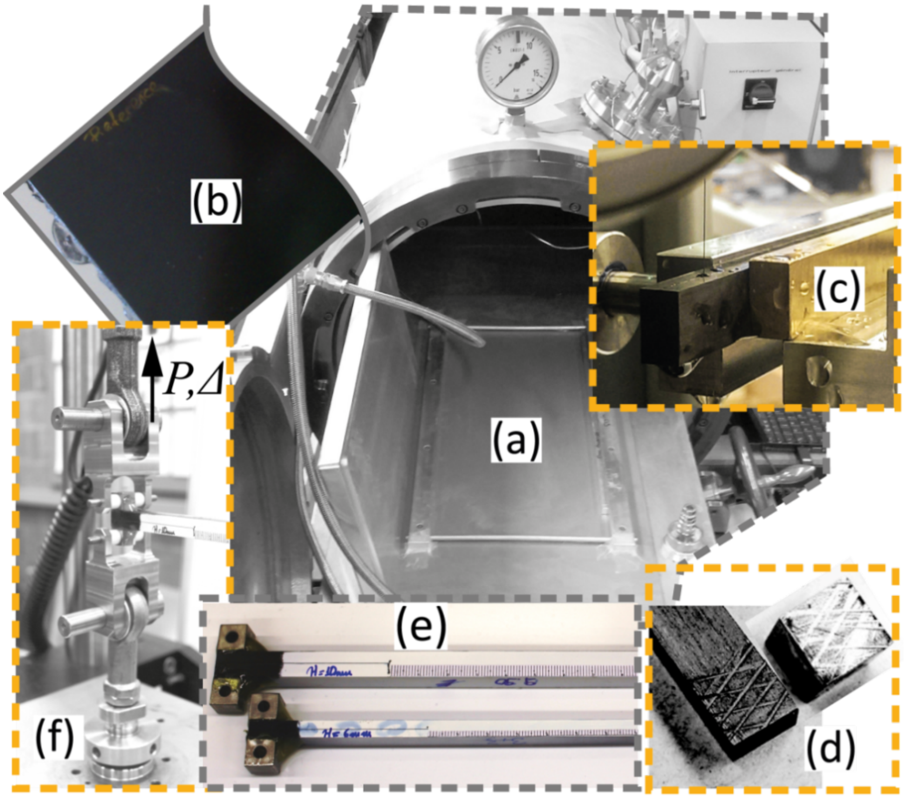

Fig. II.1: (a) Fabrication mold in the autoclave. (b) Fabricated composite plate. (c) Specimen precracking. (d) Specimen and loading block, prepared for bonding. (e) Specimens ready to test. (f) Specimen mounted on the testing machine.

The cured plate is cut in strip-coupons and consequently an intralaminar precrack is introduced by a diamond wire saw, as shown in Fig. II.1(c), forming a precrack with a tip as depicted in the micrograph of Fig. II.2(b). After this step the surfaces of the coupons are extensively roughened in the region of bonding with the loading blocks, as illustrated in Fig. II.1(d). This step is necessary to achieve the maximum possible bonding strength, since the expected loads are high due to the intensity of the LSB in intralaminar fracture. With the loading blocks bonded, the specimens are painted white and a fine, printed paper ruler is attached to side surface (Fig. II.1(e)) to enable crack propagation monitoring. Finally the prepared specimens are mounted on the testing machine before the experiment (Fig. II.1(f)). These final four steps are also followed in the preparation of the carbon/thermoplastic specimens.

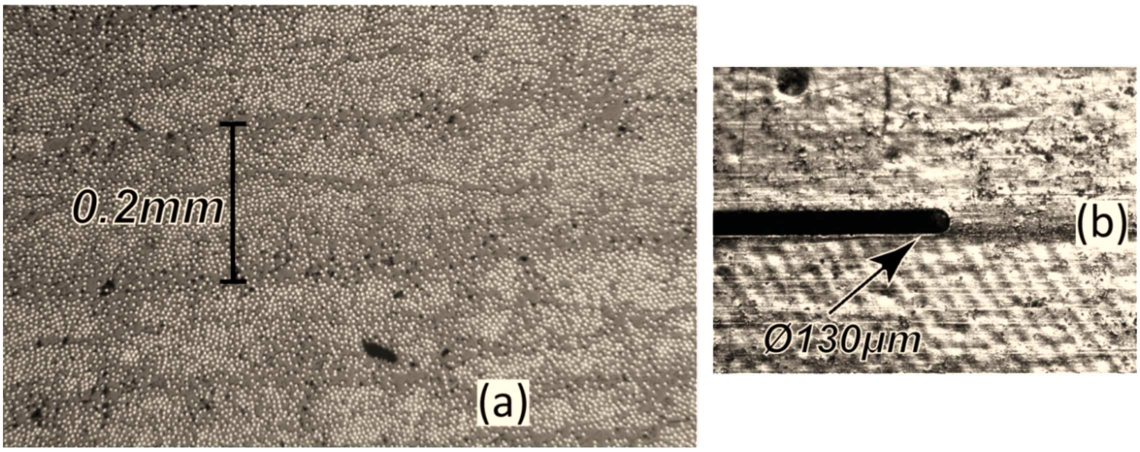

Fig. II.2: (a) Cross-section of the fabricated carbon/epoxy composite used for void calculation. (b) Microscopy of the pre-crack tip.

Appendix III

Fractography and micrographic observations

In this section, some microscopic observations related to the formation of the bridging bundles are included. A correlation between the evolution of bridging bundle size and number, with the increase in fracture resistance, for the investigated carbon epoxy system, is presented in Fig. III.1. Here a progressive evolution of the bridging bundle size and population is depicted while it is observed that LSB is formed immediately after the first crack propagation event. However, the size of the created bundles and their number is smaller than the corresponding morphology at the steady-state. Nevertheless, the cross-sectional profile of the bridging bundles appears to develop in an invariant manner after the R-curves reach a steady-state.

The small overshooting on the load-history prediction from the cohesive element model, and the R-curves predicted by the identified traction-separation relation, especially for the carbon/thermoset system, may be attributed to the described progressive development of the bridging bundles size and population, since the traction-separation identification is done for a point at the self-similar crack propagation and this applies to all investigated composite systems. Moreover, similar reasoning can be given for the minor overestimation of the load response on the micromechanical simulation in [66] (also in §4.3.4). For this case, the employed bridging bundle profile, modelled with the beam elements, corresponds to the cross-sections of the steady-state depicted in the largest cross-sectional photos of Fig. III.1. As a result the progressive evolution of the bundle size is not included on the micromechanical model. Nevertheless, the overestimation of the load-displacement response in the transient propagation state is small, while in both cases i.e. inverse identification and micromechanical approach, the steady-state response is described very well. Transient responses may be present in all fracture propagation events, however robust characterization can only be conducted when the crack propagates in a self-similar manner.

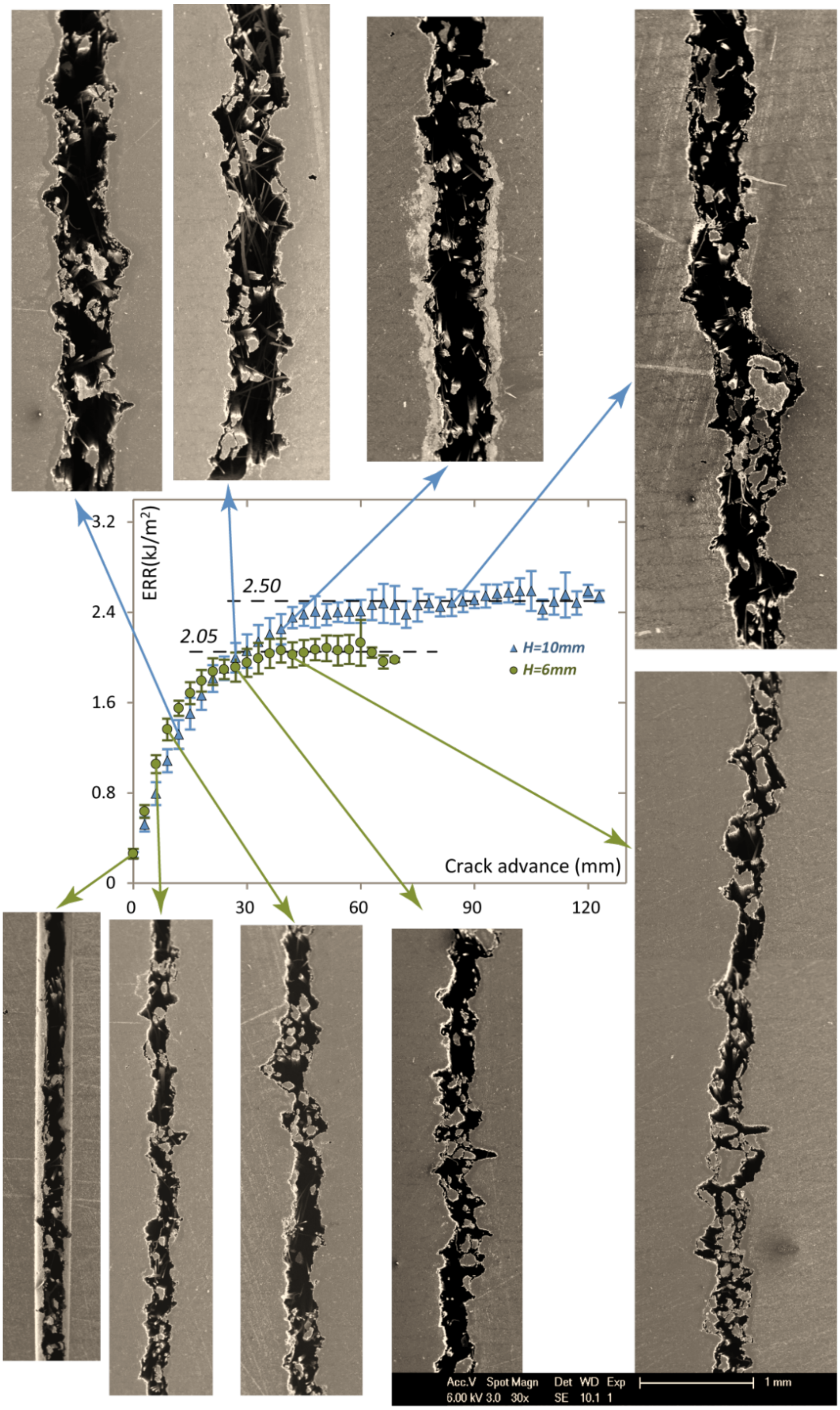

Fig. III.1: R-curves per thickness, and cross-sectional micrographs; Carbon/thermoset composite

Moreover some correlation between the fracture surface on the DCB arms and the bridging bundles, with the maximum closing traction due to LSB, $\sigma_{\max}$, is attempted. This analysis is processed for the carbon/epoxy system. For this purpose the length of a typical fracture surface's cross-section, Γ, on the DCB arms is measured, using the sketching tools of Autodesk® Inventor 2014, having manually created a polyline that follows the fracture profile, as shown in Fig. III.2(a). For the calculation of the fiber-bundle fracture profile, the cross-sectional area is initially evaluated, using the particle analysis of Image-J, open source image processing software. Consequently, the cross-section of each bundle is considered circular for simplicity and, the fracture profile per fiber-bundle, corresponding to the lower DCB arm, is approximated with the half of the circular periphery, c (see Fig. III.2(b)). Thus, the ratio of the fiber-bundle fracture profile and the fracture profile on the arm is approximated as $\sum c/\Gamma \simeq 4.3$. Remarkably, this ratio is very close to the ratio of the transverse strength and the maximum identified bridging traction; $\sigma_c/\sigma_{\max} \simeq 5$ (see §5.4). This analogy suggests that the maximum bridging traction is related with the size of the intact, active bundle/bulk interfaces right after the crack tip, where LSB is generated.

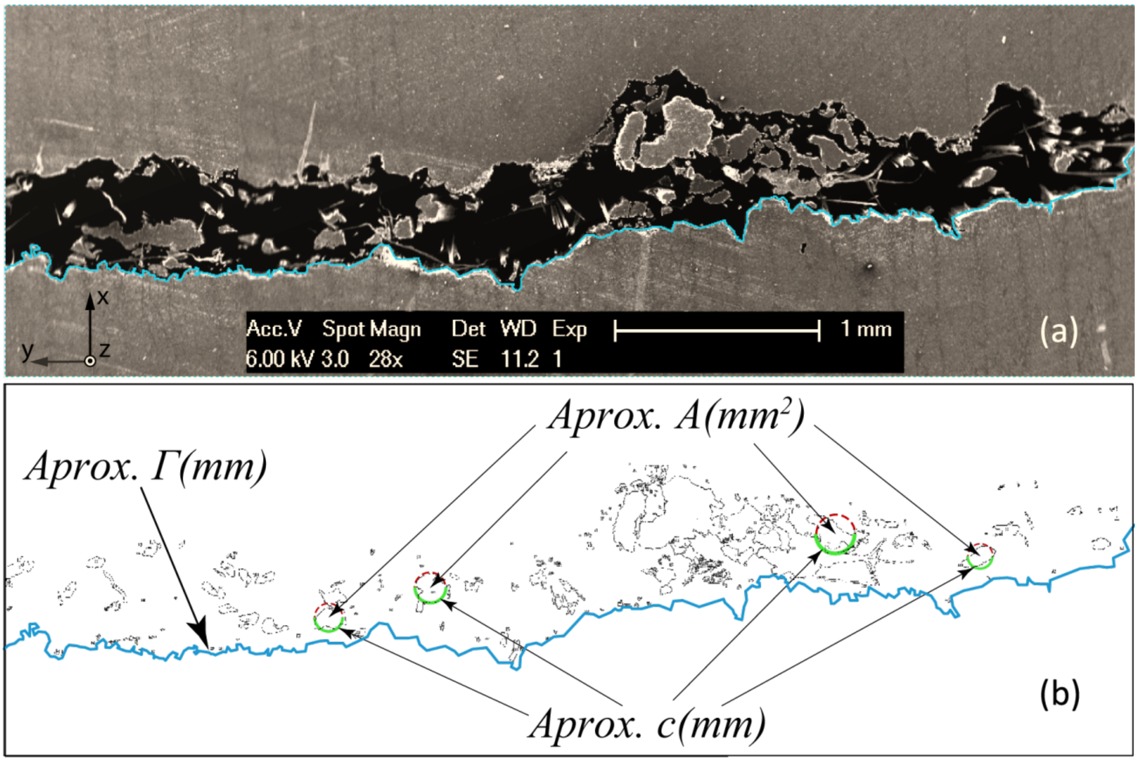

Fig. III.2: Bundle and bulk fracture surface analysis, $H = 10$mm, carbon/thermoset system:
(a) Microscopy of cross-section and approximated fracture profile.
(b) Approximated fiber-bundle area and fracture profile.

This analysis is not repeated for the carbon/thermoset system, nevertheless the corresponding transverse strength over maximum bridging traction is $\sigma_c / \sigma_{\max} \simeq 9.7$ and one may roughly observe that the fiber-bundle population for this system, depicted in Fig. III.3, is much smaller than the equivalent of the carbon/epoxy system shown in Fig. III.2, while the mean fiber-bundle size is similar.

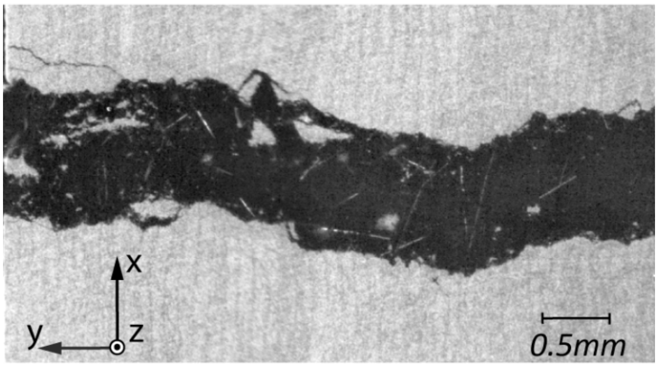

Fig. III.3: Microscopy of cross-section for bundle and bulk fracture surfaces investigation, AS4/PPS. See also Fig. 4.2(b).

Appendix IV
Design details of the Pure-Moment configuration

In this section some drawings of the designed and built PM testing setup, along with a photograph of the whole apparatus are presented to depict the solutions given to the particularities of this system.

The built PM test-rig mounted on the horizontal axis of the hydraulic biaxial machine, at the end of a DCB experiment, is displayed in Fig. IV.1. The key employed measuring instruments, described in §6.3, are indicated in this photograph.

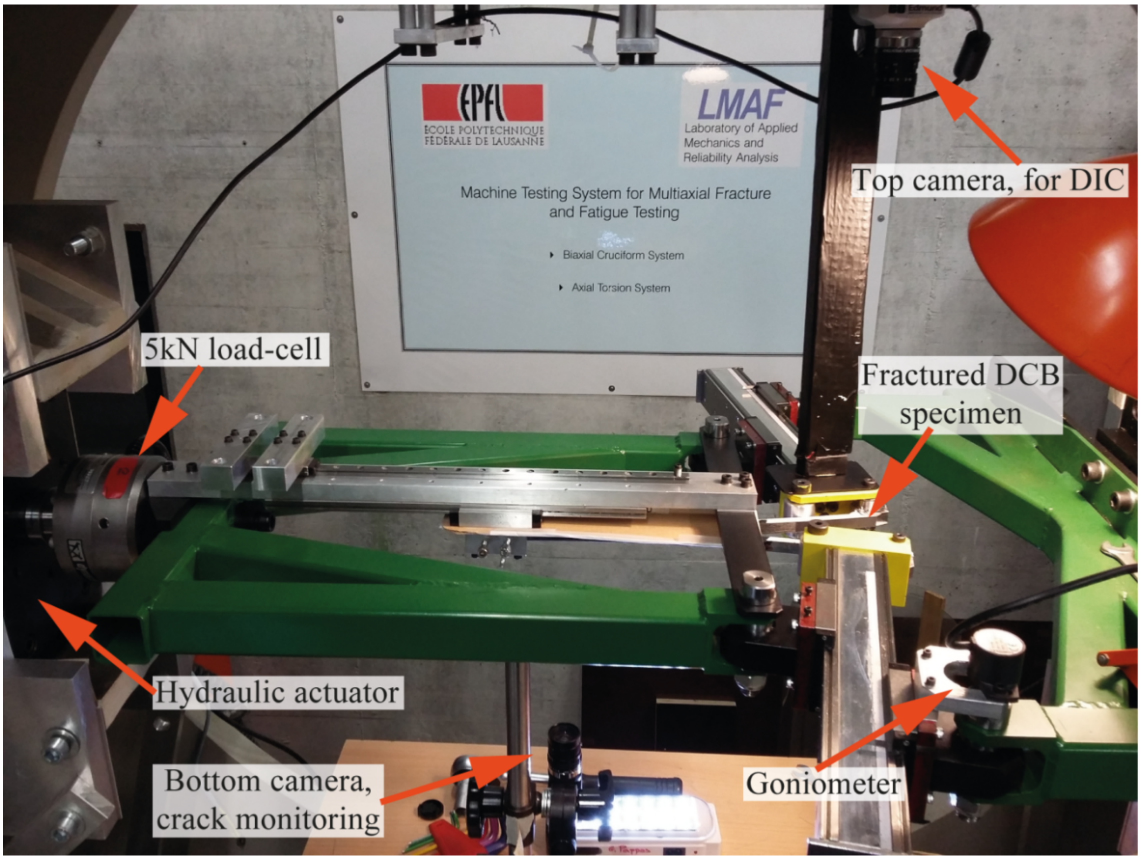
EPFL
ÉCOLE POLYTECHNIQUE FÉDÉRALE DE LAUSANNE
LMAF
Laboratory of Applied Mechanics and Reliability Analysis
Machine Testing System for Multiaxial Fracture and Fatigue Testing
Biaxial Cruciform System
Axial Torsion System
Top camera, for DIC
5kN load-cell
Fractured DCB specimen
Hydraulic actuator
Bottom camera, crack monitoring
Goniometer

Fig. IV.1: Photograph of the complete experimental setup at the end of an experiment.

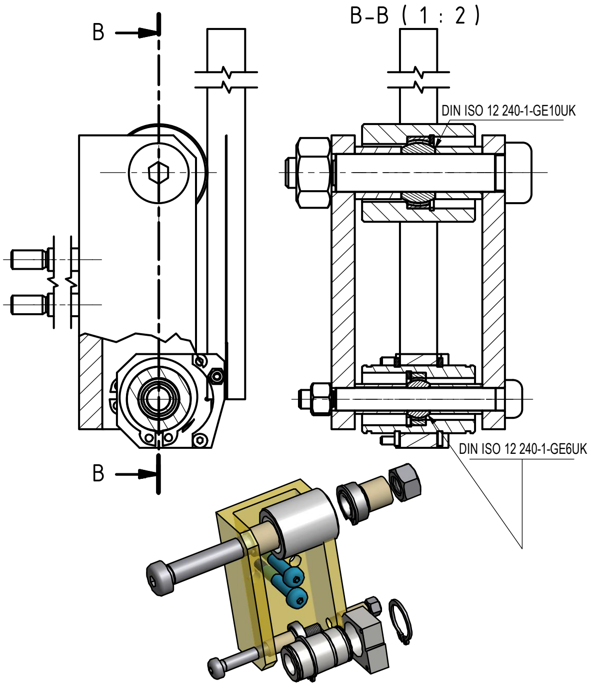

Fig. IV.2: Drawing of the assembled specimen gripping mechanism.

The drawing of the assembled specimen gripping mechanism is displayed in Fig. IV.2. The designed gripping mechanism comprises two spherical plain bearings to transfer the load to specimen. With this configuration, over-constraining is avoided, preventing the generation of torque due to any imperfection on specimen's geometry and misalignment on bonding of the loading blocks.

The load transfer from the two sub-frames to the sliding arms, without preventing the motion of the specimen, is the key feature on moment application. This is achieved by a combination of radial and linear ball bearings. The housing of the radial bearings and its connection with the carriages of the linear bearings, are shown in the drawing of Fig. IV.3. To avoid over-constraining on the connection points, a combination of self-aligning and deep-groove ball bearings is chosen. With this choice the initial preload on the linear bearings tends to zero, minimizing the applied friction.

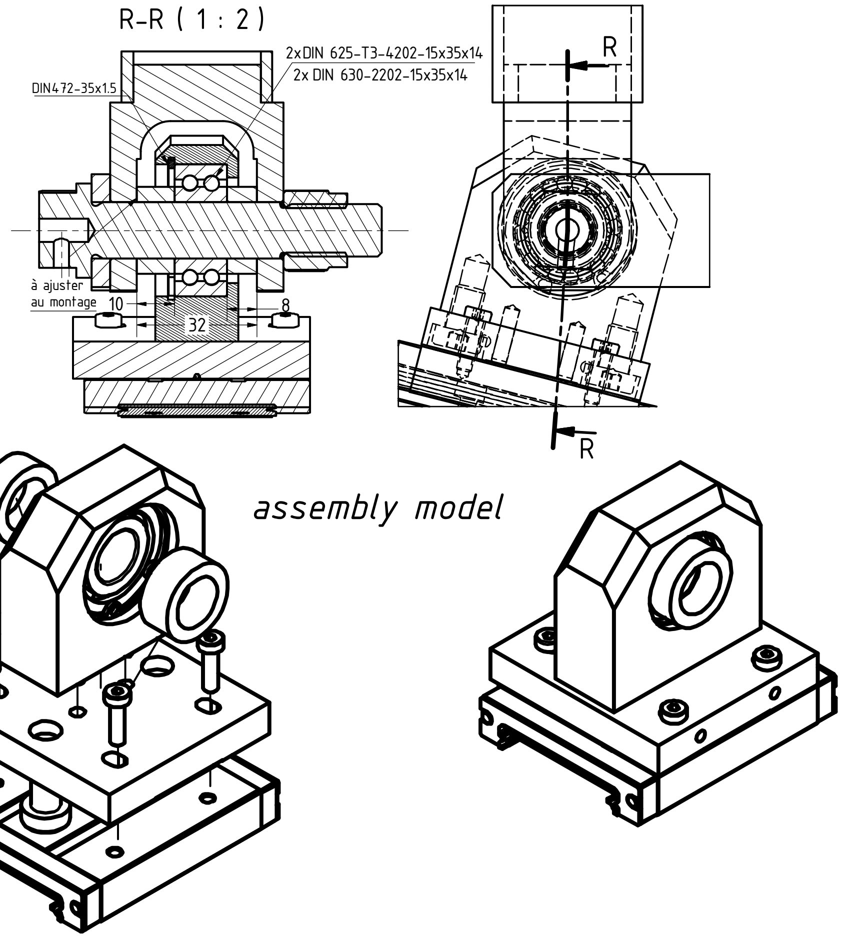
R-R (1 : 2)
2xDIN 625-T3-4202-15x35x14
2x DIN 630-2202-15x35x14
DIN472-35x1.5
à ajuster
au montage
10
32
8
R
R
assembly model

Fig. IV.3: Assembled housing of the radial bearings and its connection with the carriages of the linear bearings.

REFERENCES

[1] M. Holmes, "Carbon fibre reinforced plastics market continues growth path," *Reinforced Plastics*, vol. 57, no. 6, pp. 24-29, 2013.

[2] Isaak Daniel and Ori Ishai, *Engineering Mechanics of Composite Materials*. New York: Oxford University Press, 1994.

[3] K. Friedrich, "Fractographic Analysis of Polymer Composites," in *Application of Fracture Mechanics to Composite Materials*, K. Friedrich, Ed. Amsterdam, The Netherlands: Elsevier, 1989, ch. 11.

[4] E. Totry, C. González, and J. LLorca, "Failure locus of fiber-reinforced composites under transverse compression and out-of-plane shear," *Composites Science and Technology*, vol. 68, pp. 829-839, 2008.

[5] S.T. Pinho, P. Robinson, and L. Iannucci, "Fracture toughness of the tensile and compressive fibre failure modes in laminated composites," *Composites Science and Technology*, vol. 66, no. 13, pp. 2069 - 2079, 2006.

[6] P. Davies, W. Cantwell, C Moulin, and H.H. Kausch, "A study of the delamination resistance of IM6/PEEK composites," *Composites Science and Technology*, vol. 36, no. 2, pp. 153-166, 1989.

[7] S.M. Spearing and A.G. Evans, "The role of fiber bridging in the delamination resistance of fiber-reinforced composites," *Acta Metallurgica et Materialia*, vol. 40, no. 9, pp. 2191-2199, 1992.

[8] Z. Suo and G. Bao, "Delamination R-curve phenomena due to damage," *Journal of the Mechanics and Physics of Solids*, vol. 40, no. 1, pp. 1-16, 1992.

[9] B.F. Sørensen and T.K. Jacobsen, "Large-scale bridging in composites: R-curves and bridging laws," *Composites Part A: Applied Science and Manufacturing*, vol. 29, no. 11, pp. 1443-1451, 1998.

[10] V. Tamuzs, S. Tarasovs, and U. Vilks, "Progressive delamination and fiber bridging modeling in double cantilever beam composite specimens," *Engineering Fracture Mechanics*, vol. 68, no. 5, pp. 513-525, 2001.

[11] L. Sorensen, J. Botsis, Th. Gmür, and J. Cugnoni, "Delamination detection and characterization of bridging tractions using long FBG optical sensors," *Composites Part A: Applied Science and Manufacturing*, vol. 38, no. 10, pp. 2087-2096, 2007.

[12] S. Stutz, J. Cugnoni, and J. Botsis, "Studies of mode I delamination in monotonic and fatigue loading using FBG wavelength multiplexing and numerical analysis," *Composites Science and Technology*, vol. 71, no. 4, pp. 443-449, 2011.

[13] G. Bao and Z. Suo, "Remarks on Crack-Bridging Concepts," *Applied Mechanics Reviews*, vol. 45, no. 8, pp. 355-366, 1992.

[14] E. Farmand-Ashtiani, J. Cugnoni, and J. Botsis, "Specimen thickness dependence of large scale fiber bridging in mode I interlaminar fracture of carbon epoxy composite," *International Journal of Solids and Structures*, vol. 55, pp. 58-65, 2015.

[15] T. Jacobsen and B.F. Sørensen, "Mode I intra-laminar crack growth in composites-modeling of R-curve from measure bridging laws," *Composites Part A Applied Science and Manufacturing*, vol. 32, no. 1, pp. 1-11, 2001.

[16] M.F.S.F De Moura, R.D.S.G Campilho, A.M Amaro, and P.N.B Reis, "Interlaminar and intralaminar fracture characterization of composites under mode I loading," *Composite Structures*, vol. 92, no. 1, pp. 144-149, 2010.

[17] N. Sato, M. Hojo, and M. Nishikawa, "Novel test method for accurate characterization of intralaminar fracture toughness in CFRP laminates," *Composites Part B: Engineering*, vol. 65, pp. 89-98, 2014.

[18] B. Manshadi, A. Vassilopoulos, and J. Botsis, "A combined experimental/numerical study of the scaling effects on mode I delamination of GFRP," *Composites Science and Technology*, vol. 83, pp. 32-39, 2013.

[19] Ted Anderson, *Fracture Mechanics*, 2nd ed. Texas, USA: CRP, 1995.

[20] J. Botsis, Elements of Fracture Mechanics, 2013, Course material.

[21] D.S. Dugdale, "Yielding of steel sheets containing slits," *Journal of the Mechanics and Physics of Solids*, vol. 8, no. 2, pp. 100-104, 1960.

[22] G.I. Barenblatt, "The Mathematical Theory of Equilibrium Cracks in Brittle Fracture," *Advances in Applied Mechanics*, vol. 7, pp. 55-129, 1962.

[23] Brian Lawn, *Fracture of Brittle Solids*, 2nd ed. Cambridge, UK: © Cambridge University Press, 1993.

[24] Z. Bažant, "Concrete fracture models: testing and practice," *Engineering Fracture Mechanics*, vol. 69, no. 2, pp. 165-205, 2002.

[25] S. Hashemi, A. Kinloch, and G. Williams, "Mixed-Mode Fracture in Fiber-Polymer Composite Laminates," *Composite Materials: Fatigue and Fracture*, vol. 3, pp. 143-168, 1991.

[26] B. N. Cox and N., Sridhar, "A Traction Law for Inclined Fiber Tows Bridging Mixed-Mode Cracks," *Mechanics of Advanced Materials and Structures*, vol. 9, pp. 299–331, 2002.

[27] B. F. Sørensen and T. K. Jacobsen, "Characterizing delamination of fibre composites by mixed mode cohesive laws," *Composites Science and Technology*, vol. 69, no. 3-4, pp. 445–456, 2009.

[28] D. Sans, S. Stutz, J. Renart, J.A. Mayugo, and J. Botsis, "Crack tip identification with long FBG sensors in mixed-mode delamination," *Composite Structures*, vol. 94, pp. 2879–2887, 2012.

[29] M. Borotto, "Bridging effects on Mixed Mode delamination: experiments and numerical simulation," EPFL, Lausanne, PhD thesis 2016.

[30] J.R. Rice, "A Path Independent Integral and the Approximate Analysis of Strain Concentration by Notches and Cracks," *Journal of Applied Mechanics*, vol. 35, pp. 379-386, 1968.

[31] B.F. Sørensen, "Cohesive law and notch sensitivity of adhesive joints," *Acta Materialia*, vol. 50, no. 5, pp. 1053–1061, 2002.

[32] M. Studer, J. Pietrzyk, K. Peters, J. Botsis, and P. Giaccari, "Studies on bridging tractions – simultaneous bridging tractions," *International Journal of Fracture*, vol. 114, no. 4, pp. 379-399, 2002.

[33] C. Sarrado, A. Turon, J. Renart, and J. Costa, "An experimental data reduction method for the Mixed Mode Bending test based on the J-integral approach," *Composites Science and Technology*, vol. 117, pp. 85–91, 2015.

[34] C. Sarrado, A. Turon, J. Costa, and J. Renart, "An experimental analysis of the fracture behavior of composite bonded joints in terms of cohesive laws,"

Composites Part A: Applied Science and Manufacturing, vol. 90, pp. 234-242, 2016.

[35] L. Sorensen, J. Botsis, Th. Gmür, and L. Humbert, "Bridging tractions in mode I delamination: Measurements and simulations," *Composites Science and Technology*, vol. 68, no. 12, pp. 2350-2358, 2008.

[36] M. Heidari-Rarani, M.M. Shokrieh, and P.P. Camanho, "Finite element modeling of mode I delamination growth in laminated DCB specimens with R-curve effects," *Composites part B: Engineering*, vol. 45, no. 1, pp. 897-903, 2013.

[37] V. Antonucci, M. Giordano, A. Cusano, J. Nasser, and L. Nicolais, "Real time monitoring of cure and gelification of a thermoset matrix.," *Composites Science and Technology*, vol. 66, no. 16, pp. 3273-3280, 2006.

[38] J., Cugnoni, J. Frieden, J. Botsis, T. Gmür, and D. Ćorić, "High-speed internal strain measurements in composite structures under dynamic load using embedded internal strain measurements in composite structures under dynamic load using embedded FBG sensors," *Composite Structures*, vol. 92, no. 8, pp. 1905-1912, 2010.

[39] R. Di Sante and L. Donati, "Strain monitoring with embedded Fiber Bragg Gratings in advanced composite structures for nautical applications," *Measurement*, vol. 46, no. 7, pp. 2118-2126, 2013.

[40] G. Luyckx, E. Voet, N. Lammens, and J. Degrieck, "Strain Measurements of Composite Laminates with Embedded Fibre Bragg Gratings: Criticism and Opportunities for Research," *Sensors*, vol. 11, no. 1, pp. 384–408, 2011.

[41] A. Airoldi and CG. Dávila, "Identification of material parameters for modelling delamination in the presence of fibre bridging," *Composite Structures*, vol. 94, no. 11, pp. 3240-3249, 2012.

[42] P.P. Camanho and C.G. Dávila, "Mixed-mode decohesion finite elements for the simulation of delamination in composite materials," *NASA/TM-2002–211737*, pp. 1-37, 2002.

[43] C.T. Sun and Z.H. Jin, "Modeling of composite fracture using cohesive zone and bridging models," *Composites science and technology*, vol. 66, no. 10, pp. 1297-1302, 2006.

[44] V. Shanmugam, R. Penmetsa, E. Tuegel, and S. Clay, "Stochastic modeling of delamination growth in unidirectional composite DCB specimens using cohesive zone models," *Composite Structures*, vol. 102, pp. 38-60, 2013.

[45] G. Frossard, J. Cugnoni, T. Gmür, and J. Botsis, "Mode I interlaminar fracture of carbon epoxy laminates: Effects of ply thickness," *Composites: Part A*, vol. 91, pp. 1-8, 2016.

[46] Jia-Yen Huang, "Studies of geometry effects on strain-energy release rate of composite laminate," *Engineering Fracture Mechanics*, vol. 47, no. 6, pp. 893-900, 1994.

[47] M. Hojo and T. Aoki, "Thickness Effect of Double Cantilever Beam Specimen on lnterlaminar Fracture Toughness of AS4/PEEK and T800/Epoxy Laminates," *Composite Materials: Fatigue and Fracture*, vol. 4, pp. 281-298, 1993.

[48] E. Farmand-Ashtiani, D. Alanis, J. Cugnoni, and J. Botsis, "Delamination in cross-ply laminates: Identification of traction-separation relations and cohesive zone modeling," *Composites Science and Technology*, vol. 119, pp. 85-92, 2015 b.

[49] ASTM Standard D5528−01, *Standard Test Method for Mode I Interlaminar Fracture Toughness of Unidirectional Fiber-Reinforced Polymer Matrix Composites*. West Conshohocken, PA, United States of America: ASTM International, 2007.

[50] Airbus industry test method, "Carbon fiber reinforced plastics, Determination of interlaminar fracture, Mode I," *AITM 1.0005*, no. 2, June 1994.

[51] ISO 15024, *Fibre-reinforced plastic composites - Determination of mode I interlaminar fracture toughness, GIC, for unidirectionally reinforced materials*, 1st ed. Geneva, Switzerland: ISO Standard, 2001.

[52] N. Sela and O. Ishai, "Interlaminar fracture toughness and toughening of laminated composite materials:a review," *Composites*, vol. 20, no. 5, pp. 423-435, 1989.

[53] T.A. Sebaey, N. Blanco, J. Costa, and C.S. Lopes, "Characterization of crack propagation in mode I delamination of multidirectional CFRP laminates," *Composites Science and Technology*, vol. 72, pp. 1251-1256, 2012.

[54] L. Yao, R. Alderliesten, M. Zhao, and R. Benedictus, "Bridging effect on mode I fatigue delamination behavior in composite laminates," *Composites: Part A*,

vol. 63, pp. 103-109, 2014.

[55] G. Pappas and J. Botsis, "Intralaminar fracture of unidirectional carbon/epoxy composite: experimental results and numerical analysis," *International Journal of Solids and Structures*, vol. 85-86, pp. 114-124, 2016.

[56] S. Mohammadi, *Introduction, in Extended Finite Element Method: For Fracture Analysis of Structures*. Oxford, UK: Blackwell Publishing Ltd, 2008.

[57] © Systèmes Dassault, *Abaqus Analysis User's Manual (v6.12).*: Dassault Systèmes Simulia Corp, 2012.

[58] O.T. Topac, B. Gozluklu, E. Gurses, and D. Coker, "Experimental and computational study of the damage process in CFRP composite beams under low-velocity impact," *Composites Part A: Applied Science and Manufacturing*, vol. 92, pp. 167-182, 2017.

[59] B.P. Bussadori, K. Schuffenhaue, and A. Scattina, "Modelling of CFRP crushing structures in explicit crash analysis," *Composites Part B: Engineering*, vol. 60, pp. 725-735, April 2014.

[60] D.A.W. Kaute, H.R. Shercliff, and M.F. Ashby, "Delamination, fibre bridging and toughness of ceramic matrix composites," *Acta Metallurgica et Materialia*, vol. 41, no. 7, pp. 1959-1970, 1993.

[61] B.F. Sørensen, K. Gamstedt, R. Østergaard, and Goutianos S., "Micromechanical model of cross-over fibre bridging – Prediction of mixed mode bridging laws," *Mechanics of Materials*, vol. 40, pp. 220–234, 2008.

[62] B. Cox and Q Yang, "In quest of virtual test for structural composites," *Science 314*, vol. 314, pp. 1102-1107, 2006.

[63] L.P. Canal, J. Segurado, and J. LLorca, "Failure surface of epoxy-modified fiber-reinforced composites under transverse tension and out-of-plane shear," *Int J Solids Struct*, vol. 46, pp. 2265-2274, 2009.

[64] V. Šmilauer, C. Hoover, Z. P. Bažant, F. Caner, A. Waas, and K. Shahwan, "Multiscale simulation of fracture of braided composites via repetitive unit cells," *Engineering Fracture Mechanics*, vol. 78, no. 6, pp. 901-918, 2011.

[65] J. LLorca, C. González, J.M. Molina-Aldareguía, J. Segurado, R. Seltzer, F. Sket, M. Rodríguez, S. Sádaba, R. Muñoz, and L.P. Canal, "Multiscale Modeling of

Composite Materials: a Roadmap Towards Virtual Testing," *Advanced Materials*, vol. 23, pp. 5130-5147, 2011.

[66] L.P. Canal, G. Pappas, and J. Botsis, "Large scale Fiber bridging in mode I intralaminar fracture: multi-scale mechanisms and simulations," *Composites Science and Technology*, vol. 126, pp. 52-59, 2016.

[67] G. Pappas, L.P. Canal, and J. Botsis, "Characterization of intralaminar mode I fracture of AS4/PPS composite using inverse identification and micromechanics," *Composites: Part A*, vol. 91, pp. 117-126, 2016.

[68] C. Scarponi, A.M. Perillo, L. Cutillo, and C. Foglio, "Advanced TTT composite materials for aeronautical purposes: Compression after impact (CAI) behaviour," *Composites Part B: Engineering*, vol. 38, no. 2, pp. 258-264, 2007.

[69] Fritz Larsson, "Damage tolerance of a stitched carbon/epoxy laminate," *Composites Part A: Applied Science and Manufacturing*, vol. 28, no. 11, pp. 923-934, 1997.

[70] D.D.R. Cartié, B.N. Cox, and N.A. Fleck, "Mechanisms of crack bridging by composite and metallic rods," *Composites Part A: Applied Science and Manufacturing*, vol. 35, no. 11, pp. 1325-1336, 2004.

[71] K. Pingkarawat and , A.P. Mouritz, "Comparative study of metal and composite z-pins for delamination fracture and fatigue strengthening of composites," *Engineering Fracture Mechanics*, vol. 154, pp. 180-190, 2016.

[72] B. Zhang, G. Allegri, M. Yasaee, and S.R. Hallett, "Micro-mechanical finite element analysis of Z-pins under mixed-mode loading," *Composites Part A: Applied Science and Manufacturing*, vol. 78, pp. 424-435, 2015.

[73] G. Allegri, M. Yasaee, I.K. Partridge, and S.R. Hallett, "A novel model of delamination bridging via Z-pins in composite laminates," *International Journal of Solids and Structures*, vol. 51, no. 19-20, pp. 3314-3332, 2014.

[74] F. Bianchi and X. Zhang, "A cohesive zone model for predicting delamination suppression in z-pinned laminates," *Composites Science and Technology*, vol. 71, no. 16, pp. 1898-1907, 2011.

[75] M. Colin de Verdiere, A.A. Skordos, M. Maya, and A.C. Walton, "Influence of loading rate on the delamination response of untufted and tufted carbon epoxy non crimp fabric composites: Mode I," *Engineering Fracture Mechanics*,

vol. 96, pp. 11-25, 2012.

[76] C. Osmiani, G. Mohamed, J.W.G. Treiber, G. Allegri, and I.K. Partridge, "Exploring the influence of micro-structure on the mechanical properties and crack bridging mechanisms of fibrous tufts," *Composites Part A: Applied Science and Manufacturing*, vol. 91, no. Part 2, pp. 409-419, 2016.

[77] H. Wang and T. Vu-Khanh, "Use of end-loaded-split (ELS) test to study stable fracture behaviour of composites under mode II loading," *Composite Structures*, vol. 36, no. 1-2, pp. 71-79, 1996.

[78] B.F. Sørensen, P. Brethe, and P. Skov-Hansen, "Controlled Crack Growth in Ceramics: The DCB Specimen Loaded with Pure Moments," *Journal of the European Ceramic Society*, vol. 16, no. 9, pp. 1021-1025, 1996.

[79] C. Berggreen and K. N. Anyfantis, "Fracture characterization of interfaces with a new DCB-UBM test rig," in *ICEM-16*, Cambridge, 2014.

[80] V. Saseendran, C. Berggreen, and L. Carlsson, "Fracture testing of honeycomb core sandwich composites using the DCB-UBM test," in *ICCM-20*, Copenhagen, 2015.

[81] B. Mirzaei, A. Sinha, and J.A. Nairn, "Measuring and modeling fiber bridging: Application to wood and wood composites exposed to moisture cycling," *Composites Science and Technology*, vol. 128, pp. 65-74, 2016.

[82] S. W. Freiman, D. R. Mulville, and P. W. Mast, "Crack propagation studies in brittle materials," *Journal of Materials Science*, vol. 8, no. 11, pp. 1527–1533, 1973.

[83] J.E Lindhagen and L.A Berglund, "Application of bridging-law concepts to short-fibre compositesPart 1: DCB test procedures for bridging law and fracture energy," *Composites Science and Technology*, vol. 60, no. 6, pp. 870-883, 2000.

[84] H., Paris, P.C., Irwin, G.R. Tada, *The stress analysis of cracks handbook*, 3rd ed. New York: ASME Press, 2000.

[85] M. Czabaj and J. Ratcliffe, "Comparison of intralaminar and interlaminar mode I fracture toughnesses of a unidirectional IM7/8552 carbon/epoxy composite," *Compos Sci Technol*, vol. 89, pp. 15-23, 2013.

[86] A. Hillerborg, M. Modéer, and P.E. Petersson, "Analysis of crack formation and

crack growth in concrete by means of fracture mechanics and finite elements," *Cement and Concrete Research*, vol. 6, no. 6, pp. 773-781, 1976.

[87] T.K O'Brien and R.H. Martin, "Round Robin Testing for Mode I Interlaminar Fracture Toughness of Composite Materials," *Journal of Composite Technology & Research*, vol. 15, no. 4, pp. 269-281, 1993.

[88] C.T. Sun and Z.-H. Jin, *Fracture Mechanics*. Boston, USA: Academic Press, 2012.

[89] G.R. Irwin and J.A. Kies, "Critical energy rate analysis of fracture," *Welding Journal*, vol. 33, pp. 193-198, 1954.

[90] S. Hashemi, A.J. Kinloch, and J.G. Williams, "The Analysis of Interlaminar Fracture in Uniaxial Fibre-Polymer Composites," *Proceedings of the Royal Society of London. Series A, Mathematical and Physical*, vol. 427, pp. 173-199, 1990.

[91] J.P. Berry, "Determination of Fracture Energies by the Cleavage Technique," *Journal of Applied Physics*, vol. 34, no. 1, pp. 62-68, 1963.

[92] K. Kageyama and M. Hojo, "Proposed Methods for Intrerlaminar Fracture Toughness Tests of Composite Laminates," in *Proceedings of the 5th U.S/Japan Conference on Composite Materials*, Tokyo, 1990, pp. 227-234.

[93] P. C. Paris and A. J. Paris, "Instantaneous evaluation of J and C*," *International Journal of Fracture*, vol. 38, pp. R19-R21, 1988.

[94] U. Stigh, "Measurement of cohesive laws and related problems," in *IMECE*, vol. 11, Florida,USA, 2009, pp. 293–298.

[95] T. Andersson and U. Stigh, "The stress–elongation relation for an adhesive layer loaded in peel using equilibrium of energetic forces," *International Journal of Solids and Structures*, vol. 41, no. 2, pp. 413-434, 2004.

[96] K.O. Hill and G. Meltz, "Fiber Bragg grating technology fundamentals and overview," *Journal of Lightwave Technology*, vol. 15, no. 8, pp. 1263-1276, 1997.

[97] R. Measures, *Structural Monitoring with Fiber Optic Technology*, 1st ed. USA: Academic Press, 2001.

[98] J. Botsis, "Fiber Bragg Grating applied to in-situ characterization of composites," in *Wiley Encyclopedia of Composites*. New Jersey: John Wiley &

Sons, 2012, pp. 1-15.

[99] P. Giaccari, G.R. Dunkel, L. Humbert, J. Botsis, H.G. Limberger, and P.R. Salathé, "On a direct determination of non-uniform internal strain fields using fibre Bragg gratings," *Smart materials and structures*, vol. 14, no. 1, pp. 127-136, 2005.

[100] W.W. Morey, J.R. Dunphy, and G. Meltz, "Multiplexing fiber Bragg grating sensors," *Fiber & Integrated Optics*, vol. 10, no. 4, pp. 351-360, 1991.

[101] P. Giaccari, "Fiber bragg grating characterization by optical low coherencere rectometry and sensing applications," EPFL, Lausanne, PhD thesis 2003.

[102] B. Vieille, J. Aucher, and L. Taleb, "Influence of temperature on the behavior of carbon fiber fabrics reinforced PPS laminates," *Materials Science and Engineering A*, vol. 517, no. 1-2, pp. 51-60, 2009.

[103] R. Massabòa, L. Brandinellib, and B. N. Cox, "Mode I weight functions for an orthotropic double cantilever beam," *International Journal of Engineering Science*, vol. 41, no. 13-14, pp. 1497-1518, 2003.

[104] TenCate Advanced Composites™. (2015, Mar.) TenCate Cetex® TC1100 PPS resin system. Product datasheet. [Online]. http://www.tencate.com

[105] Gurit SP™. (2014, July) SE 70, Low temperature cure high toughness epoxy prepreg system. General datasheet. [Online]. http://www.gurit.com

[106] Ted Diehl, "Modeling Surface-Bonded Structures with ABAQUS Cohesive Elements: Beam-Type Solutions," in *ABAQUS Users' Conference*, Boston, 2004, pp. 1-27.

[107] J. Cugnoni, Th. Gmur, and A. Schorderet, "Inverse method based on modal analysis for characterizing the constitutive properties of thick composite plates," *Composite Structures*, vol. 85, no. 17, pp. 1310-1320, 2007.

[108] J. Cugnoni, "Identification par recalage modal et fréquentiel des propriétés constitutives de coques en matériaux composites," EPFL, Lausanne, PhD Thesis 2005.

[109] J.D. Gunderson, J.F. Brueck, and A.J. Paris, "Alternative test method for interlaminar fracture toughness of composites," *International Journal of Fracture*, vol. 143, no. 3, pp. 273-276, 2007.

[110] A. Biel and U. Stigh, "Effects of constitutive parameters on the accuracy of measured fracture energy using the DCB-specimen," *Eng Fract Mech*, vol. 75, no. 10, pp. 2968-2983, 2008.

[111] ASTM Standard D6272−10, *Standard Test Method for Flexural Properties of Unreinforced and Reinforced Plastics and Electrical Insulating Materials by Four-Point Bending*. West Conshohocken, PA, United States of America: ASTM International, 2010.

[112] ASTM Standard D3039/D3039M–14, *Standard Test Method for Tensile Properties of Polymer Matrix Composite Materials*. West Conshohocken, PA, United States of America: ASTM International, 2014.

[113] ASTM Standard D3518/D3518M−13, *Standard Test Method for In-Plane Shear Response of Polymer Matrix Composite Materials by Tensile Test of a ±45° Laminate*. West Conshohocken, PA, United States of America: ASTM International, 2013.

[114] R.D. Kriz and W.W. Stinchcomb, "Elastic moduli of transversely isotropic graphite fibers and their composites," *Experimental Mechanics*, vol. 19, no. 2, pp. 41-47, 1979.

[115] S. Mahmoud and K. Lease, "The effect of specimen thickness on the experimental characterization of critical crack-tip-opening angle in 2024-T351 aluminum alloy," *Engineering Fracture Mechanics*, vol. 70, no. 3-4, pp. 443-456, 2003.

[116] K.L. Johnson, *Contact mechanics*, 1st ed. Cambridge, UK: © Cambridge University Press, 1985.

[117] M. Meng, H.R. Le, M.J. Rizvi, and S.M. Grove, "The effects of unequal compressive/tensile moduli of composites," *Composite Structures*, vol. 126, pp. 207–215, 2015.

[118] ASTM Standard D3171−15, *Standard Test Methods for Constituent Content of Composite Materials*. West Conshohocken, PA, United States of America: ASTM International, 2015.

[119] Advanced Materials Huntsman International LLC®. (2016, Sep.) Araldite® LY 8615 / Aradur® 8615 / Hardener XB 5173. Technical datasheet. [Online]. http://samaro.fr

[120] L.P. Canal, M. Alfano, and J. Botsis, "A multi-scale based cohesive zone model for the analysis of thickness scaling effect in fiber bridging," *Composites Science and Technology*, vol. 139, pp. 90-98, February 2017.

[121] A.J. Kinloch, Y. Wang, J.G. Williams, and P. Yayla, "The mixed-mode delamination of fibre composite materials," *Composites Science and Technology*, vol. 47, no. 3, pp. 225–237, 1993.

[122] E. Farmand-Ashtiani, J. Cugnoni, and J. Botsis, "Effects of large scale bridging in load controlled fatigue delamination of unidirectional carbon-epoxy specimens," *Composites Science and Technology*, vol. 137, pp. 52-59, 2016.

[123] C.F Shih, B Moran, and T Nakamura, "Energy Release Rate Along a Three-Dimensional Crack," *International Journal of Fracture*, vol. 30, pp. 79-102, 1986.

[124] J. Nairn, "Analytical and numerical modeling of R curves for cracks with bridging zones," *International Journal of Fracture*, vol. 155, no. 2, pp. 167-181, 2009.

Curriculum Vitæ

Georgios PAPPAS

Nationality: **Greek**

Email: **georgios.pappas@epfl.ch**

EDUCATION

2/2013 –5/2017	**PhD in Solid Mechanics** École Polytecchnique Fédérale de Lausanne (EPFL), Lausanne, Switzerland. ***Doctoral Thesis:*** *'Studies On Traction Separation Relations of Layered Composites'.*
2003 – 2009	**Dipl. Eng. in Mechanical Engineering** ***Analysis and Synthesis of Mechanisms*** Department of Mechanical Engineering, School of Engineering, Aristotle University of Thessaloniki (AUTh), Greece. Grade 8.02 (scale 5 to 10), 'Very Good', *ranked 2nd in terms of grades, among 52 graduates.* ***Diploma Thesis*****:** *'Analysis and Design of Wheel Uprights & Bearing, Brake System and Pedals, of a Formula student race car'.* **Activities & Societies:** Co-founder of F-SAE team of A.U.Th. & Leader for 2006-2007 (ART-7).
2000 – 2003	**High School Diploma** 1st General Lyceum of Cholargos, Athens.

TEACHING EXPERIENCE

2013 – 2017	**Teaching Assistant**, EPFL (Lausanne, VD) in the courses: "Mécanique des structures" (Mechanics of structures) "Mécanique des milieux continus" (Continuum mechanics) "Fracture mechanics"

PROFESSIONAL EXPERIENCE

02/2013 – today	**Doctoral assistant & Lab IT Administrator,** Laboratory of Applied Mechanics and Reliability Analysis, École Polytechnique Fédérale de Lausanne (EPFL), Lausanne, Switzerland.
09/2012 – 12/2012	**Research Fellow**, Department of Mechanical Engineering, Politecnico di Milano (Milan, Italy).
9/2011 – 07/2012	**Freelance** as Mechanical & Building Engineer, (Athens, Greece).
10/2009 – 06/2011	**Research Fellow & Lab infrastructure Engineer**, Laboratory of Machine Elements and Machine Design (LMEMD) of Aristotle University of Thessaloniki (Thessaloniki, Greece) ***Achievements & Responsibilities:*** Design and conduction of fatigue experiments in commercial leaf springs. Redesign and Upgrade the Hydraulic Power Station and Cooling System of a testing machine.

PROFESSIONAL QUALIFICATIONS

Computer Skills:

Operating Systems:	Windows, Unix, Mac OS
Languages:	Matlab, Fortran, Visual Fortran, C, Arduino programming
Packages:	MS Office, Wolfram Mathematica, Origin, Adobe Illustrator, GIMP and many others.
CAD-CAE Software:	Autodesk Inventor, Autodesk AutoCAD Mechanical Desktop, Abaqus Simulia, ANSA-mETA of beta CAE Systems, MSC Nastran, DTECH-Dynamis

Languages:

Greek	Native of Bilingual Proficiency
English	Full Professional Proficiency
French	Professional Working Proficiency

PUBLICATIONS

G. Pappas, L.P. Canal, and J. Botsis, “Mode I Intralaminar fracture; comparison of end opening forces and pure moment loading”, *In preparation*.

G. Pappas, S. Joncas, V. Michaud, J. Botsis, “The Influence of Through-Thickness Reinforcement Geometry and Pattern on Delamination of Fiber-Reinforced Composites: Part I - Experimental results”, *In preparation*.

G. Pappas, S. Joncas, V. Michaud, J. Botsis, “The Influence of Through-Thickness Reinforcement Geometry and Pattern on Delamination of Fiber-Reinforced Composites: Part II - Modelling”, *In preparation*.

G. Pappas, L.P. Canal, and J. Botsis, “Characterization of intralaminar mode I fracture of AS4/PPS composite using inverse identification and micromechanics”, *Composites: Part A*, vol. 91, pp. 117-126, 2016.

L.P. Canal, G. Pappas, and J. Botsis, "Large scale Fiber bridging in mode I intralaminar fracture: multi-scale mechanisms and simulations", *Composites Science and Technology*, vol. 126, pp. 52-59, 2016.

G. Pappas and J. Botsis, "Intralaminar fracture of unidirectional carbon/epoxy composite: experimental results and numerical analysis", *International Journal of Solids and Structures*, vol. 85-86, pp. 114-124, 2016.

R. Fragoudakis, A. Saigal, G. Savaidis, I. Bazios, M. Malikoutsakis, A. Savaidis, *G. Pappas*, S. Karditsas, *“Fatigue Assessment and Failure Analysis of Shot Peened Leaf Springs”*, Fatigue & Fracture of Engineering Materials & Structures, vol. 36, no. 2, pp. 92–101, 2013.

BOOK CHAPTERS

J. Botsis, E. Farmand-Ashtiani, G. Pappas, J. Cugnoni, and L.P. Canal, "Traction-Separation Relations in Delamination of Layered Carbon-Epoxy Composites Under Monotonic Loads: Experiments and Modeling", in *The Structural Integrity of Carbon Fiber Composites*, P. Beaumont and C. Soutis, Eds. Cham, Switzerland: Springer International Publishing, 2016, ch. 20, pp. 549-590.

CONFERENCE PROCEEDINGS

S. Joncas, G. Pappas, J. Botsis, V. Michaud, “Interlaminar fracture in tufted composites: effects of tuft geometry and surface density”, Canadian-international conference on composites (CANCOM2017) Ottawa, Canada, Accepted.

G. Pappas, J. Botsis, “Experimental studies on mode I fracture and damage in DCB subjected to pure moments”, 8th International Conference on Fracture of Polymers, Composites and Adhesives (ESIS2017) Les Diablerets, Switzerland, Accepted.

L.P. Canal, G. Pappas, J. Botsis, “Micromechanics of large scale bridging in mode i intralaminar fracture”, 17th International Conference on Experimental Mechanics (ICEM 17), Rhodes, Greece, July 2016.

G. Pappas, L.P. Canal, J. Botsis, “Intralaminar Mode I fracture of a carbon-fiber reinforced thermoplastic composite: Experimental characterization and modeling”, European Mechanics of Materials Conference (EMMC-15), Brussels, Belgium, September 2016.

L.P. Canal, G. Pappas, J. Botsis, “Multi-scale modeling of mode I intra-ply fracture in fiber-reinforced composites”, European Mechanics of Materials Conference (EMMC-15), Brussels, Belgium, September 2016.

L.P. Canal, G. Pappas, J. Botsis, “Multi-scale simulations of large scale fiber bridging in mode i intra-ply fracture”, 17th European Conference on Composite Materials (ECCM17), Munich, Germany, June 2016.

G. Pappas, J. Botsis, “Fiber bridging in intralaminar mode I fracture of a unidirectional carbon/epoxy composite; effects of specimen size”, 5th ECCOMAS Thematic Conference on The Mechanical Response of Composites, Bristol, UK, September 2015.

G. Pappas, J. Botsis, “Traction separation response of a unidirectional carbon/epoxy composite in intralaminar mode I fracture; experimental and numerical results”, 20th International Conference on Composite Materials (ICCM20), Copenhagen, Denmark, July 2015

J. Botsis, G. Pappas, E. Farmand-Ashtiani, J. Cugnoni, “Inter- & intralaminar fracture response of unidirectional composites: resistance curves & traction separation relations”, COMINT Workshop (2015), KAUST, Thuwal, Saudi Arabia, June, 2015.

G. Pappas, J. Botsis, “Intralaminar Mode I fracture and bridging of a unidirectional Carbon/Epoxy composite”, 16th International Conference on Experimental Mechanics (ICEM-16), Cambridge, UK, July 2014.

R. Fragoudakis, A. Saigal, G. Savaidis, I. Bazios, M. Malikoutsakis, G. Pappas, S. Karditsas, A. Savaidis, *‘Fatigue Assessment and Failure Analysis of Shot Peened Leaf Springs’*, 2nd International Conference of Engineering Against Fracture (ICEAF II), Mykonos, Greece, June 2011.

AWARDS

18/11/2009	**Award of Excellence and Innovation of 2009, from the Research Committee of A.U.Th**, as a member of the Aristotle Racing Team (F-SAE team).
09/11/2007	**Commendation from the Dean of School of Engineering A.U.Th., Professor Nikolaos Moussiopoulos**, for participating at the ART7 team, who designed and constructed the first formula-student vehicle of the Aristotle University of Thessaloniki, which participated at the competition Formula-ATA, in Italy at 2007.

PROFESSIONAL MEMBERSHIPS

09/3/2010	Member of the Technical Chamber of Greece, holder of ***Professional license practicing Mechanical Engineering.***